Theses and Dissertations   1. Thesis and Dissertation Collection, all items

2020-06

CHARACTERIZATION OF SURFACE ROUGHNESS ALONG THE ROCKY COASTLINE USING STEREO PHOTOGRAPHY TECHNIQUES

Garrett, Jessica A.

Monterey, CA; Naval Postgraduate School

https://hdl.handle.net/10945/65526

NAVAL POSTGRADUATE SCHOOL

MONTEREY, CALIFORNIA

THESIS

CHARACTERIZATION OF SURFACE ROUGHNESS ALONG THE ROCKY COASTLINE USING STEREO PHOTOGRAPHY TECHNIQUES

by

Jessica A. Garrett

June 2020

Thesis Advisor: Derek Olson
Second Reader: Mara S. Orescanin

THIS PAGE INTENTIONALLY LEFT BLANK

REPORT DOCUMENTATION PAGE		*Form Approved OMB No. 0704-0188*
Public reporting burden for this collection of information is estimated to average 1 hour per response, including the time for reviewing instruction, searching existing data sources, gathering and maintaining the data needed, and completing and reviewing the collection of information. Send comments regarding this burden estimate or any other aspect of this collection of information, including suggestions for reducing this burden, to Washington headquarters Services, Directorate for Information Operations and Reports, 1215 Jefferson Davis Highway, Suite 1204, Arlington, VA 22202-4302, and to the Office of Management and Budget, Paperwork Reduction Project (0704-0188) Washington, DC, 20503.		
1. AGENCY USE ONLY *(Leave blank)*	**2. REPORT DATE** June 2020	**3. REPORT TYPE AND DATES COVERED** Master's thesis
4. TITLE AND SUBTITLE CHARACTERIZATION OF SURFACE ROUGHNESS ALONG THE ROCKY COASTLINE USING STEREO PHOTOGRAPHY TECHNIQUES		**5. FUNDING NUMBERS**
6. AUTHOR(S) Jessica A. Garrett		
7. PERFORMING ORGANIZATION NAME(S) AND ADDRESS(ES) Naval Postgraduate School Monterey, CA 93943-5000		**8. PERFORMING ORGANIZATION REPORT NUMBER**
9. SPONSORING / MONITORING AGENCY NAME(S) AND ADDRESS(ES) N/A		**10. SPONSORING / MONITORING AGENCY REPORT NUMBER**
11. SUPPLEMENTARY NOTES The views expressed in this thesis are those of the author and do not reflect the official policy or position of the Department of Defense or the U.S. Government.		
12a. DISTRIBUTION / AVAILABILITY STATEMENT Approved for public release. Distribution is unlimited.		**12b. DISTRIBUTION CODE** A

13. ABSTRACT (maximum 200 words)

High resolution images have been used to estimate and characterize the roughness of the rocky seafloor in terms of small scale roughness and power spectral density. The application of this work is acoustical modeling of scattering from the sea floor. Two camera systems were designed and built to collect images of the ten different types of surfaces along the rocky shoreline on the Monterey Peninsula at low tide. Using commercial photogrammetry software, the images were processed to calculate height Digital Elevation Maps, which were then used to estimate 1-D and 2-D roughness power spectra. A power-law model was fit to the spectrum and had two parameters, the spectral strength and spectral slope. These roughness power spectra parameters were compared to previously collected parameter data on sandy seafloor, and the scattering strength values were compared to recently collected data along the same rocky coastline of the Monterey Bay. The lower-frequency rocky seafloor spectral strength and slope showed overlap with some of the sand surfaces at varying spatial scales. These parameters were used as inputs into a small-scale roughness perturbation theory model to predict scattering strength of the ten different surfaces for a frequency of 200 kHz and three different grazing angles. The predictions using this scattering strength method were within 10 dB of measurements collected within the same area in the Monterey Bay.

14. SUBJECT TERMS roughness, underwater acoustics, rocky seafloor, stereo photography			**15. NUMBER OF PAGES** 113
			16. PRICE CODE
17. SECURITY CLASSIFICATION OF REPORT Unclassified	**18. SECURITY CLASSIFICATION OF THIS PAGE** Unclassified	**19. SECURITY CLASSIFICATION OF ABSTRACT** Unclassified	**20. LIMITATION OF ABSTRACT** UU

THIS PAGE INTENTIONALLY LEFT BLANK

CHARACTERIZATION OF SURFACE ROUGHNESS ALONG THE ROCKY
COASTLINE USING STEREO PHOTOGRAPHY TECHNIQUES

Jessica A. Garrett
Lieutenant Commander, United States Navy
BS, U.S. Naval Academy, 2007

Submitted in partial fulfillment of the
requirements for the degree of

MASTER OF SCIENCE IN METEOROLOGY AND PHYSICAL
OCEANOGRAPHY

from the

NAVAL POSTGRADUATE SCHOOL
June 2020

Approved by: Derek Olson
                Advisor

                Mara S. Orescanin
                Second Reader

                Peter C. Chu
                Chair, Department of Oceanography

THIS PAGE INTENTIONALLY LEFT BLANK

ABSTRACT

High resolution images have been used to estimate and characterize the roughness of the rocky seafloor in terms of small scale roughness and power spectral density. The application of this work is acoustical modeling of scattering from the sea floor. Two camera systems were designed and built to collect images of the ten different types of surfaces along the rocky shoreline on the Monterey Peninsula at low tide. Using commercial photogrammetry software, the images were processed to calculate height Digital Elevation Maps, which were then used to estimate 1-D and 2-D roughness power spectra. A power-law model was fit to the spectrum and had two parameters, the spectral strength and spectral slope. These roughness power spectra parameters were compared to previously collected parameter data on sandy seafloor, and the scattering strength values were compared to recently collected data along the same rocky coastline of the Monterey Bay. The lower-frequency rocky seafloor spectral strength and slope showed overlap with some of the sand surfaces at varying spatial scales. These parameters were used as inputs into a small-scale roughness perturbation theory model to predict scattering strength of the ten different surfaces for a frequency of 200 kHz and three different grazing angles. The predictions using this scattering strength method were within 10 dB of measurements collected within the same area in the Monterey Bay.

THIS PAGE INTENTIONALLY LEFT BLANK

TABLE OF CONTENTS

LIST OF FIGURES

LIST OF TABLES

THIS PAGE INTENTIONALLY LEFT BLANK

LIST OF ACRONYMS AND ABBREVIATIONS

DEM	Digital Elevation Map
FD	Fractal Dimension
ISO	International Organization for Standardization

THIS PAGE INTENTIONALLY LEFT BLANK

ACKNOWLEDGMENTS

I would like to thank Dr. Derek Olson and Dr. Mara Orescanin for their support and encouragement during this thesis process. I would also like to thank Mr. Mike Cook for his technical MATLAB support, without which this thesis would not have been possible. Lastly, I would like to thank my cohort at NPS who provided support throughout the two and a half years that we spent here.

THIS PAGE INTENTIONALLY LEFT BLANK

I. INTRODUCTION AND BACKGROUND

Acoustic systems have become the primary remote sensing tools used in the ocean for both civilian and military activities such as hydrography, anti-submarine warfare, and mine warfare (National Research Council (U.S.) 2007). While most active acoustic sonar systems use frequencies that range from roughly 100 Hz to several MHz (Jackson and Richardson 2007), many active remote sensing instruments use a higher frequency range of approximately 10 kHz to 1 MHz for shallow water applications (Jackson and Richardson 2007). Although many of the measurable environmental characteristics of the water column and seafloor have an impact on underwater acoustic system performance, the physical characteristics of the seafloor are the most significant parameters needed when evaluating and predicting the acoustic detection performance of a system during high-frequency applications. This is especially true in the shallow coastal environment, where acoustic scattering from the seafloor is highly important (Jackson and Richardson 2007).

After the Cold War the acoustic community shifted its scientific focus from deep-water environmental to the shallow water environment, where the characteristics of the seafloor have a much more significant impact on acoustics scattering (Jackson and Richardson 2007). While the shift from deep water to shallow water acoustics brought the littoral region into focus for the acoustics community, the vast majority of the coastal environmental characterization experiments in support of acoustic research have been focused characterizing the roughness of the sandy seafloors. The lack of research in rocky seafloor environments prevents performance estimation, or remote sensing in this type of area. Therefore, more research in rocky environments is required to carry out these activities.

Acoustic scattering is the process in which acoustic waves are temporally and spatially dispersed when they interact with variations of the seafloor height and material properties. Since scattering becomes a primary concern when the surface variations (roughness) scales are on the same order of magnitude as the acoustic wavelength, high-frequency acoustic waves tend to experience high scattering levels when interacting with

small scale surface features that are present across all seafloors (Jackson and Richardson 2007, p. 21).

Scattering strength can significantly impact the performance of a sonar system through either reverberation or changes in the propagation. This can have both positive and negative effects on the performance of the system depending on the application it is being used for. If target detection is the intent, the scattering interferes with the signal received back at the sensor, making the target harder to detect. However, if bottom characterization is the intent, the scattering ensures the signal makes it back to the sensor and the bottom can be mapped, or inferences made about its composition. No matter the intended application, accurately predicting the scattering strength allows for better application and performance of the acoustic system being used (Jackson and Richardson 2007, p. 1, 171). Since scattering strength is directly related to surface roughness, large datasets are necessary to establish roughness trends for individual environments such as the sandy seafloor or rocky coastline. These trends can then improve environmentally adaptive target detection algorithms, and performance estimates of the systems (Stack 2011).

While roughness is one of many seafloor characteristics that impact the performance of an acoustic system, other factors include material composition, density, and porosity. Not all of these relevant characteristics have been well-studied for every possible seafloor environment. Surface roughness is one of the areas of study with significant data gaps in varying environments, despite the fact that it is one of the most significant factors in shallow water underwater acoustic scattering in the high-frequency range (Jackson and Richardson 2007). Surface roughness is generally understood as the variation in the surface features. A rough surface is marked by discontinuities or ridges. In other words, it has a bumpy or uneven surface (Merriam-Webster, n.d.). Many of the seafloor and coastal surfaces in and around the ocean are rough. These physical characteristics that make up the roughness parameters of the various seafloors exist on different spatial scales. These scales vary from the very large mid-Atlantic Ridge, with widths of up 1500 kilometers protruding upwards of 2 to 3 kilometers from the abyssal plain, to the meter wide sand bars created by surface wave action and the centimeter-sized pits created by fish living near the seafloor (Jackson and Richardson 2007, p. 171). In

general, the features that make up the larger scale roughness along the seafloor are more stable, meaning that they do not change significantly over short periods of time. However, the features on the smaller end of that spatial frequency range tend to be less stable, changing over the course of hours to days (Jackson D.R. et al., 2009), (Jackson and Richardson 2007, p. 171), (Lyons, A.P, Brown, D.C, 2013) . Large-scale features are generally easier to identify and measure through basic hydrographic survey techniques used to map the ocean floor. Small scale features are more challenging to resolve and generally depend on statistical characterization, which means there are multiple techniques used to parameterize the roughness of a surface at these scales depending on the scientific application (Jackson and Richardson 2007). High-frequency acoustic applications between 10kHz and 1 MHz are impacted by roughness parameters that are on the same or smaller scales than their associated wavelengths of 15 cm and 1.5 mm, respectively.

Analysis of the surface roughness is often done using a roughness power spectral estimate of either a cross section (1-D) or a plane (2-D) of a height field of the surface. From the roughness power spectrum, acoustic parameters of the surface can then be identified. Two of the most prevalent acoustic parameters with respect to surface roughness characterization are the 1-D spectral intercept $\left(\phi_1\right)$ and the 1-D spectral slope $\left(\gamma_1\right)$. These two parameters are estimate by applying a power-law model, a straight line in log-log space, to the regression portion of the plotted roughness power spectrum which is derived from a cross section or slice of a surface (z(x) or z(y)). The parameter values for the 1-D spectral intercept $\left(\phi_1\right)$ and the 1-D spectral slope $\left(\gamma_1\right)$ were ascertained from the slope and intercept of power-law fit lines that were applied to the regression each spectrum.

In all the spectra plotted, a break in the slope was identified, creating two distinct portions of the regression of the spectra. Therefore, to best characterize the spectral parameters in this study, a power-law line was fit to each section and the spectral parameters were estimated for each section. An example of this can be seen in Chapter II, Figure 13. The presence of two different slopes may indicate that different processes may be responsible for the roughness. For example, on a rocky surface, very high spatial frequencies may be related to the grain scale of the granites. When identified and analyzed

3

together, these parameters can help to statistically characterize the variation of the surface roughness across a range of spatial frequencies on the surface that is being analyzed.

These two 1-D parameters can also be converted to their equivalent 2-D parameters for input into acoustic scattering models (Jackson and Richardson 2007). These parameters are useful in scattering models since the scattering cross section is proportional to the power spectrum evaluated at the Bragg wavenumber (Jackson and Richardson, 2007). A more detailed discussion on how these values are calculated and how they are used in the perturbation theory scattering model can be found in the data processing section of Chapter II but it is relevant to identify both the 1-D and 2-D parameters now as many of the previous studies referenced in this chapter used these parameters to characterize the roughness of the seafloor and these will be the primary parameters utilized for roughness characterization in this experiment.

The following sections will provide a brief background of the roughness characteristics, and associated parameters and methods by which this data collection was conducted for the sandy seafloor and rocky seafloor environments in recent decades. The measured values of scattering strength and means of collection for these environments will also briefly be described. These sections serve to provide a foundational understanding of what has been measured and how it has been collected to date in these environments, for both roughness parameters and their associated scattering strength values.

A.   ROUGHNESS CHARACTERISTICS OF THE SANDY SEAFLOOR

Given that roughness exists at a range of spatial scales, a sandy seafloor can actually be characterized as having significant roughness at smaller, on the order of cm to mm, scales. Many small-scale roughness features on the sandy seafloor are created by movement in the water, primarily caused by waves and tidal currents, as is the case for sand bars, ridges, and ripples (Jackson and Richardson 2007, p. 60). Additionally, they can be created through the presence of small animals or other biological processes such as the mounds, craters, or pits created by small fish or the trails and burrows created by various small creatures that reside along the seafloor (Jackson and Richardson 2007, p. 171). Since these features are created and altered by the dynamic forcing due to currents and waves or

by biological organisms and processes, they are constantly changing. These changes can occur over the course of minutes to days, with some of the largest features, such as sand bars changing slightly slower, over weeks to months (seasonally) (Jackson D.R. et al. 2009), (Jackson and Richardson 2007, p. 171; Lyons, A.P, Brown, D.C 2013) .

With the small-scale features associated with the sandy seafloor being inherently time-varying, measuring and characterizing them in a way that is beneficial to acoustic applications is challenging. Below are a few summaries of experiments that were designed to conduct the type of roughness measurements and parameter characterization required for acoustic model application.

1.   Sandy Seafloor Roughness Parameter Collection – Previous Studies

In the past few decades, numerous studies have collected and characterized roughness in sandy environments in support of acoustic applications. Twelve of these studies are presented in (Jackson and Richardson 2007), which does not encompass all studies conducted in this field, but does present a useful data set in which to analyze. A brief description of three of these studies follows.

One of the earliest studies performed to collect and classify microscale roughness parameters of the seafloor in support of acoustic applications was conducted in 1989 (Briggs 1989). During this study, various sediment morphologies from flat to rippled surfaces were measured using stereo photogrammetry. From these height measurements, roughness power spectral density was calculated. This study concluded that various sediment types changed the power spectrum characteristics. Specifically, the spectral slope (γ_1) varies with sediment type and spatial frequency of the surface features. The effects of varying sediment types and spatial frequencies were evident across the spectrums, indicating that one single spectral model would not suffice to characterize all three of the locations analyzed in this study (Briggs 1989).

As cameras and photogrammetry techniques improved, more studies were conducted using this method to measure seafloor roughness parameters in the sand environment at progressively higher resolutions. In 2002, (Lyons et al. 2002) conducted an

experiment with resolutions between one millimeter and one meter on sediment surfaces in shallow water using digital photographs, as opposed to the analog methods of Briggs 1989. This study found that if a surface is dominated by directionally specific features (such as ripples in the case of this experiment), the 1-D spectral exponent (w_1) and spectral slope (γ_1) parameters will not provide a complete characterization of the seafloor. Instead, they found that a two-component spectrum derived from the combination of a isotropic (meaning there are no directionally specific features) (Jackson and Richardson 2007) power-law component and a non-centered Gaussian component would provide a better characterization of the 2-D environment that has direction-specific features (Lyons et al. 2002).

In 2004, Richardson et al. performed a study using divers and stereo photography techniques to analyze the roughness and associated scattering strength by making deliberate directional modifications to the sandy seafloor surface. Photographs were collected before and after the modification of the seafloor with follow up photographs collected at 12-hour increments after the modification. This study had an effective resolution of about one millimeter horizontally and vertically. Analysis of the measurements included the calculation of 2-D power spectra and associated roughness parameters of w_2 (spectral strength) and γ_2 (spectral exponent), which will be discussed in Chapter II. In general, this study found the spectral slope varies between -2.6 and -3.3 with a larger variation of spectral exponent values between $0.31*10^{-5}\,m^{(\gamma_2-1)}$ and $16.40*10^{-5}\,m^{(\gamma_2-1)}$ as the roughness varied through time. While already quite variable parameters, this study showed the potential for variability of spectral parameter values as the surface roughness changed, even a short period of time due to biological forcing. It also highlighted the need for more information on how the biological processes impact surface roughness and associated acoustics scattering. While values like this are not necessarily be directly applied to the rocky seafloor, they provide a valid comparison of values at small spatial scales as more roughness data along the rocky seafloor is collected.

B.   ROUGHNESS CHARACTERISTICS OF THE ROCKY SEAFLOOR

The rocky seafloor is composed of features that span a wide range of spatial and temporal scales. From the large-scale tectonic features of the ocean basins to the biological life that exists across the reefs, in the sand, and on the rocky outcroppings near the coast, the composition of this environment varies significantly, therefore one can expect that the roughness of this environment will vary considerably as well (Jackson and Richardson 2007). While the small-scale features will play the most significant role in high-frequency applications, it is important to understand the entirety of the environment to best predict the potential impacts on the acoustic system being used. The next few paragraphs will describe both the large and small-scale characteristics that are typical of the rocky seafloor environment.

1.   Rocky Seafloor Roughness Parameter Collection – Previous Studies

Two relatively recently conducted studies used updated stereo photography techniques to characterize the surface roughness in environments other than the sandy seafloor. First, in 2015, (Leon et al. 2015) utilized these techniques to characterize an underwater coral reef environment. While not exactly equivalent to a rocky shore, this environment has many similarities to a rocky shoreline environment since both have dynamic biological processes and significantly more structural variation than a sandy seafloor. Collecting photographs along a transect, they were able to resolve roughness features at the submillimeter scale using diver hand-held cameras and commercial photogrammetry processing software. Through processing, they were able to characterize the environment through various types of roughness measurements. The study found that the variations across the different surfaces of the reef correlated best with the Fractal Dimension parameter (Leon et al. 2015).

Olson et al. (2016) conducted an acoustically focused study using these photogrammetry techniques characterize the roughness of rock outcrops as part of a larger experiment to measure high-frequency acoustics scattering within a rock dominated environment. Using similar stereo photography techniques to previous studies done in sand, data were collected subaerially on rock surfaces that displayed various surface

structures, like those discussed above in for the large-scale roughness features of the rocky seafloor.

This study found that roughness data collected above the waterline could be applied to the same surfaces underwater without affecting acoustics scattering measurements at high frequencies, due to the extreme resistance of the rock material to chemical weathering. The calculation of 2-D power spectrum and power-law fits for the two distinct surface types produced roughness parameters of γ_2 (spectral slope) and w_2 (spectral exponent). These values were then applied to relative acoustic scattering strength models (Olson et al. 2016). The spectral parameter values found by (Olson et al. 2016) provide a comparison data set to the data collected for this paper as both data sets were conducted in an area dominated by granite outcroppings in the aerial environment.

C.   SPECTRAL PARAMETERS FROM PREVIOUS STUDIES

To date, there is not a significant amount of data available regarding the spectral parameters measured during previous studies. Figure 1 shows some of the available data (Jackson, 2020).
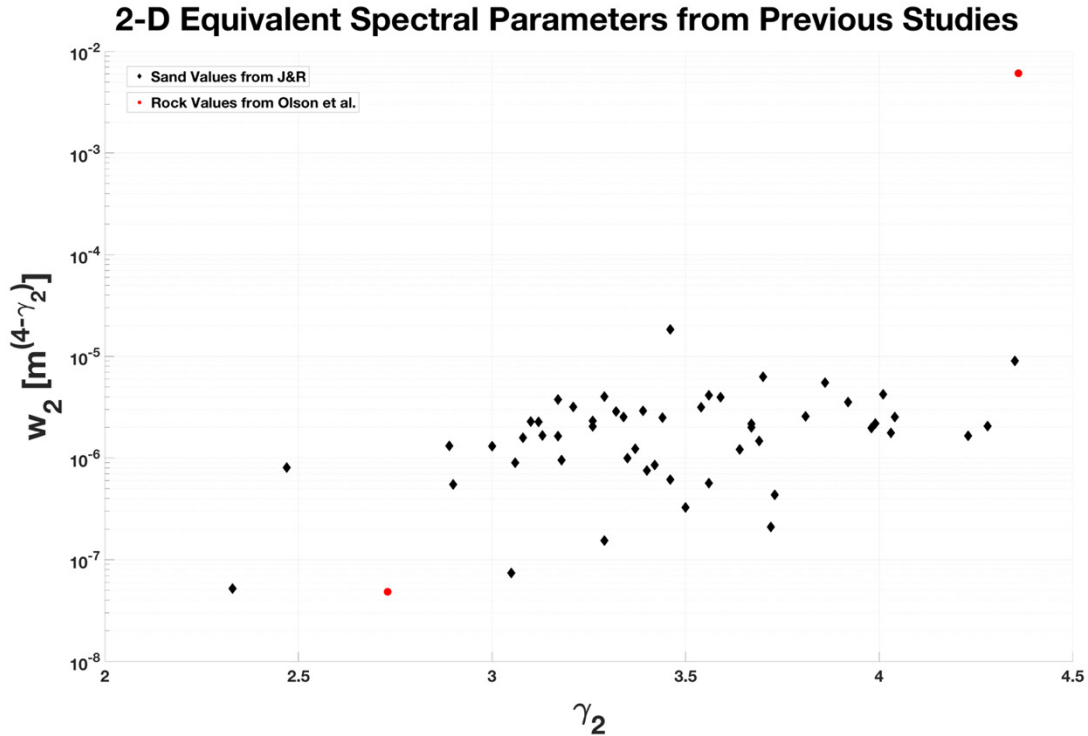
Scatter plot showing sand and rock 2-D spectral equivalent values from sand and rock environments. In the legend, J& R stands for (Jackson and Richardson, 2007). The sand data was taken from Table 6.1 in Jackson and Richardson (2007) and converted to the 2-D values. rock values were pulled directly from Olson et al. (2016). The sand values are depicted by black diamonds while the rock values are depicted by red dots. Derived from Jackson and Richardson (2007) and Olson et al. (2016).

Figure 1.   2-D Equivalent Spectral Parameters from Previous Studies

The sand spectral parameter values were derived from a study conducted by Briggs (2002) and consolidated within Jackson and Richardson (2007). These 1-D values were converted to their 2-D equivalent values through the use of equations that will be discussed in Chapter II. These values, while not all encompassing for data available on the sandy seafloor, serve a good reference for the values that have been collected in the sandy seafloor environment. Even less data exists on the spectral parameters within the rocky seafloor environment. The two data points (red dots on the plot) for rocky spectral parameters are from Olson et al. (2016). These data points serve as a valid reference points for this study given that experiment was conducted over rock surfaces with similar composition to the rocky outcroppings found within the Monterey Bay, which will be discussed in a later section of this chapter.

Understanding the roughness parameters alone is not necessarily effective when trying to understand how roughness will impact sensors or systems. Therefore, these parameters need to be applied to models that can predict scattering strength in in order to increase performance. Since scattering strength is that measure for this experiment, the next section will discuss the correlation between roughness and scattering strength and why that is important to understand.

D.   SCATTERING STRENGTH AND SURFACE ROUGHNESS RELATIONSHIP

As noted previously in the introduction, the roughness characteristics of the seafloor at the centimeter to millimeter scale play a primary role in scattering for high-frequency acoustics systems in the shallow water environment. When an acoustic signal is incident upon a portion of the seafloor that is composed of roughness variations along the same scale as the signal wavelength, the incoming sound energy will scatter in multiple directions as depicted in Figure 2.
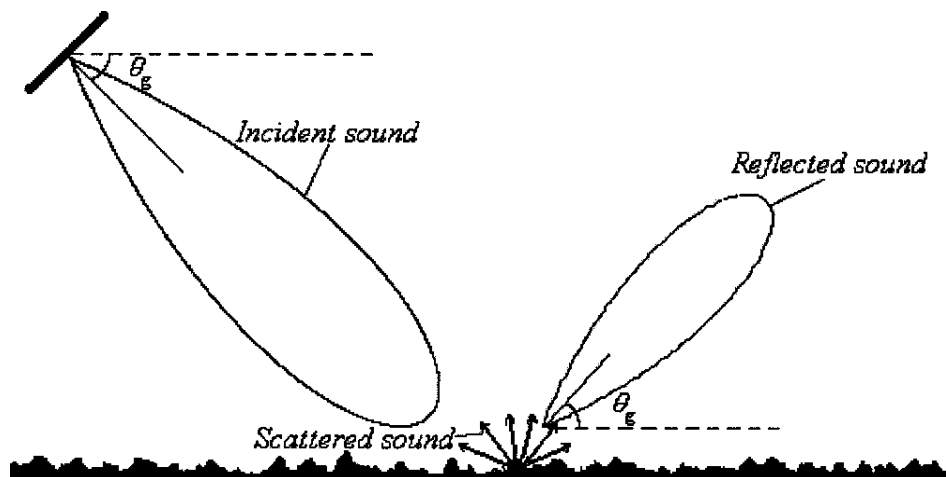
Depiction of incoming and scattered sound waves along a rough surface. Source: (Oelze et al. 2002)

Figure 2.   Depiction of Scattering from a Rough Surface

Scattering strength is defined as the ratio of scattered intensity to the incident intensity with spherical spreading and the ensonified area removed. Under the small

roughness perturbation approximation method used in this study, the scattering strength is proportional to the 2-D roughness power spectral density evaluated at the Bragg wavenumber, which for backscattering direction is $2k_w \cos(\theta_i)$, where $k_w = \dfrac{2\pi f}{c_w}$ is the wavenumber in water, f is the acoustic frequency, and c_w is the acoustic speed of sound in water (Jackson and Richardson 2007). In order to understand the scattering effects and estimate acoustic performance in the near-shore environment, it is imperative that roughness characteristics of any given environment are quantified and the associated scattering strength of the acoustic system(s) that will be used is estimated.

1. Scattering Strength on Sandy Seafloors

To date, there have been numerous studies on roughness characteristics and associated acoustic scattering for sandy seafloors, the twelve studies described in (Jackson and Richardson 2007) encompass a significant portion of these studies that directly consider the connection between scattering strength and roughness parameters. Many of the earlier studies conducted to assess scattering strength either did not sufficiently characterize the seafloor environment when measuring the scattering strength. Other studies conducted lacked resolution or refined calibrations techniques, making their data less useful for comparison at the high resolution required when considering high-frequency acoustic applications (Jackson and Richardson 2007). These limitations on data notwithstanding, (Jackson and Richardson 2007) illustrated the variation in scattering strength over the multiple experiments through multiple scatter plots. Using the Lambert Law curves fit to the plots at a 45° grazing angle (for reference) the scattering strength along that curve for sand was -25 dB. The scattering strength for gravel was also estimated and may provide a good comparison to data in this study since the grain size of gravel is larger than the grain size of sand, and gravel is commonly found in areas around the rocky outcroppings within the Monterey Bay, which will be discussed in the next section. For the data collected over gravel seafloors, a 45° grazing angle produced a scattering strength of approximately -15 dB along the Lambert Law curve. It should be noted that scattering

strength also varies with frequency and should be considered if various frequencies will be used in an analysis (Jackson and Richardson 2007, p. 321–330).

2. Scattering Strength on Rocky Seafloors

Relative to the sandy seafloor environments, there have been fewer studies conducted to measure scattering strength in the nearshore or underwater rocky environment While there have been seven total studies conducted, only five have successfully collected scattering strength data in rocky environments that can be reliably used for comparison purposes when roughness based estimates are made (Gruber, 2019). These studies include: (Urick 1954), (McKinney and Anderson 1964), (Soukup and Gragg 2003), (Olson et al. 2016)) and (Gruber 2019). There is also a relatively small data set analyzing rocky seafloor scattering strength in (Jackson and Richardson 2007). In that data set, a 45° grazing angle produced a scattering strength of approximately -10 dB at the curve fit to Lambert's Law, but the values in this data showed significant variability when compared to the sand data that was analyzed in the same manner (Jackson and Richardson 2007, p. 324–325).

E. DESCRIPTION OF THE MONTEREY BAY

As discussed previously in the rocky environment roughness section, there are both large-scale, hundreds of meters to kilometers, and small-scale, sub millimeters to meter, features that impact acoustic scattering in the rocky environment.

1. Large-Scale Features of the Monterey Bay

The Monterey Bay is a crescent-shaped bay along the central coast of California with the Monterey Peninsula located on the southern tip of the Bay and its western coast exposed to the Pacific Ocean. Geologically, the Bay is located on the Salinian Block formation and was the site of a geological study conducted by Greene (1977). The portion of the Block that lies beneath the Monterey Bay is broken into multiple pieces by fault lines that primarily run northwest to southeast. The Monterey Peninsula itself resides on a sub-block identified as the Monterey Block. Within the Monterey Block two smaller fault lines run along the peninsula's northeast and southwest coasts in the same direction as the larger fault lines in the region. The faulting processes within the Bay and around the peninsula

have created significant rocky outcroppings along the coast. Eittreim et al. (2002) analyzed additional surveys conducted within the Monterey Bay and noted a highly variable, rough, knobby and fracture pattern on the granite outcroppings along the coast. These outcroppings along the shelf run continuously from offshore to onshore. Thus, the assumption can be made that the structure observed in the underwater imagery is similar, if not the same, to the structure within the nearshore and intertidal environments along the coast of the Monterey Bay (Eittreim et al., 2002).

The Salinian Block, which is partially exposed due to the faulting activity, consists primarily of granite and is overlaid with various sediment types including mud, silty sand, course sand, and gravels (Greene, 1977), (Eittreim et al.). During the geological survey in 1977, Greene collected multiple samples from the rocky outcroppings on the shelf and offshore along the coast of the Monterey Peninsula. The rock samples collected just to the west of the Monterey Peninsula, closest to the two coastal locations used for this experiment, were comprised of very angular granodiorite rocks and a few semi-rounded boulders. The overall shape, structure, and variability of the outcroppings within the Bay can be discrete scatterers for mid-frequency, 1 to 10 kHz, systems. However, depending on the scale, the physical characteristics (angularity and facet structures) of the rocks within the outcroppings will also have an impact on high-frequency acoustic systems due to changes in the local grazing angles caused by the larger scale features of the outcroppings.

2. Small-Scale Features of the Monterey Bay

While the rocky outcroppings along the coast make up the mid to large-scale features, the sediments, covering portions of the rocky outcroppings and seafloor as well as the small-scale biological organisms in the region will impact the roughness characteristics of both the seafloor and surfaces of the rocky outcroppings along the coast of the Bay and Peninsula.

As noted above, portions of the seafloor in Monterey Bay are covered by various sediment types. In addition to rock samples, (Greene, 1977) also collected sediment samples along the west coast of the Peninsula. Samples collected closest to the two

locations selected for this experiment showed a mixed composition of medium to course-grained granitic sand and fine-grained silty sand (Greene, 1977).

Upwelling in the region, caused by the reoccurring wind patterns and eastern boundary current that runs northwest to southeast along the west coast of the United States, where the Monterey Bay and Monterey Peninsula are located, creates a superb environment for biological life. The upwelling causes cold, nutrient-rich water from near the seafloor to be pushed upwards into the water column toward the ocean surface, creating an environment for biological life such as plankton, seaweed (kelp), and other animal and plant species to flourish (NOAA).

The Monterey Bay is well known for its diverse biological environment and has been designated as National Marine Sanctuary (NOAA, 2019). Biological life ranging in size from microscopic plankton to the giant blue whale reside in the Bay. Considering the upwelling characteristics and diversity of biological life found in this region, it is no surprise then than the rocky shores of the Peninsula are teeming with a variety of plant and animal life of all shapes and sizes. During the survey conducted by Greene (1977), significant biological presence, in the form of bryozoans, calcareous worm tubes, and barnacles, was noted on the rock samples collected in off the west coast of the Monterey Peninsula near the locations selected in for this experiment (Greene, 1977). This means that we can expect that the biological organisms found within the Bay can also be found on or around the rocky surfaces, impacting their roughness characteristics and ultimately the scattering strength.

Given the physical and biological features present in the area, the Monterey Bay is a superb example of a rocky environment that showcases the spectrum of large- and small-scale features that a rocky coastline can have. For these reasons, the Monterey Bay provided an excellent location for research focused on measuring and characterizing the roughness characteristics of a rocky coastline.

F. GOALS AND INTENT OF THIS STUDY

With markedly fewer data collected within the rocky environment, identifying techniques and environmental data, such as roughness, is critical to the future performance

of underwater acoustics systems in the nearshore rocky environment. Therefore, this experiment was designed with the goal of collecting rough surface parameters in the rocky environment of the Monterey Bay through the use of flexible stereo photography techniques and modern computer vision software. Since seafloor roughness is a dominant factor in acoustics scattering in the shallow water environment, the measured roughness parameters will be used to investigate the potential scattering impact that the measured surface roughness parameters have on high-frequency acoustics systems.

Chapter II describes the methodology used for this study to include equipment selection and design as well as data collection and data processing techniques. Chapter III presents the results and a discussion of the findings. Chapter IV provides conclusions.

THIS PAGE INTENTIONALLY LEFT BLANK

II. METHODOLOGY

In this chapter, the methodology used throughout the study is described. Section A outlines the overall methodology of the experiment, Section B discusses the equipment used, Section C covers data collection, and Section D details the data processing and analysis techniques used. Since the experiment used a combination of camera setups, data collection, and post-processing techniques similar to previous experiments conducted in similar manner, background details from the experiments that were also designed to collect and process multiple photographs in a rocky area along the coast will be discussed throughout the various Sections. All the methods used in this experiment were selected with the intent of identifying a fast, portable, and effective method to obtain roughness parameters of the rocky seafloor for acoustic applications.

A. OVERALL METHODOLOGY

The fundamental methodology for these experiments were as follows:

- Equipment Selection and Design

    a. Determine Equipment and Setup: Working with a local underwater camera and dive store, cameras and equipment were selected that would meet the requirements of our experiment and work best in the local area.

    b. Design and Test Equipment Setup: A portable frame was built to hold the selected camera equipment. The frame was tested in multiple environments to determine the best collection setup for the coastal environment it was to be used in.

- Data Collection

    a. Collect Data: Photographs were taken at multiple angles and elevations over ten different surface types along rocky areas on the Monterey bay coast with either dual mounted cameras on a portable PVC

frame or with a handheld single camera. A reference object was placed on or near each surface as photographs were taken for use during post-processing. Data was collected at two locations during low tide events on the coast of the Monterey Peninsula.

- Data Processing

a. Process Images and Produce Digital Elevation Maps (DEM): Images were processed using commercial software (Agisoft LLC 2020) to produce a digital elevation map (DEM) for each surface and height fields were exported from each DEM in the form of (x, y, z) coordinates.

b. Select Data for Processing and Estimate Power Spectral Density: The height fields for each surface were cut into 0.1m by 0.1m sections for processing due to processing capacity. MATLAB was then used to estimate the 1-D power spectral density of each section in the local x and y directions using a traditional averaged spectrum, and the multitaper method. Estimates of the 2-D spectrum were performed as well.

c. Fit Power Law Models (straight lines in log-log space) to determine ϕ_1 (Spectral Intercept) and γ_1 (Spectral Slope) of each spectrum: Using the power law model, lines were fit to the two distinct regression sections on the power density spectrums of the ten surfaces to determine the spectral parameters of each section (Jackson and Richardson 2007).

d. Predict Scattering Strength using the Small Roughness Perturbation Model: All the derived ϕ_1 and γ_1 parameters were converted to their equivalent 2-D components and run through scattering strength formulas that utilized the small roughness perturbation estimation technique for scattering strength calculations (Jackson and Richardson 2007) to determine the potential scattering strength of each surface type.

18

e. Plot Data and Analyze Data: Data was plotted in MATLAB using various methods to allow for analysis and comparison.

The steps outlined above will now be discussed in further detail, starting with the equipment selection in Section B. While there may be variations that could be made to these steps based on the desired end state, this process is easily repeatable for future data collection in the rocky coastal environment.

B.   EQUIPMENT SELECTION AND DESIGN

The equipment used to collect data for this experiment included a portable, dual-camera mounted system constructed from PVC pipe and a single handheld underwater camera, both of which required an external reference object. Variations of these types of techniques have been used previously to measure seafloor roughness in support of acoustic scattering experiments (Briggs 1989), (Richardson et al.), (Briggs et al. 2002), (Lyons et al. 2002), and (Tang 2004). The earliest of these studies conducted in support of underwater acoustics was Briggs (1989), where analog cameras and an optical stereocomparator were used. More modern experiments, such as (Lyons et al. 2002), used dual-camera setups like Figure 3.
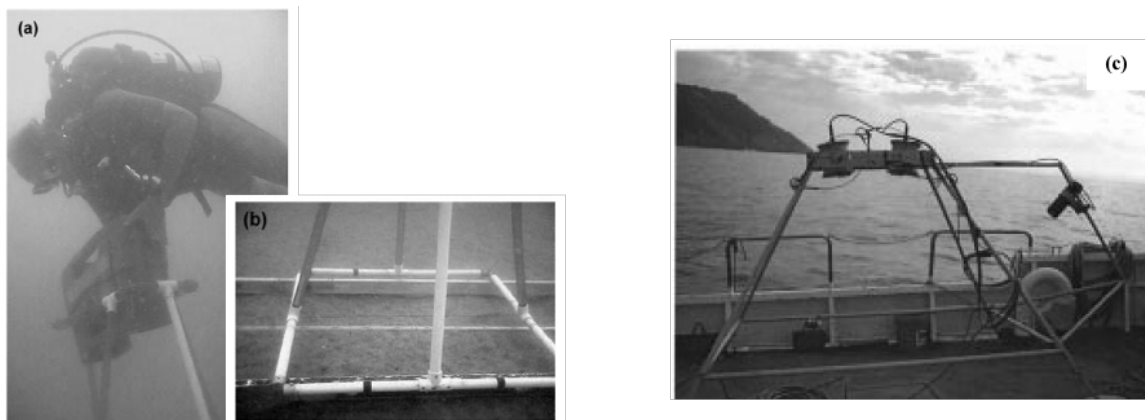
Pictures (a) and (b) show the diver handheld setup utilized in 2002 near Fort Walton Beach Florida. Source: Briggs et al. (2002). Picture (c) shows a larger set up utilized in 2002 near Elba Island, Italy. Source: Lyons et al. (2002).

Figure 3.   Previous Stereo Photography Experiment Setups

Traditional photogrammetry techniques rely on the very specific arrangement of the cameras to utilize geometry to convert the coordinates of the pixels in the captured images to object coordinates. Figure 4 shows the geometry and associated equations used in this type of camera setup. By identifying the same pixel in both images, the disparity between the pixels can be quantified. Using that value and the known values of the focal lengths and camera baseline, similar triangle geometry can be used to determine the height (z coordinate) of the object/point of interest.

Left Camera   Right Camera

O_L

B

O_R

f

(x^L_p, y^L_p)

(x^R_p, y^R_p)

H

(x, y, z)
Coordinates of
Object of Interest

O_L & O_R = Left and Right Image Origins

f = Camera Focal Length

B = Camera Baseline

H = Height of Object

$\left(x^R_p, y^R_p\right)$ & $\left(x^L_p, y^L_p\right)$ = Pixel Coordinates

Pixel Disparity

$$d = x^R_p - x^L_p$$

Object Coordinates

$$z = \left(\frac{fB}{d}\right)$$

$$x = \frac{\left(P_{xL}\right)}{B}$$

$$y = \frac{\left(P_{yL}\right)}{B}$$
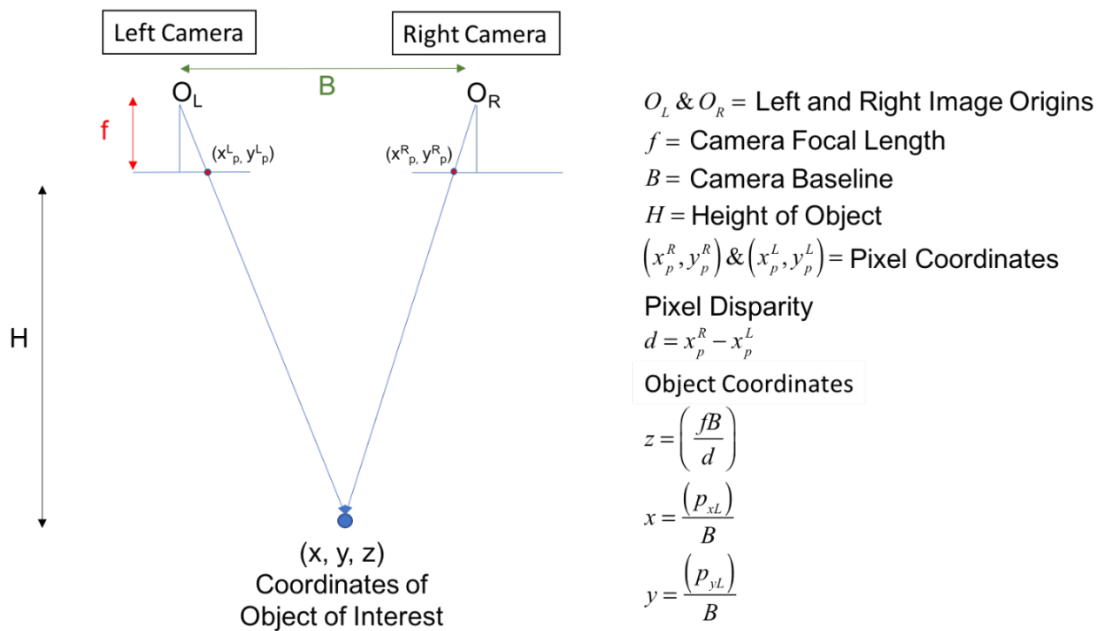
Diagram of traditional stereo photography geometry. Object coordinates can be derived from similar triangles using the equations for pixel disparity and the object coordinated. Adapted from Olson (2014).

Figure 4.   Stereophotogrammetry Setup Geometry and Equations.

Due to the precise geometry specifications required for these types of height measurements, previous studies that used this technique required frames to be constructed and cameras to be mounted at angles that allowed for significant overlap of pixels (for disparity calculations) between the two photographs being taken at the same time, or close to the same time, as depicted in Figure 5. Additionally, the cameras and set up needed to be calibrated using a checkerboard pattern to ensure that the images were not skewed or

distorted and the same focus that was used in the calibration was used in the measurement, which is essential when using this technique to gather elevation/height data. Photographs were then processed in camera pairs (right and left) along multiple views of the target area in order to calculate the height field of a given region. This technique was primarily used to collect data on sandy sea floor environments and requires high water clarity and minimal movement of the camera frame. Previous studies that used this or similar photogrammetry setup techniques include (Richardson et al.), (Briggs et al. 2002), (Lyons et al. 2002), and (Tang 2004).
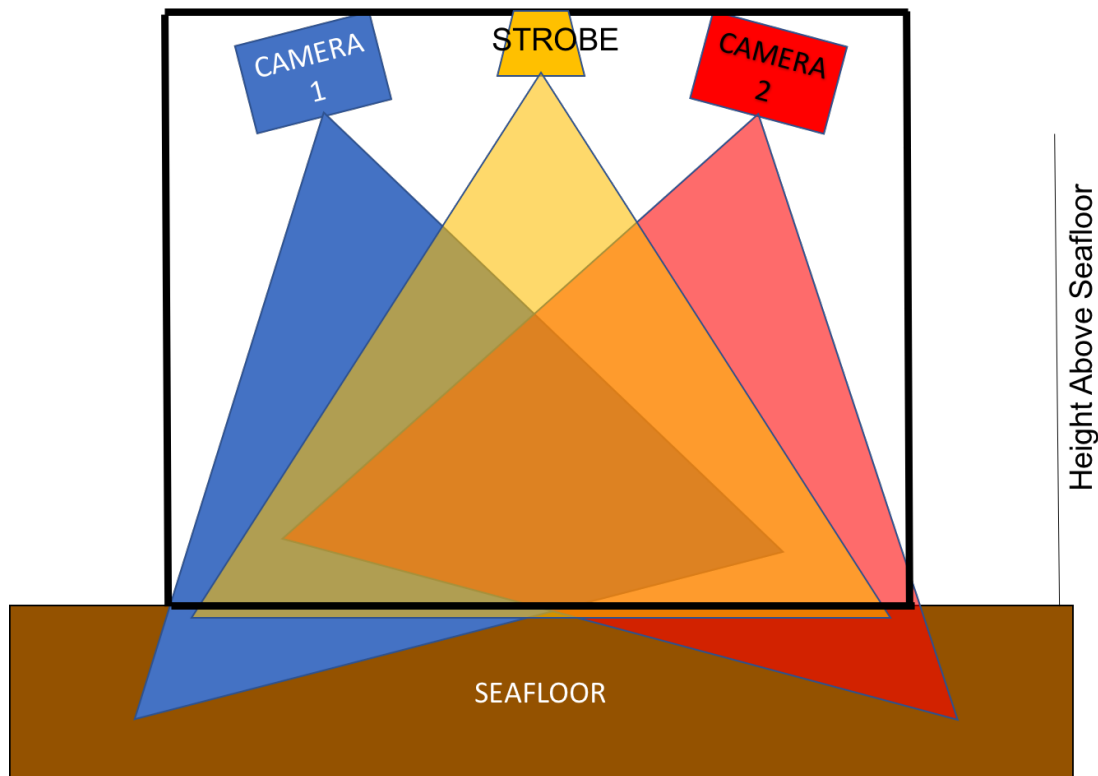
Camera footprint diagram representative of traditional stereo photography set ups.

Figure 5.   Traditional Stereophotogrammetry Setup Camera Footprint
Diagram

Olson et al. (2016) used a variation of this technique to characterize the roughness of glacially eroded rock surface with prominent surface variations. This study used a frame and two cameras, calibrated by a checkerboard pattern to collect stereo photography data

and derive height fields much like previous studies. This study, however, focused on the collection of the height field for characterization of roughness parameters along a rocky coast as it could be applied to underwater acoustics scattering. Additionally, this data collection was conducted fully in-air, much like the method used to collect data in this paper, but without the presence of the biological diversity (kelp, algae, grass, mussels, etc.) that was found along the Monterey coast.

More flexible photogrammetry techniques were used by (Leon et al. 2015) where photographs were collected along a line of coral reef and the image data was processed using commercial software. For this data collection method, two handheld cameras were deployed by a diver to continuously collect side-by-side photographs with significant overlap over a 250 m long coral reef transect. For scaling purposes, lead weights, with known measurements, were places along the transect and a plastic disc was placed at the beginning and end of the transect to be used as georeferenced points during post-processing. The commercial software was then used to build the digital terrain model (height fields) for the transect simultaneously with estimated camera locations and camera parameters. Select sections of the digital terrain model along specific areas of the transect were then analyzed to calculate various roughness parameters in post-processing. Both the handheld data collection method and commercial software used in (Leon et al. 2015) are similar to the methods used during the data collection and post-processing portions of this study.

By taking advantage of modern photogrammetry software that uses algorithms to simultaneously estimate height and camera position, with enough data, and improvements in photography technology, such as camera size and resolution, previously used techniques that required large setups and detailed calibration processes to obtain mm scale resolution can be simplified to the use of a handheld camera and a reference object. Below is a list of the equipment that was selected for this experiment. Ultimately, the camera and housing were used for aerial photo collection during low tide with a square wooden block used as a reference object.

1. **Equipment Specifications**

The following section provides the specifics on the equipment that was tested and used for data collection and post-processing during this study.

- Cameras

    Olympus TG-6 waterproof cameras used for the experimental set up were selected for their size, resolution, and specifications. The camera, without the housing, measures 113 mm wide, 66 mm height and 32.4 mm deep, weighing in at about 253 grams. The TG-6 has both USB and HDMI connectors and is GPS enabled. This camera has a resolution of 12 megapixels and produces RAW images 4000x3000. The focal length of the camera can be adjusted from 4.5 mm to 18 mm and shutter speed ranging from ½ to 1/2000 second (Olympus).

- Housing

    The underwater housing for the TG-6 is constructed out of polycarbonate and is waterproof to depths of 147 feet. Various ports allow connections to made from the camera to the strobe lights via fiber optical cable. The housing also has tripod/mounting sockets for mounting onto equipment set up frame (Olympus).

- Strobe Lights

    The YS-D2J underwater strobe was selected for its portability and strength. It is waterproof to depths of 100 m, has a beam angle of 80°x80° without the use of a diffuser, and a guide number of 32. This strobe also has a recycle time of 1.5 seconds which allows for sequential photographs of the same features in very small timeframes at different angles. Fiber optic connects allow the strobe to be connected and synced with the TG-6 cameras (Sea & Sea).

- Connection Cables

    Optical cable was selected to sync the strobe lights with the cameras for underwater use. These optical cables can stretch to vary with the setup width and allow for the underwater cameras to be used in darker underwater environments if necessary (AOI).

- Equipment Frame

    A frame for the cameras and strobe lights was constructed out of PVC pipe and handlebar camera mounts. This allowed for the cameras to be mounted and connected to strobe lights as required for operation above and below the surface of the water. The frame was light weight, portable and adjustable to house both cameras and strobes, only cameras, or singular camera set ups.

- Reference Block

    A reference object was used to build a local coordinate system within the photogrammetry software. For this experiment, a square wooden block from a children's block set was selected. This object's sides were easily identifiable within the photographs and could be measured using digital calipers to within a 100th of a millimeter. The block dimensions were 44.5 mm on each side.

C. DATA COLLECTION

This section describes all aspects of data collection for this study including collection locations, collection times, and collection methods.

1. Data Collection Locations

Data for this experiment were collected along the coast of Pacific Grove, California in areas where there were accessible rocky outcroppings and significant biological presence at low tide, as discussed in Chapter I. Data collection consisted of taking multiple sets of

photographs of the exposed rocky coastline at low tide. Each set encompassed morphologies that comprise the rocky coastlines. The surface types that were collected in this experiment were: algae, anemone, barnacle, grass, moderate/mixed rock, mussels, kelp, urchin, smooth rock, and gravel. The surfaces like kelp, algae, and grass were included because they are generally attached to the rock dominant surfaces and readily found along the rocky coastline. However, once submerged, these materials scatter and attenuate sound more as 3-D heterogeneities within the volume than as seafloor roughness scatterers, especially at frequencies greater than 1 kHz (Ballard et al. 2020). These surfaces are nonetheless important to understand and characterize because not only are they a significant biological feature in this environment, but in both the aerial and submerged environments, they can have an impact on surface roughness and as well acoustic scattering strength at some level.

The two locations chosen for data collection were Asilomar Beach and Point Lobos. Figure 6. shows the two locations in reference to the Monterey Peninsula with insets of images showing what those two locations looked like at low tide. Both of these chosen locations were on the ocean side of the peninsula, as opposed to the bayside meaning they were more exposed to wave and tidal influence. These locations were chosen based on the accessibility on foot to the rock formations that were exposed at low tide as well as the wide range of surface types (biological and geological) present in those areas, which allowed for maximum data collection of various during low tide events.
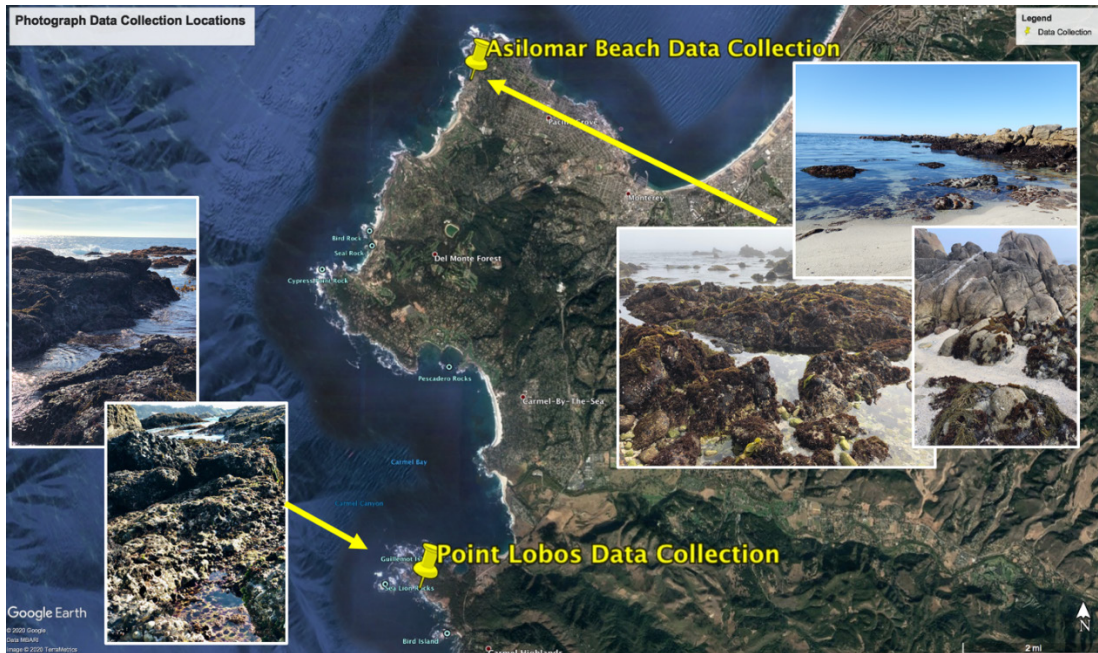
Google earth representation of the two data collection locations, Asilomar Beach to the north and Point Lobos to the south. The insets depict some of the features present at each location at low tide. Adapted from Google (n.d.)

Figure 6.   Data Collection Locations.

While the majority of the data collection was done in the air to minimize the noise in the images collected—which will be discussed in the next sub-section—Data Collection Time, a small dataset for underwater rocks was collected in the deep tide pools for underwater/above water dataset comparisons. More discussion on the determination to primarily collect photographs in the air, versus underwater, can be found in the Chapter I and the next section of this chapter.

2.   Data Collection Time

Datasets were collected between October 2019 and February 2020, primarily during the window of lowest tide on the days that the region was experiencing King Tide events (Sea Grant California) (NOAA Tides and Currents, 2019). By conducting data collection during these periods of time, it was possible to take photographs in the air of surfaces that were submerged for the majority of the lunar month outside of the extreme tidal events. The decision was made to collect the photograph at low tide, as opposed to

underwater, for two primary reasons, increased photo clarity and more controlled data collection for various surface types.

The first reason for conducting the majority of data collection in air during low tide events, versus taking the photographs of the surfaces while submerged, was that it allowed for higher clarity and less noise within the photographs. Generally, the dynamic nature of the intertidal zone, which is even more pronounced for locations not protected from wave energy by the Bay—as was the case for these two locations on the ocean side of the peninsula, makes for a constantly moving underwater environment with sand, debris, and grasses constantly shifting as the waves and tidal currents moved on and offshore. This movement in front of the camera lens creates a lot of noise in the photographs from one frame to another. Since these locations were also chosen for their significant biological presence at low tide, it was noted that the intertidal zone in this region was teeming with biological optical scatterers, such as plankton and algae. These optical scatterers created interference and variation between photographs, making it difficult for the photogrammetry data processing software to correlate pixels across multiple frames. The inability of the software to correlate enough common pixels between images leads to higher pixel disparity error and lower resolution of photo alignment during post-processing.

The effect of taking underwater photos in the dynamic intertidal zone can be seen in Figure 7, which shows two sets of photographs. In the Figure, photographs (b) and (d) were taken 3 seconds after photographs (a) and (c), respectively, at the same location in the intertidal zone off of Asilomar Beach. While the seafloor features are recognizable in both images, there is a significant amount interference and movement within the water column, impacting the clarity and stationarity of the photos.
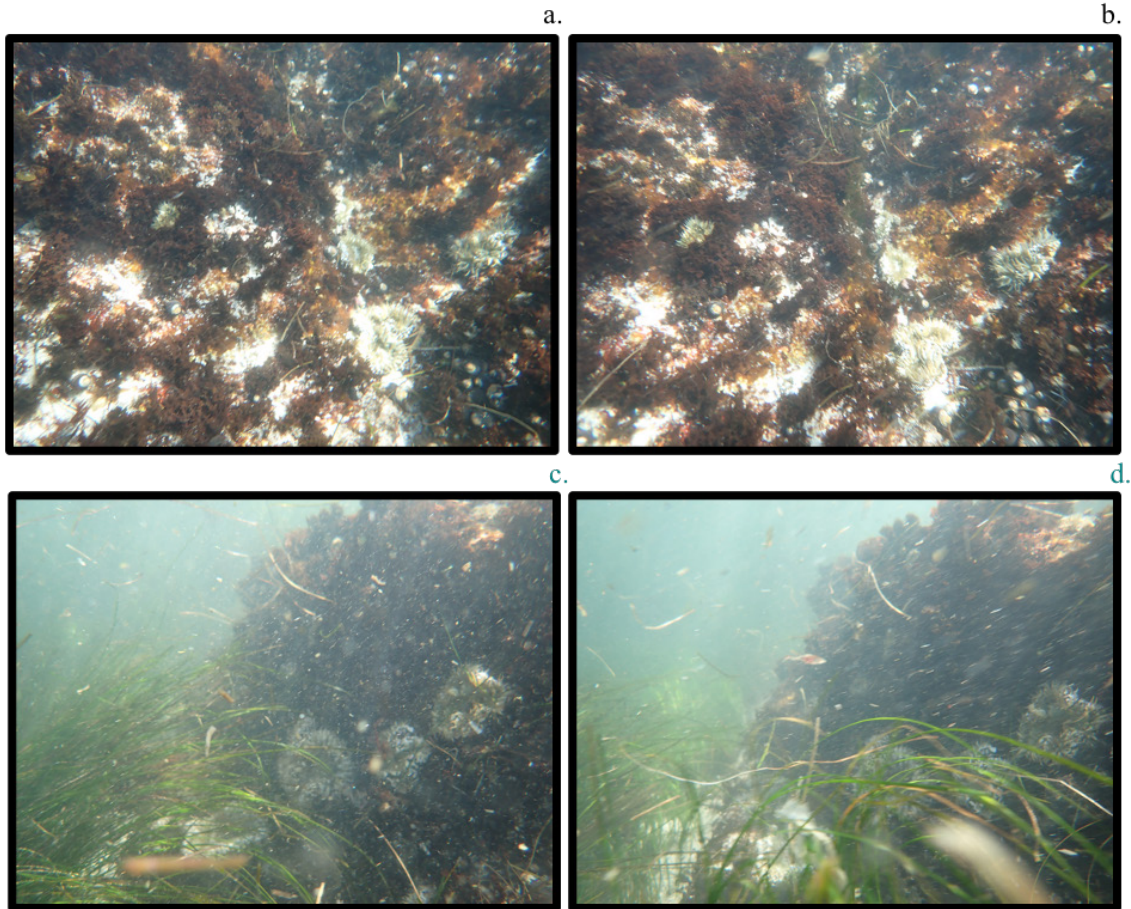
Two pairs of photos (a. and b.) and (c. and d.) were taken within 3 seconds of one another. Photos a. and c. were taken first in each set. The photographs show how the movement within the intertidal zone can create significant movement and interference between photographs, which impacts post-processing resolution.

Figure 7.   Underwater Photographs Depicting Water Clarity

The other factor in conducting data collection during extreme low tide events was that the range of surface types common to this area could be easily identified and data collection efforts could be focused on each specific surface type. If data collection was conducted underwater, the divers would have had significantly less visibility of the surfaces, making the different types harder to distinguish, and isolated data sets more difficult to collect. This would have also made post-processing of the images much more challenging. To aid in post-processing accuracy, each surface data set was annotated by a photograph taken of a whiteboard identifying the surface and location at the start of each individual set (which encompassed one specific surface type as much as possible) to ensure

that the individual surfaces could be isolated during post-processing and therefore analyzed individually when calculating roughness parameters.

3.   Data Collection Techniques

Individual data sets for the ten different surfaces identified above were collected over multiple tidal events. This meant that photographs of different surface types were acquired at both different times and different locations. Thus, ensuring a variety of data would be analyzed for each surface type. Data were split into sub-parts corresponding to surface type or morphology as a means in which to characterize the roughness characteristics of different surfaces that could be found along the rocky seafloor. This was done because it aligned with the way previous studies collected and analyzed data by different sediment types and because it allowed for the roughness measurement to be more stationary. Data were also collected and analyzed in this manner because if successful, it could create a means by which acousticians could estimate the roughness characteristics of a different area if the primary surface type for that location was known and spectral parameter data sets existed for that type of surface.

For each data set, to ensure maximum coverage and resolution for photogrammetry post-processing, between 50 and 200 photographs were taken of each surface from different angles and different viewpoints. This technique guaranteed that all parts of the target surface were captured in multiple frames with significant overlap between each frame, which is important to properly estimate the intrinsic and extrinsic camera parameters along with the 3-D surface within the Metashape software. Generally, this meant that photographs were taken along one radial from 0° to 90° before moving to the next radial, making a full circle with 180° coverage to the best degree possible. Figure 8. shows the camera positions in the processing software shown to demonstrate the amount of coverage acquired using this type of technique.
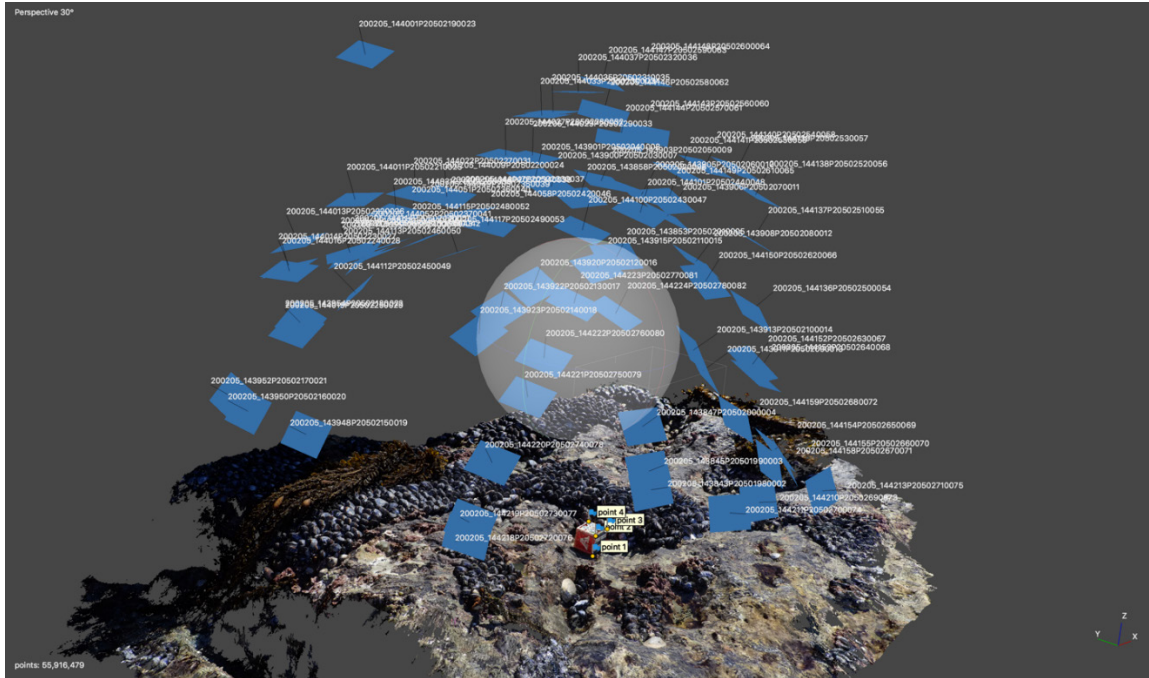
Each blue square in the figure above represents a camera location for the photographs taken over this surface.

Figure 8.   Camera Location Depiction from Metashape

Additionally, a square block with known dimensions of 44.5 mm was placed near or on each surface being photographed as a reference object as shown in Figure 9. The block remained in the same position while all photographs of the surface were collected. The photographs were taken so that the block was visible in the majority of the frames at different angles. The placement of a reference object into the collection area ensured that a local coordinate system could be created during post-processing, and the points in the digital terrain map assigned correct dimensions. The Metashape software used the block to create a reference scale to base its reconstruction of the surface. By creating a small three-dimensional reference coordinate system, each point identified in the reconstruction was assigned scaled coordinates based on its location from the reference points.
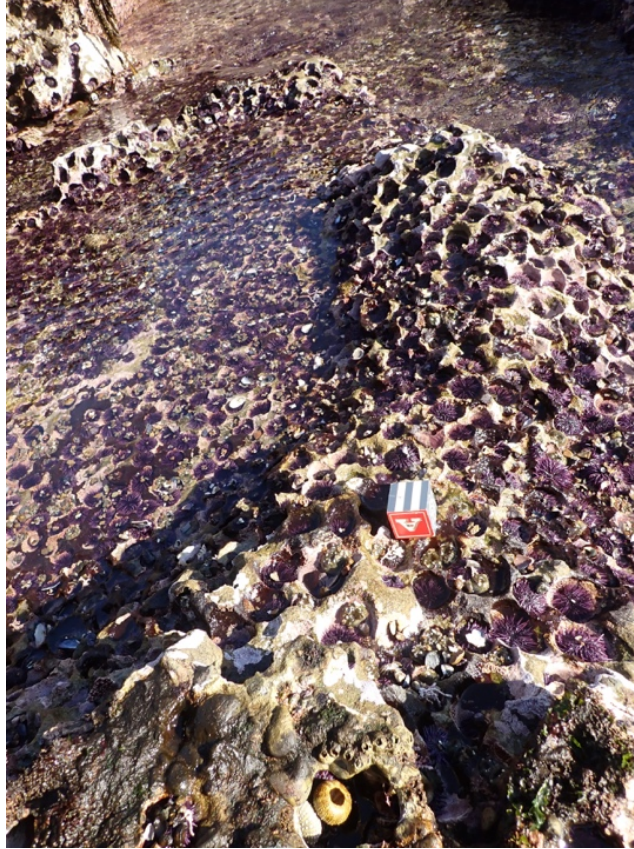
The block, as shown in the picture, was used as a reference object during the data collection process. Using a reference object allowed for a local coordinate system to be created during post-processing of the images in the commercial photogrammetry software.

Figure 9.   Reference Object Example

Data sets were collected with two different camera setups during the course of the study. First, during earlier data collection trials, two cameras were mounted on a camera frame built out of PVC pipe and standard camera handlebar mounts at a set distance apart as shown in on the left in Figure 10. The cameras were set to autofocus, which has the potential to increase the error of the height calculations within the 3-D reconstruction, especially if images are collected from significant distances from the surface (as would be the case for drones or other imagery collection systems). This potential error was minimized by taking many photographs over different angles ,but at similar and relatively small distances from the surface as well as by ensuring that the photographs from the same camera were imported and processed together in the photogrammetry software. For all data collection, the photographs were taken with a fixed International Organization for

Standardization (ISO), which is the setting for light sensitivity in digital image sensors, of 200. The cameras were both set to take ten simultaneous photos at a predetermined interval (1-2 seconds). This allowed the data collector to press the execute button on the cameras and get multiple photographs of the surface by simply moving the PVC frame slightly between each picture.

The camera frame was built out of PVC pipe, making the frame small and portable. The rectangular frame allowed for various camera distances to be used as well as a structure to stabilize the cameras or strobes as needed. The vertical handle allowed for easy carrying and camera positioning in either air or under water. All of the mounting hardware for the set-up was removable and adjustable to ensure maximum flexibility of camera distance and setup composition (1 or 2 cameras, with or without strobes). Handlebar mounts were used to attach the cameras (and housing if used) to the PVC frame. The same handlebar mounts were used for the strobe attachments but the addition of underwater ball joints, common in underwater photography tray setups, were necessary to connect the strobe lights to the frame. Fiber optic cables allowed the cameras and the strobe lights to be connected and synced, allowing the system to be used in a shallow underwater environment if the conditions were determined to be conducive for data collection.

However, even given how portable and flexible the initial setup was, a second setup was deemed necessary as the environment along the rocky shore was not easily traversed or easily accessible with even a lightweight, portable camera setup. For the second setup, a single camera was detached from the frame and that camera, along with the reference object, was used by the data collector. Photographs were then taken manually as shown on the right in Figure 10. The settings of autofocus and ISO of 200 remained the same but the data collector had to actively take each frame using the same collection methods and considerations as described for the dual camera setup. While this secondary process was slower, it allowed for more surface coverage and collection precision during the imagery collection process in the rugged, slippery environment found along the rocky shoreline at low tide. While both methods worked, this second setup with one camera and a reference object was the primary means of collection for the data sets analyzed within this paper.
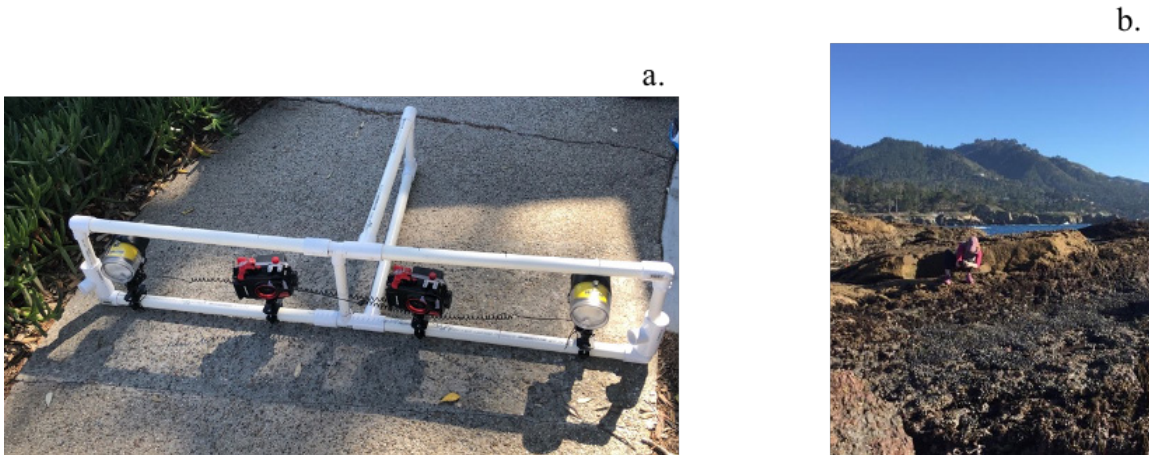
Picture (a) shows the dual mounted camera setup on the portable PVC frame. Picture (b) shows the author using a single hand-held camera and reference block to collect photographs in a hard to reach area of Point Lobos.

Figure 10.   Camera Setups

It should be noted that this secondary setup was only feasible because of the commercial photogrammetry software that was being used to process the data. If traditional stereo photogrammetry techniques, as described earlier, for processing were used, only the first setup would have been valid and processing techniques would have had to include camera calibration. This is the case because unlike previous experiments using traditional stereo photogrammetry processing techniques, a checkerboard pattern was not required to calibrate the photographs for the primary data collection when the commercial photogrammetry software was used. This step was not necessary when processing the image sets from individual cameras because the software is designed to perform the calibration during processing, provided there are enough common points between photographs and a well-placed reference object (Agisoft Metashape User Manual, 2020).

D.   DATA PROCESSING

The data processing portion of this experiment relied heavily on the use of Metashape Photogrammetry Software (Agisoft LLC, 2020) to produce the Digital Elevation Maps (DEMs) from which the height fields for the individual surfaces were derived. Metashape utilizes 'Structure from Motion' (SFM) and scale invariant feature transform (SIFT) algorithms to that identify features between overlapping images and

extract the camera parameters from the images to resolve the 3-D coordinate system and reconstruct the surface (Karmacharya et al. 2019). When the images are brought into the program and aligned, the software identifies tie points between overlapping images. These tie points are common objects in real space that can be identified in two or more images. The number of tie points identified is based on the resolution settings within the programs and the resolution and number of images being used (Agisoft LLC 2020). However, in an almost reverse process from traditional means, the software can use the relative information from the tie points to calculate the internal and external parameters of the cameras within the calibration groups, which are then used to undistort the images. From there, the software can process the tie points and all the pixels in the corrected images using the calculated parameters of focal length, camera baselines, and pixel disparities to create what is known as the dense cloud, or the 3-D map of the images (Agisoft LLC 2020). Figure 4 showed a very simple example of these calculations for traditional techniques. However, the software is able to do this at significantly higher resolution, comparing millions of pixels throughout the photo set in order to produce extremely high resolution 3-D depictions and coordinate grids of the surfaces photographed. The steps of this process will now be explained in more detail below.

1.   Photograph Import and Data Management

Once photographs were taken at each location, they were downloaded and converted from RAW to TIF files using the Olympus Workspace photo processing software recommended through the camera manual and put into folders by camera (if two were used), location and date. Within each folder, subfolders for each set of photos for the individual surface sets were created. Collecting, organizing, and processing the datasets as individual surfaces and surface types was important to the process since it allowed for decreased error in the alignment process (Agisoft LLC, 2020) and allowed each surface type to be processed individually, allowing for roughness parameters to be estimated specifically for each type of surface that was identified within this study.

2.   Metashape Processing

The first step in data processing involved the use of the Metashape Professional software (Agisoft LLC). The standard workflow utilized was as follows:

1.   Create a new Chunk (a set of photos within a project) and Import photos from one surface

2.   Align Photos

3.   Delete photos (cameras as referred to by the software) that failed to align

4.   Delete extraneous/mislocated points (ones significantly outside the model/region box)

5.   Assign markers to each corner of the reference object (block) and assign coordinates based   on measurements of the side lengths.

6.   Verify the marker locations in all photographs (cameras) and covert the coordinate system

7.   Build Dense Cloud

8.   Build Mesh

9.   Create Digital Elevation Map and Export

10.   Create Orthomosaic and Export

The workflow outlined above was the standard procedure for all data collected. Depending on the number of photographs taken of each surface, the entire workflow could take as much one to two days since various points of the workflow required significant processing time due to the resolutions selected. More detail on each step of the workflow is outlined in the following paragraphs (Agisoft LLC, 2020).

For each surface, a new Chunk, or set of photos within a project, was created and photos were imported into the Metashape software. The project was then saved by location,

date, and surface type so processing or data could be accessed at a later time if necessary (Agisoft LLC, 2020).

Once photos were imported and saved, they were aligned using the highest accuracy settings. Metashape Professional software is designed to align the photos using aerial triangulation and bundle block adjustment (Agisoft LLC, 2020). By identifying common features in multiple photographs, the software could create ties, or common pixels, across images, creating a sparse point cloud, as shown in Figure 11. The sparse point cloud is a 3-D representation of the tie-points that are found between the images, therefore maximizing the number of photographs, while ensuring significant overlap between photos during data collection, of a given surface will allow the software to find and calculate more tie points (matching pixels) between images. This will result in a higher resolution initial point cloud (Agisoft LLC, 2020).
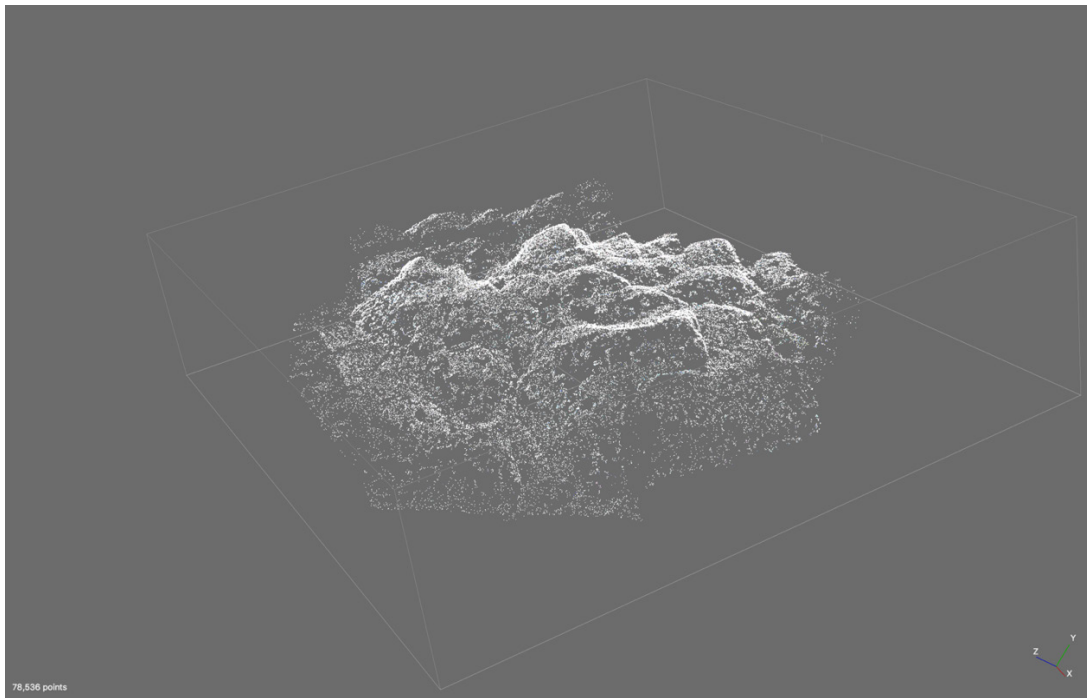
Sparse cloud of tie points created during the initial alignment phase of processing in Metashape Professional. Derived from (Agisoft LLC 2020)

Figure 11.   Sparse Cloud Example Created by Metashape

When the photos are imported, Metashape automatically divides the photos into calibration groups based on resolution and image data. During this alignment process, the software estimates the internal and external camera orientation parameters for each calibration group (groups can consist of one or more images). External parameters include the camera position and orientation (rotation) while internal parameters include the focal length and radial distortion (Agisoft LLC 2020). The accuracy of the alignment is dependent upon the amount overlap of the images (cameras—as denoted by Metashape), creating as many high confidence tie points as possible, as well as the amount of the surface that is visible within the images, since some angle of the camera may create blind spots where parts of the surface are not visible and therefore cannot be correlated. Accuracy of the alignment can be improved through the editing process of the sparse cloud which is why the next step in the workflow allowed for the deletion of any erroneous or mis-located tie points after camera alignment. Further optimization occurred when the reference object coordinates were set within the workflow (Agisoft LLC, 2020).

Once the photos were imported, aligned and edited, reference markers were placed on each corner of the reference block as seen in Figure 12. For this experiment, the manual approach to placing markers was used in order to reduce error. Since it was done manually, this step could also be conducted prior to alignment of the photographs if desired. The manual placement process started with the first photo that the reference block was visible. In that first photograph a marker was added to one of the bottom corners of the block and that marker was given the local coordinate of (x=0, y=0, z=0) within the reference tab of the software. From there, markers were added to the other visible corners of the reference block and the appropriate local coordinate were given based on the measured length of each side. It was imperative to ensure that all three directions (x, y, and z) were referenced for each project in order to create a local coordinate system at the sub-millimeter scale.

Once markers were created and assigned coordinates in the first photograph, the same markers were manually placed in the second photograph of the set. Metashape could then automatically place the markers in the subsequent photographs in the Chunk, but for accuracy purposes during this experiment, each remaining photograph was examined and markers were verified or moved as necessary to match the marker location in the first and

second photographs. While this was a more time-consuming process, by verifying the marker positions on the block in each photograph, the coordinate system error can be significantly reduced which will lead to a more accurate digital elevation map and exported xyz files later in the workflow. Once all the marker locations were verified in each photo, the coordinate system was converted using only these marker coordinates. This conversion established the local coordinate system that the 3-D model would be built upon in the following steps (Agisoft LLC, 2020).

Following the alignment and creation of a local coordinate system, the dense cloud was built. For this experiment the 'ultra high-quality' setting was used to create the dense cloud for each surface, meaning that the original image size was used while making the dense cloud with no image downsizing. Additionally, depth filtering settings were kept at the 'mild' level to ensure that the smallest resolved features would not be removed as noise. This portion of the process took anywhere from a few to 48 hours because of the quality and filtering parameters selected. The number of cameras and tie points selected within each project determined the length of processing time. To create the dense cloud, the Metashape software processed the image data into spatial information using the camera positions (each photograph) to generate depth information, in a similar manner to the techniques described in Section 2.B. and depicted in Figure 4. Using these height calculations, the software creates a 3-D model of the images as shown in Figure 12. (Agisoft LLC, 2020).
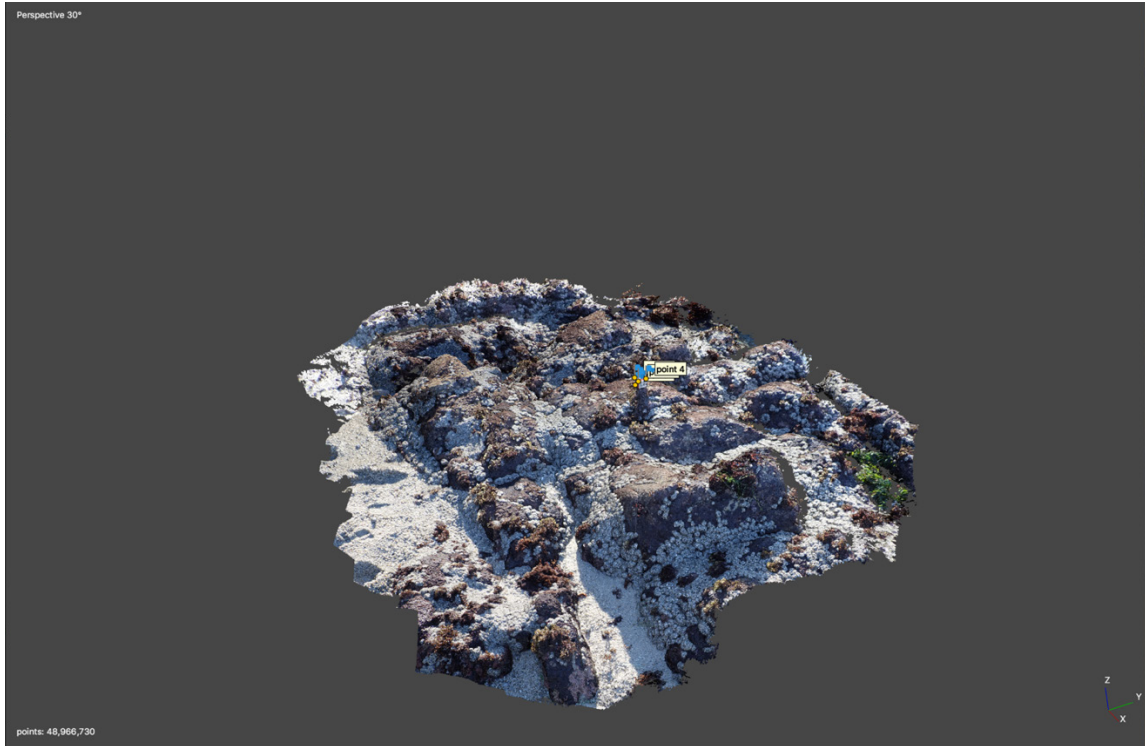
Depiction of a dense cloud created by Metashape. Derived from (Agisoft LLC, 2020)

Figure 12.   Dense Cloud Example Created by Metashape

From the dense cloud, Metashape can construct a polygon mesh model. To construct the mesh, the dense cloud was selected as the source data and the height field was selected as the surface type. As with the dense cloud, the 'ultra high-quality' was selected which meant that this step could also take a significant amount of processing time. The face count specification was set to high so that the software would create the highest possible resolution mesh based on the total number of points in the dense cloud. Additionally, the interpolation feature was disabled so that the mesh was only constructed in areas of the model that had dense cloud parameters. These settings ensure the highest level of resolution was maintained during the mesh processing (Agisoft LLC, 2020).

With the dense cloud and the mesh created, data was exported from Metashape in order to estimate the power spectral density in MATLAB. For all the surfaces processed in Metashape, a digital elevation map (DEM), orthomosaic image, and text file containing the individual xyz points (point cloud) were created. An example of a DEM and orthomosaic

39

image for each surface can be found in the table in Appendix A. The DEM and the orthomosaic image created for each surface type were valuable for visual comparison, providing an understanding of what each surface feature looked like in a 3-D space, while the point cloud text file provided the height data that would be used to estimate the height power spectral density (Agisoft LLC, 2020).

3.   Roughness Power Spectral Density Calculations

Once the point cloud file for each surface was exported from the Metashape software, it could then be further processed in MATLAB, to estimate the roughness power spectrum. In order to characterize roughness parameters of these surfaces, multiple techniques to calculate the power spectral density were utilized.

Due to processing limitations of the computer systems and MATLAB, as well as the large size of the xyz files exported by Metashape, each surface was broken out into 0.1 m by 0.1 m sections to be processed at a spatial resolution of 0.01 mm. By using these dimensions, features on spatial scales of 0.05 m and smaller could theoretically be resolved. These spatial scales correspond to the size of the wavelengths of signals that fall within the high-frequency range defined in Chapter I. These dimensions were chosen in order understand how scattering strength predictions will be impacted by surface roughness at very small spatial scales when utilizing high frequency acoustic signals (Jackson and Richardson 2007).

To make the appropriate spectral density calculations, a rectangular grid in the x-y plane was first created from the xyz data file. The mesh was constructed at the set spatial resolution of 0.01 mm for all surfaces so that each (x,y) point was associated with a specific z value (or elevation). From there, 1-D spectra were calculated. To do this, a cross-section (or slice) of the height data was taken in both the x and y direction based on the local coordinate system created within Metashape.

The 1-D roughness spectrum, $W_1\left(\overline{K_x}\right)$ is defined as the Fourier transform of the height covariance, $B(x,0)$, as depicted in the equation,

$$W_1\left(\overline{K_x}\right) = \frac{1}{2\pi} \int B(x,0) e^{-iK_x x} dx$$

(1)

where $B(x,0) = \iint W\left(K_x, K_y\right) e^{iK_x x} dK_x dK_y$ is the covariance in terms of the spectrum (Jackson and Richardson 2007, p. 375).

If necessary, the 1-D spectrum can be converted, using the assumption of isotropy from the 2-D spectrum using the equation (Jackson and Richardson 2007, p. 375),

$$W_1\left(K_x\right) = \int W\left(K_x, K_y\right) dK_y$$

(2)

Likewise, the 2-D roughness spectrum, $W\left(\overline{K}\right)$, is defined as the Fourier transform of the height covariance, $B\left(\overline{R}\right)$, where $\overline{R} = (x,y)$ and $\overline{K} = \left(K_x, K_y\right)$, as depicted in the equation (Jackson and Richardson 2007, p. 174),

$$W\left(\overline{K}\right) = \frac{1}{2\pi} \int B\left(\overline{R}\right) e^{-i\overline{K}\cdot\overline{R}} d^2 R$$

(3)

The Fourier transform is normalized by the root mean square of the window so that the spectral levels do not need to be corrected for the windows used. The root mean square (RMS) height is shown in the following equations (Jackson and Richardson 2007, p. 174),

$$h^2 = \int W\left(\overline{K}\right) d^2 K$$
$$K = \sqrt{K_x^2 + K_y^2}, \text{ the wavenumber}$$

(4)

The Fourier transforms were then averaged using,

$$S\left(u_x, u_y\right) = \frac{\langle\, | F\left(u_x, u_y\right) | \,\rangle}{\left(L_x L_y\right)}$$

(5)

41

where $F\left(u_x, u_y\right)$ is the Fourier transform, the $\langle\,\rangle$ brackets represents ensemble averaging, and L_x and L_y are the linear dimensions in the x and y direction of the measurement area (Olson, D.R, 2014).

For spectral comparison purposes, two methods for spectrum calculations were used for the 1-D analysis, the Welch method and the multitaper method. For the Welch method, a single Hann window and a sampling interval of 10,000 m-1 (or 1/ 0.01 mm) were used. The Welch method produced a one-sided, normalized power spectral density estimate (Welch P., 1967).

As a comparison, multitapers reduce spectral leakage, since they have the least spectral leakage for a given sequence length, N. They also provide a way to average the data by using the entire sequence through orthogonal windows instead of breaking the sequence up into sections, as is done in the Welch method. The multitaper calculation utilizes discrete prolate-spheroidal sequences (DPSS) as window functions, which is what reduces the spectral leakage (Thomson, 1982). The multitaper spectrum calculations for this study were done with the same sampling frequency as the Welch estimates and NW=4, which is defined as the time-bandwidth product. This value determines the number of tapers used based on the calculation of (2*NW-1) with last taper being dropped. Also, the NW parameter determines the effective bin width of the power spectral density. The multitaper method also produces a normalized one-sided power spectral density estimate (Thomson, 1982), (Mathworks Inc).

In addition to the 1-D spectrum estimates, 2-D calculations were also completed as a means of comparison since both 1-D and 2-D spectrum estimates have been calculated during previous studies. Using the same point cloud file for each section, as was used for the 1-D estimates, the 2-D Fourier Transform function shown in the equation,

$$F\left(u_x, u_y\right) = \frac{1}{\left(2\pi\right)^2} \int_{-\frac{L}{2}}^{\frac{L}{2}} \int_{-\frac{L}{2}}^{\frac{L}{2}} f(x,y) e^{-i2\pi x u_x - i2\pi y u_y} \, dx \, dy$$

(6)

was applied to the data (Olson, D.R, 2014).

Finally, a circular shift function was applied to the data in order to calculate the periodogram as in Figure 14. This spectrum calculation was conducted using a rectangular window and the same spatial resolution of 0.01 mm that was used for the 1-D spectrum calculations (Mathworks Inc).

Once the spectrum calculations were completed and spectrum variables were saved into a master data table, plots of each spectrum could be generated. Each power spectrum estimate in the x and y directions were plotted on log-log plots. In addition to the Welch and multitaper spectrum estimates, the 1-D components in the x and y directions for the 2-D spectrum data sets were plotted in the same manner.

4.   Spectral Parameter Calculations

When the power spectrum estimates discussed in the previous section were plotted in log-log space, it was evident that there were consistently two distinct slopes (regressions) present within the majority of the spectrums. An example of the plotted spectra which can be seen in Figure 13.
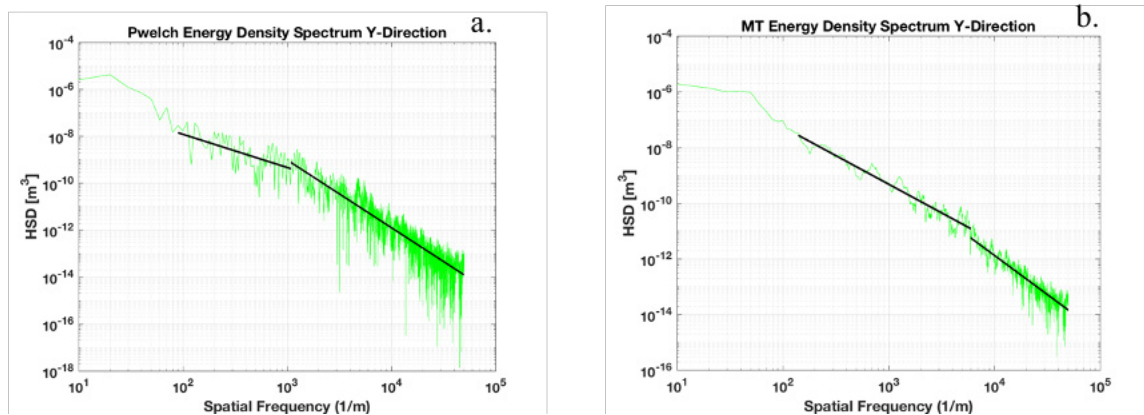
The graphic (a) shows a 1-D Welch method spectrum calculation over a kelp surface with two power-law lines on the spectrum. The graphic (b) shows the 1-D multitaper spectrum calculation for the same kelp surface with two power-law lines on the spectrum.

Figure 13.   1-D Roughness Power Spectrum Plots and Power Law Fit Lines

43

Thus, with the intent of capturing the behavior of the roughness spectra, two separate lines were fit to each of the power spectrums. Since the fit was linear in log-log space, the spectral parameters of ϕ_1 and γ_1 to be obtained from the equations of the line that was fit to each distinct spatial frequency band. Examples of the plotted lines are plotted over the spectrums in Figure 13.

From the plotted lines for each spatial frequency band, the acoustically relevant parameters of ϕ_1, the spectral strength or the y-intercept in log-log space of the best fit line of each frequency band, and γ_1, the spectral slope or the slope of the spectrum for each frequency band in log-log space, could be determined (Jackson and Richardson 2007). It should be noted that owing to the direction of the slope (decreasing from left to right), the spectral slope value identified was always negative. Therefore, the spectral data values derived from the modeled lines actually reflects the $-\gamma_1$ value.

These spectral parameters were determined through calculation of the 1-D power density spectrum $\left(\Phi_1(F) \right)$, which was done in the previous processing step, and the fit of the power law in the equation,

$$\Phi_1(F) = \frac{\phi_1}{F^{\gamma_1}}$$

(7)

These spectra utilized spatial frequency (F) but could be converted to a 1-D spectra based on wave number $\left(w_1(K) \right)$ if necessary, as shown in the equation,

$$\Phi_1(F) = 2\pi w_1 \left(2\pi F \right)$$

(8)

due to the spatial frequency relation to wave number, which is shown in the equation (Jackson and Richardson 2007),

$$K = 2\pi F = \frac{2\pi}{\lambda}$$

(9)

From the 1-D parameters, equivalent 2-D parameters (w_2 and γ_2) can be calculated for use in acoustics scattering estimates using the following equations (Jackson and Richardson 2007, p. 478):

$$\gamma_2 = \gamma_1 + 1$$

(10)

$$w_2 = w_1 \frac{\Gamma\left(\frac{\gamma_2}{2}\right)}{\sqrt{\pi}\Gamma\left(\frac{\gamma_2 - 1}{2}\right)}$$

(11)

$$w_1 = \phi_1 \left((2\pi)^{\gamma_2 - 1} \right)$$

(12)

Active input was required during the processing of each spectrum to select the start and end frequencies for each frequency band to ensure the most accurate model representation for the individual sections identified within each spectrum. To do this, three separate frequencies were chosen and manually input, upon prompting within the code, to delineate the two separate sections in which the power law lines would be fit. This plotting and line fitting process was completed for all spectra calculated on each 0.1 m by 0.1 m section across all the surfaces. Upon completion of each section, the spectrum parameters (ϕ_1 and γ_1) were saved to the master data table for follow on analysis. The spectral parameters for all the spectra analyzed can be found within the tables of Appendix B.

For the 2-D spectrum calculations, 2-D polar roughness spectrums were also generated using a contour plot on the periodogram for all frequencies as seen in Figure 14. In addition to the 2-D polar colored contoured plot of the roughness spectrum, each 2-D output was averaged radially. This allows for a better graphically representation of the 2-D data which will be shown in the results section of this paper.

45
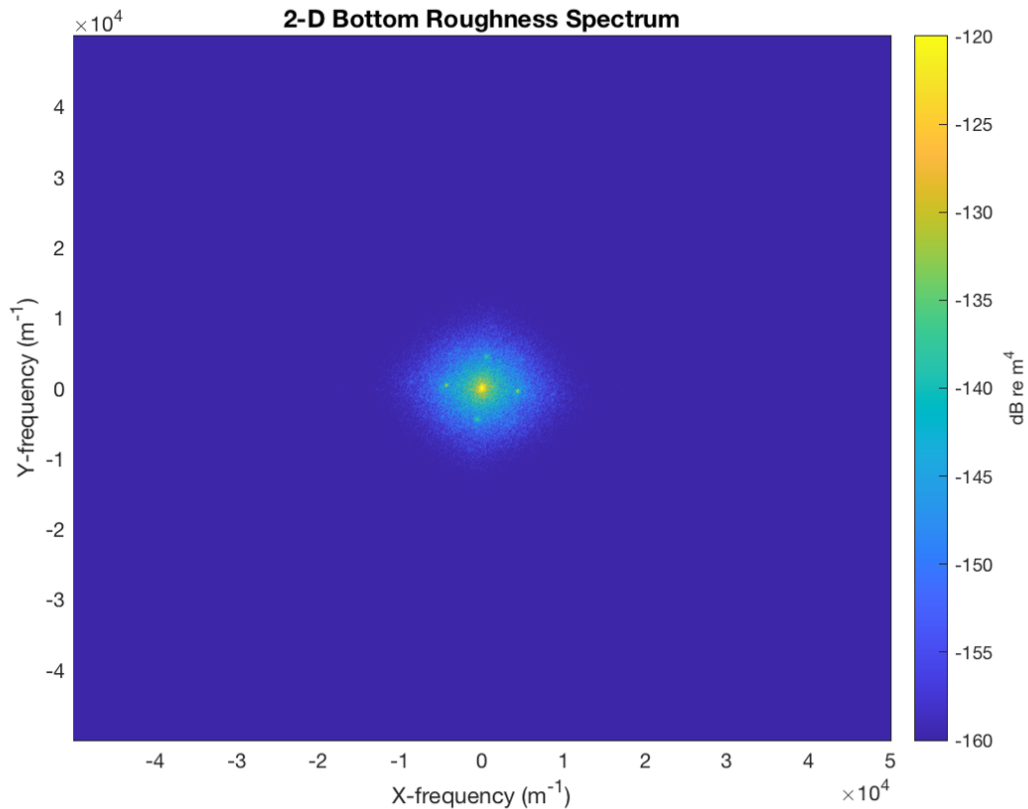
2-D roughness spectrum for the same kelp surface as Figure 13.

Figure 14.   2-D Polar Roughness Power Spectrum

5.   Acoustic Scattering Strength Calculations

Using the spectral parameters and seafloor material properties, it is possible to predict the bottom scattering strength of a given surface using acoustic scattering models. For this study, the perturbation approximation was utilized. Perturbation theory is commonly utilized for acoustic scattering calculations for its ability to link wave propagation in the seafloor and the roughness spectrum to scattering strength (Jackson and Richardson 2007), (Jones and Jackson, 2001). The roughness properties inputs for the model were estimated from the data analyzed in this experiment and the geoacoustic inputs were taken from Gruber (2019). The selected values for the set variables are shown in Table 1.

46

Table 1.   Acoustic Scattering Strength Model Variables

Parameter	Value
Frequency	200 kHz
Sound Speed of Water	1490 m/s
Compressional Sounds Speed	6255 m/s
Shear Speed	3464 m/s
Water Density	1024 kg/m^3
Bottom Density	2644 kg/m^3
Bottom Attenuation Parameter in Rock	0.02
Shear Wave Attenuation Parameter in Rock	0.04

The frequency of 200 kHz was chosen because it was the frequency used in Gruber (2019) to collect scattering data on the rocky outcroppings in the Monterey Bay near where this data was collected. Using this frequency would allow for comparison between collected scattering strength values and scattering strength values derived from roughness measurements in this paper. For these calculations, an elastic geoacoustic model was selected (Gragg et al. 2001), (Jackson and Richardson 2007), since granite supports shear waves. A detailed description of the perturbation approximation techniques for an elastic model can be found in Chapter 13. of (Jackson and Richardson 2007).

To run the scattering model estimates, the 1-D parameters, ϕ_1(spectral intercept) and $\gamma_1$discussed in the previous Section first had be converted to their 2-D equivalent values ($w_2$and γ_2) using Eq. 10 and 11 that were described above. Scattering strength calculations using all the derived spectral parameters were then made for three different incident/grazing angles (which were set to the same value). Since acoustic systems utilize a range of angles, 10°, 45°, and 60° were chosen for these model runs in order to cover the range of grazing angles measured in Gruber (2019).

THIS PAGE INTENTIONALLY LEFT BLANK

III. RESULTS AND DISCUSSION

Image processing using the commercial photogrammetry software resulted in detailed DEM and orthomosaic images for each surface that was analyzed. Examples of a DEM and corresponding orthomosaic can be found in Figure 15. A DEM and orthomosaic example for each surface can also be found in Appendix A. Height fields were produced and exported as text files that could be analyzed through spectral analysis.
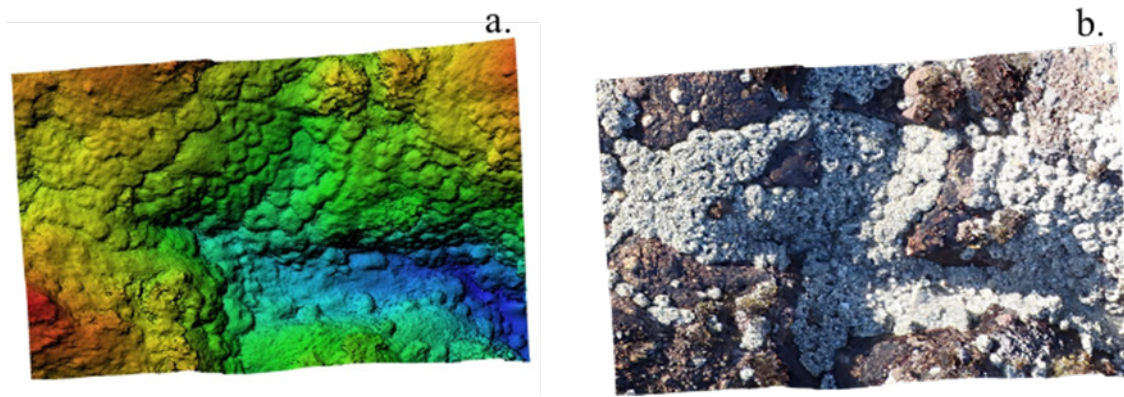
Picture (a) shows a DEM of a surface cover in anemones. Picture (b) shows the corresponding orthomosaic image of the same anemone surface. Both images were created in Agisoft Metashape.

Figure 15.   DEM and Orthomosaic Image Examples

Spectral parameters were estimated from a subset of the extracted height field data through the implementation of a power-law model to the roughness power density spectra. The methods used for these calculations were discussed in Chapter II and the results of all the estimates can be found in the tables of Appendix B. The 1-D ϕ_1 and $-\gamma_1$ parameters for each spectrum can be found in the first three tables while the fractal dimension calculations can be found in the fourth table of Appendix B.

During the data processing portion of this analysis, three different types of spectra, multitaper method, Welch method, and 2-D Fourier transform, were used to estimate the roughness power density spectra. The multitaper method generally best estimated the

roughness spectra while reducing noise at the higher spatial frequencies as compared to the other methods. Therefore, only the multitaper method spectral parameter results will be shown in this chapter for the 1-D parameters and scattering strength calculations. The rest of the spectral parameter plots can be found in Appendix C for comparison purposes.

It should be noted that the results for roughness parameters and scattering strength of the surfaces covered in grass, kelp, and algae are most likely not appropriate once the surfaces are submerged in the water column since they become mobile, acting more as volume scatters as discussed in Chapter II. However, these surfaces were not removed from the plots within this chapter since they are widely present along the rocky shoreline both above and below the water line, and they provide a good comparison for potential surface scale and shape variability when considering the range of surfaces and associated spectral parameter values that are present within a rocky seafloor environment.

This chapter will summarize the spectral parameter results and examine trends in the data. It will also provide any relevant discussion and dataset comparisons for the collection methods/techniques, the range of the frequency bands identified in the spectra, the estimated ϕ_1 and γ_1 parameters and associated calculations across both of the frequency bands, the 2-D radially averaged spectra, and finally the acoustics scattering strength estimates based on the spectral parameters.

A.   DATA COLLECTION METHODS AND EQUIPMENT

Both the camera setups and the data collection techniques used for this experiment were effective in collecting photographs for this type of study. However, maximum flexibility was found using a single camera to take many images of one surface since it allowed for the most accessibility to the surfaces along the shoreline. It was also supported in post processing by the photogrammetry software utilized given that the software was designed to process each individual image as a separate 'camera', the term that Metashape assigned to each image. This method was effective because Metashape uses tie points estimated with structure from motion and scale invariant feature transform (SIFT) algorithm to simultaneously estimate the extrinsic and intrinsic parameters of the cameras, which is only possible if there is a significant dataset and overlap between images like the

datasets collected for this study. These data collection techniques and capabilities within the software allowed for significant photo collection flexibility on stationary surfaces.

It is important to note that this type of data collection was only feasible because the images were collected in air, on stationary surfaces, where many images could be collected of a surface over a short period of time with no appreciable change to the surface in between frames. Data collection in a more dynamic environment would have required a more traditional approach to with dual, time-synced cameras to capture simultaneous images that could be processed together as pairs before the surface underwent any changes.

3-D surfaces with spatial resolutions, on the order of millimeter to submillimeter scales, were produced using the equipment and the commercial stereophotogrammetry software outlined in Chapter II. Resolution at this scale was attained from the combination of using the high-resolution digital cameras, the collection of a larger number of photographs over each surface, and by applying the highest resolution thresholds available within the software during post processing. The final resolution is impacted by combination of all of these factors, meaning a reduction in resolution those inputs will have a negative impact on the final resolution results.

The ability to use a single camera to conduct this type of data collection while maintaining a high spatial resolution output means that imagery collection for the purpose of estimating roughness parameters may be expanded to other techniques. These techniques could include imagery collected from drones or even satellites, as long as an object with known dimensions is present within the images collected and careful consideration of camera settings and calibration or processing settings is taken into account due with the higher elevation imagery collection. This type of data collection is something that is already being used within other fields of study in the coastal environment, and with the implementation of some automation, this type of method could allow the acoustics community to collect and analyze roughness estimates relatively quickly, over large areas of the coastline which would ultimately improve the roughness parameter data sets used for acoustic scattering strength estimates on the rocky seafloor.

51

B. SPATIAL FREQUENCY BANDS

As discussed in Chapter II, three distinct spatial frequencies were chosen on the spectra to distinguish the two discrete slopes that were created by a consistently identified break in the slope of the regression portion of each power spectrum. Data from Briggs et al. (2002) which was plotted and analyzed in Jackson and Richardson (2007) also showed a break in the slope of the roughness power spectra for at least one collection site. It was unclear in the analysis of the data whether this break was natural, or a product of the data processing techniques applied to the data (Jackson and Richardson 2007, p. 182). Since all the data in this study was processed using consistent methods from start to finish, it is possible that the distinction in slopes is a product of processing as well. As with most processing techniques, artefacts such as spectral leakage and aliasing may play a role in producing a break in the slope, as could the image processing techniques. These impacts should have been minimized given the windows selected and the high resolution of the data and processing settings. Additionally, the break in slope was evident in all three spectral estimate methods that were utilized and the wavenumber on which the break fell varied by surface type. Therefore, the break in slope could be naturally occurring, delineating the primary and secondary spatial scales that make up the composition of the surface features at the range of spatial scales being analyzed (mm to submillimeter in this case).

Within this study, the first spatial frequency identified marked the start of the regression, the second spatial frequency marked the delineation or break between the two different slopes, and the third frequency marked the end of the regression on the spectrum. Figure 15 shows the box plots illustrating the range of spatial frequencies chosen for each delineation, specifically for the multitaper spectra, broken out by surface type. On that figure, the spatial frequency delineations identified within the x-cross sections are shown in plots (a), (b), and (c), while the y-cross section delineations are displayed in plots (d), (e), and (f).

For the purposes of this paper, the spatial frequency bands are referred to as either section 1 and section 2 or the 1st Frequency band and the 2nd Frequency band. Section 1 is the spatial frequency band between the first spatial frequency delineation on the plots (a) and (d) and the spatial frequency delineation illustrated on the plots (b) and (e) in Figure

15. Section 2 is therefore the spatial frequency band between the spatial frequency values shown on plots (b) and (e)and the spatial frequencies plotted on the plots (c) and (f), which also correspond directly with the limit of the spatial resolution set within the calculation parameters in Figure 16.

Across all surfaces and spectrum types, the average value for the break in slope across all spectrums was 2302.6 m^{-1}, with the average spatial frequency range for section 1 identified as 112.2 to 2302.6 m^{-1}, and the average spatial frequency range for section 2 calculated to be 2302.6 to 49990 m^{-1}. These spatial frequencies correspond to spatial resolution ranges of 8.9 to 0.4 mm for section 1 and 0.4 to 0.02 mm for section 2. Therefore, the overall range of spatial scales considered for roughness parameters estimated in this paper falls between 0.02 mm and 8.9 mm.

The box plots of the spatial frequency delineation ranges in Figure 15 show that while there is some variation around the mean spatial frequencies limits for each section listed above, they are relatively consistent for the first (plots (a) and (d)) and last frequencies (plots (c) and (f)) of each surface. The largest variations around the mean are seen for the middle frequency (the break in slope), delineating where section 1 ends and section 2 begins (plots (b) and (e)). This variation in the center frequency delineator could be due to multiple factors including the spectrum type or the surface type being analyzed.

The existence of a break in the slope and the wavenumber at where that break falls on the spectra both could be an artefact of the surface composition. For example, the granodiorite found in this area of Monterey Bay is composed of both large crystals and a finer crystalline structure (Green, 1977). This type of scale and spatial variation in the composition of the surfaces could account for two distinct slopes, if the roughness parameters at each scale vary significantly. Since all the surfaces analyzed in this paper are composed of features of varying scale (within the spatial frequency bands analyzed), it is possible that the change in slope and the wavenumber on which that change occurs is a factor of the composition of the surfaces in this environment.
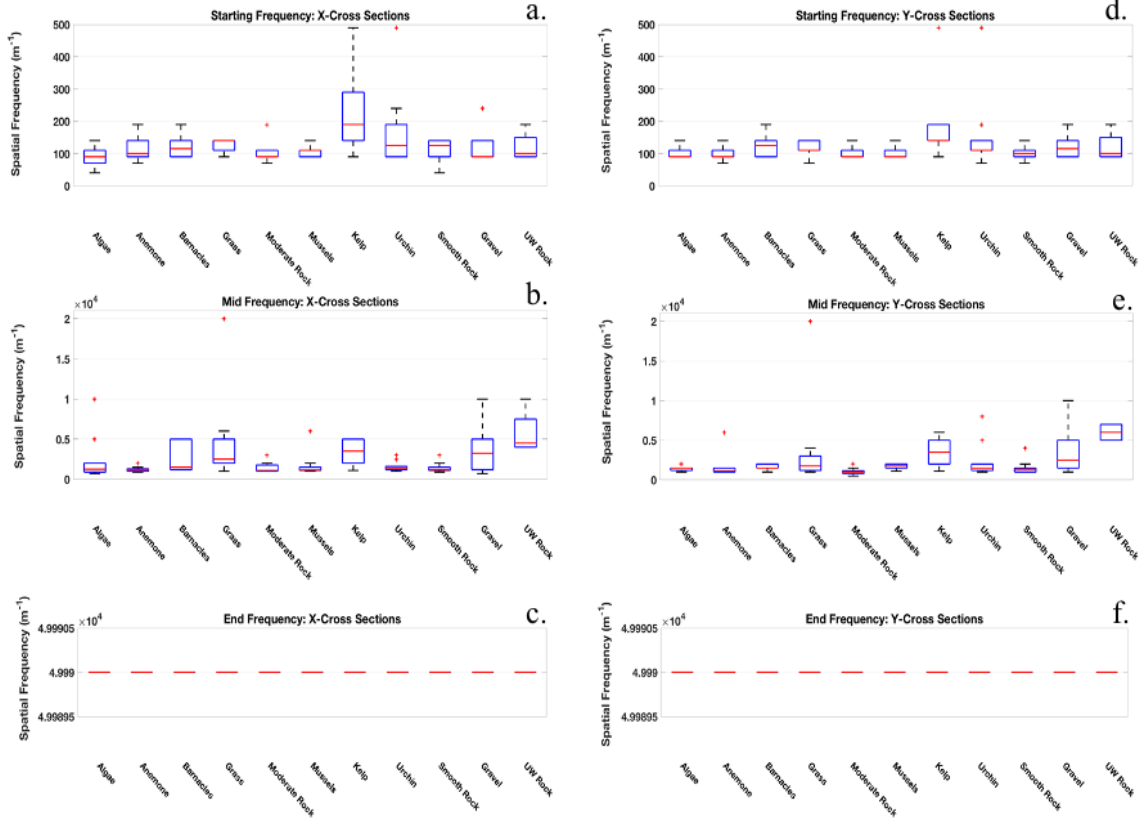
This figure shows box plots of the multitaper spectrum frequency delineators by surface type. The surface types are indicated on the y-axis. The top two plots (a) and (d) show the starting spatial frequencies of the power spectra regressions. The center plots (b) and (e) show the values of the break in slope identified in the spectra. The bottom two plots (c) and (f) show the spatial frequency marking the end of the spectra regressions. The median spatial frequency for each surface is depicted by the red line in each box. The blue box represents 50% of the data, or the limits of the 25th percentile and the 75th percentile. The dashed black lines represent the upper and lower adjacent values and the red plus signs represent outliers within the data for each surface. Plots (a), (b), and (c) show the frequency delineators for the x-cross sections and plots (d), (e), and (f) show the frequency delineators for the y-cross sections.

Figure 16.   Frequency Ranges Delineations for the Multitaper Spectrum
Estimates - by Surface Type

C.   1-D POWER-LAW PARAMETERS

The 1-D ϕ_1 and γ_1 parameters were derived from the power-law fit lines (in log-log space) for both sections of the slope on the power spectra. Box plots for the ϕ_1 (spectral intercept) parameters derived from the multitaper spectra can be found in Figure 16, while

54

box plots for the $-\gamma_1$ (spectral slope) parameters from the multitaper spectra can be found in Figure 17, both of which are delineated by surface type. Since γ_1 represents the magnitude of the slope, the direction of the slope for all the spectra (decreasing from left to right) meant that all the spectral slope values were estimated as $-\gamma_1$, which is also what is plotted in the figures below.
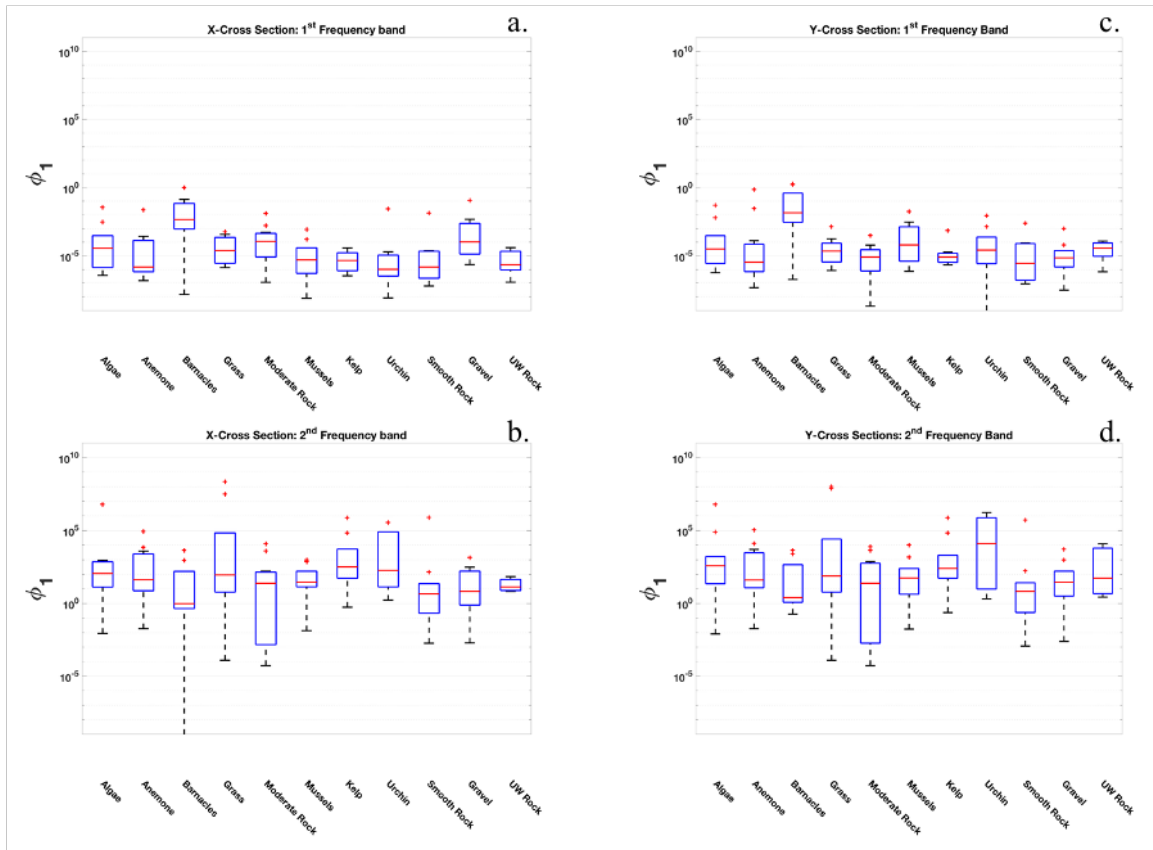
Box plots of ϕ_1(1-D spectral intercept) parameters for the multitaper spectrum based on surface type. The median value for each surface is depicted by the red line in each box. The blue box represents 50% of the data, or the limits of the 25th percentile and the 75th percentile. The dashed black lines represent the upper and lower adjacent values and the red plus signs represent outliers within the data for each surface.

Figure 17. ϕ_1 Boxplots Based on Multitaper Spectrum Estimates
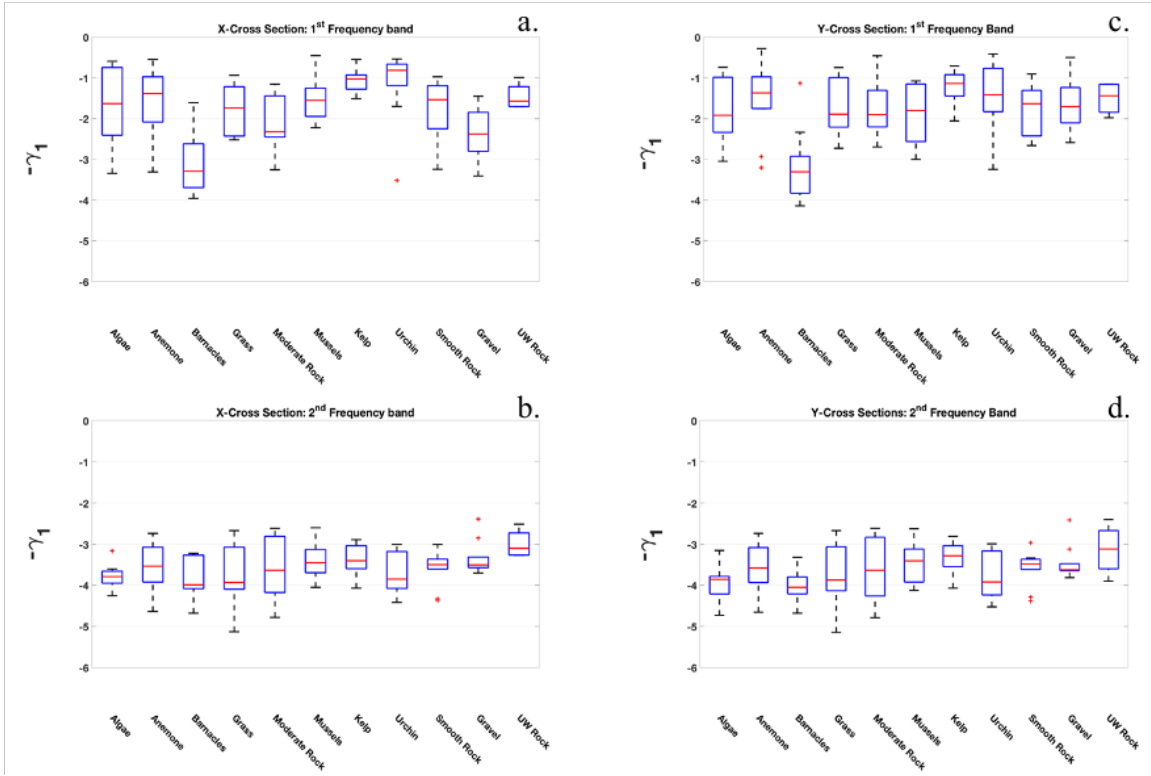
Box plots of $-\gamma_1$ (spectral slope) parameters for the 1-D components for the multitaper spectrum based on surface type. Values were kept negative based on the direction of the slope in the spectrums. The median value each surface is depicted by the red line in each box. The blue box represents 50% of the data, or the limits of the 25th percentile and the 75th percentile. The dashed black lines represent the upper and lower adjacent values and the red plus signs represent outliers within the data for each surface.

Figure 18. $-\gamma_1$ Boxplots Based on Multitaper Spectrum Estimates

Figures 16 and 17 show that both the spectral exponent values and the spectral slope values vary significantly between surface types, interclass, and for the same surface types but across the two frequency bands, intraclass.

For the ϕ_1 parameters, the values calculated for the 1st spatial frequency band in both the x and y directions (Figure 16, plots (a) and (c)) fluctuate roughly around 10^{-5} while the values for the 2nd spatial frequency band fluctuate just above 10^0 for all the surfaces identified (Figure 16, plots (b) and (d)). However, within the 2nd spatial frequency band there are more outlier values across the surface types than seen within the 1st spatial frequency band (Figure 16, plots (a) and (c)). There is also intraclass variability in

56

parameter value ranges between the spatial frequency bands. For all the surface types, the parameters span a larger range of values within the 2nd spatial frequency band than in the 1st spatial frequency band. This difference in outlier presence and intraclass value ranges between the spatial frequency bands could be due to a higher variability of the surface height at the smaller spatial scales or the fact that the end of the second spatial frequency band aligns with the limit of the spatial resolution that was attainable during the calculations, thus creating error as the spectrum slope reached that limit.

For the γ_1 parameters, there is also a marked intraclass difference between the two spatial frequency bands. Within the 1st spatial frequency band (Figure 17, plots (a) and (c)), the mean values fluctuate roughly between 1 and 3 for the surfaces, while in the 2nd spatial frequency band the mean values fluctuate between 3 and 4 (Figure 17, plots (b) and (d)).

However, unlike the first spatial frequency band, the interclass values ranges of γ_1 parameters within the second spatial frequency (Figure 17, plots (b) and (d)) are smaller for each surface type. There are also more outlier γ_1 parameter values within the 2nd spatial frequency band (Figure 17, plots (b) and (d)) than compared to the first the 1st spatial frequency band (Figure 17, plots (a) and (c)). The increase in outlier presence within the 2nd spatial frequency band again may suggest that the potential for increased error as the estimates reach the resolution limit.

Since the acoustic models use both parameters, the spectral slope and spectral exponent, in their respective calculations to classify surface roughness for modeling purposes, it is prudent to look at the relationship between the parameters for the various surface types. In order to do this, each ϕ_1 and $-\gamma_1$ pair was plotted and color coded based on surface type on a scatterplot, as shown in Figure 18.
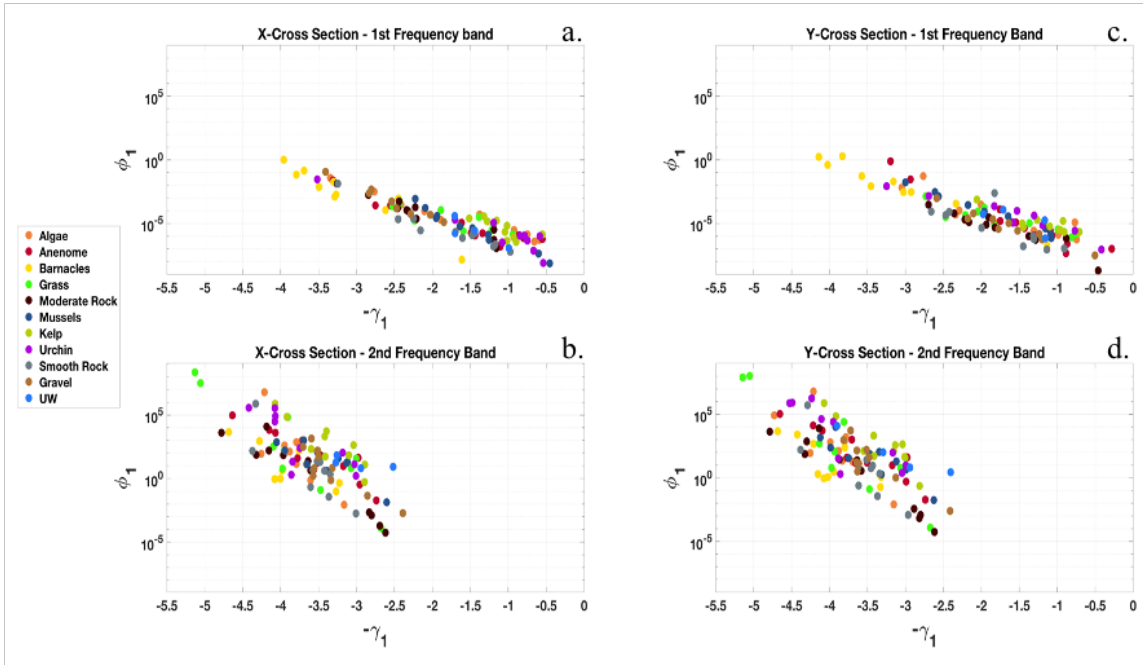
Scatter plots for each ϕ_1, $-\gamma_1$ pair based on surface type. Each surface is designated by a specific color based on the legend. The 1st spatial frequency band is plotted along the top row and the 2nd spatial frequency band is plotted along the bottom row. For both spatial frequency bands, the x-cross section variables are on the left and the y-cross section variables are on the right. For all four plots, the y-axis is a log-log scale while the x-axis is linear.

Figure 19. $-\gamma_1$ vs ϕ_1 Scatter Plots by Surface Type for the Multitaper Spectrum Estimates

Once again, these plots show an intraclass distinction between the first (Figure 18, plots (a) and (c)) and second spatial frequency bands (Figure 18, plots (b) and (d)), which aligns with the values of the individual parameters discussed in the previous paragraphs. However, with the points colored by surface type, it is possible to more clearly identify the interclass distinctions for the different surface types within both spatial frequency bands. For instance, on the scatter plots for the 1st spatial frequency band (Figure 18, plots (a) and (c)), the yellow dots, which denote surfaces covered with barnacles, tend to all be within the upper left half of the group of points, while the purple and sea green dots, which denote surfaces inhabited by urchins and surfaces covered in kelp respectively, tend to all be in the lower right half of the grouping of points. This relationship is highlighted by the colored areas on the plots (a) and (c) in Figure 19.

58

Within the 2nd spatial frequency band, the points denoting the various surfaces are not as clearly grouped. Instead, the surfaces follow a more 'linear' (in semi-log space) pattern within the second spatial frequency band with the points for each surface type spread throughout the entire length of the point cloud but aligned in a way such that a line could be fit to the individual surface identifiers. In some cases, it appears that these lines created by the various surfaces run parallel to one another. Again, noting the sea green dots (kelp) and yellow dots (surfaces covered in barnacles), the relatively parallel relationship between surfaces ϕ_1 and $-\gamma_1$ pairs can be seen. These more linear relationships are shown in the plots to the right in Figure 19. The linear relationship shown here highlights again the potential for higher intraclass surface height variability at the smaller spatial resolutions.

It is important to note that while there are both interclass and intraclass variations for these parameters, both the clustered relationship within the 1st spatial frequency band and the parallel 'semi-log linear' relationship identified in the 2nd spatial frequency band provide insight into the parameter ranges that could be considered for different surface types found along the rocky shoreline.
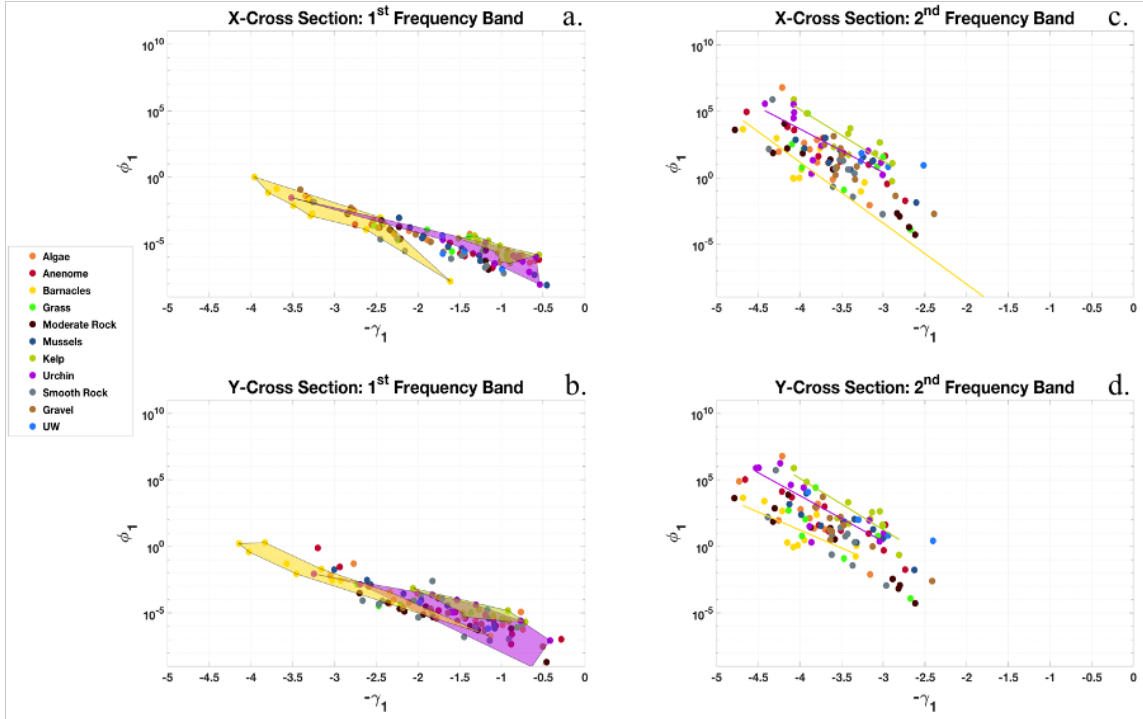
Scatter plots for each multitaper ϕ_1, $-\gamma_1$ pair based on surface type. The colored areas represent the groupings of the spectral pairs in the 1st spatial frequency band plots while the lines over the plots in the 2nd spatial frequency band represent the best fit lines for the pairs. For all four plots, the y-axis is a log-log scale while the x-axis is linear.

Figure 20. $-\gamma_1$ vs ϕ_1 Parameter Relationships: Multitaper Spectrum Estimates

D.   2-D EQUIVALENT SPECTRAL PARAMETERS w_2 AND γ_2

Even though the two spectral parameters, γ_1 and ϕ_1, have been identified in almost all of the previous studies of this type due to their acoustic applications, comparison of these values directly becomes difficult due to difference in parameter scales, variations in spatial frequency limits within the calculations, and the large amount of irregularity seen within the parameters themselves, even when collected within the same study.

To compare the spectral parameter values collected in this study to other data collected in a previous studies, the ϕ_1 and $-\gamma_1$ values from this study as well as the values

from the studies done in sandy seafloor environments found within Jackson and Richardson (2007) were converted to their 2-D equivalent spectral parameters w_2 and γ_2 and converted to meters (as needed) using the Eq. 10 and 11 from Chapter II of this paper. All the values were then plotted on scatter plots with values from this study identified by dots colored by the individual surfaces types and the values from the sand studies identified by the black diamonds. These plots are shown in Figure 21.
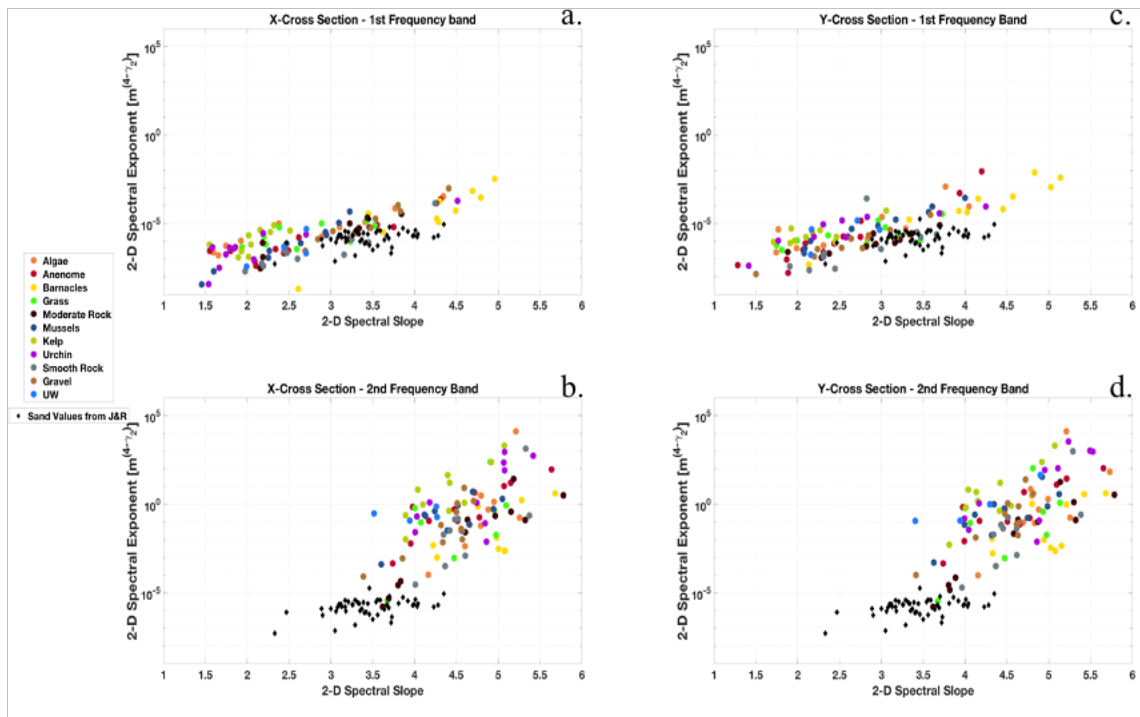
Scatter plots of the γ_2 vs w_2 parameters calculated for the multitaper spectrums. The colored circles represent the surface types collected in this experiment and the black diamonds represent the converted values from Table 6.1 in (Jackson and Richardson 2007) which was comprised data collected from the twelve studies discussed in the book and represent various sediment types.

Figure 21. γ_2 vs w_2 Scatterplots Comparing Rocky Seafloor Values to Sand Seafloor Values

It should be noted that the some of the sand studies discussed in Jackson and Richardson (2007) encompass data analyzed over larger areas and lower spatial resolutions

than the data from this experiment so the plotting of this data is not necessarily directly comparable but provides a good reference of values across different surface types (Jackson and Richardson 2007).

The plots (a) and (c) in Figure 20 show the relationship of the values collected here within the 1st spatial frequency band and the values collected in the previous sandy seafloor studies. There is an overlap between the rocky surfaces and the sandy seafloor values indicating that there may be some similarities between the roughness, or variations in RMS surface height of the rocky seafloor surfaces at the mm range and the variations in the RMS surface height of the sandy seafloor at slightly higher spatial resolution ranges since the data from Briggs (2002) found within the table was collected at special resolutions between 0.2 and 250 cm . The plots for the data collected for the second spatial frequency band, plots (b) and (d) in Figure 20, do not show the same correlation. In this spatial frequency band, there is almost no overlap between the rocky seafloor surface data and the sandy seafloor data. Indicating that the there is a significant difference in the roughness parameters of the sand at the cm scales and the roughness parameters of the rocky seafloor at the submillimeter scales.

E.   1-D FRACTAL DIMENSIONS

Continuing the evaluation of the parameters calculated in this experiment, the Fractal Dimension (D) parameter, which has been used in other studies as a seafloor classification feature of the surface environment, was evaluated from the 1-D parameters of the multitaper spectra. While this parameter has no new information since it is a function of the spectral slope, it is included as a discussion point to compare the values conducted in this study with the values collected in a coral reef environment. Figure 21. shows the fractal dimension values based on those 1-D parameters using the Eq. 13 (Russ, n.d.). Plots (a) and (c) depict the fractal dimension values for the x and y-cross sections for the 1st spatial frequency band plots (b) and (d) depict the fractal dimension values for the x and y-cross sections for the 2nd spatial frequency band. In general, the higher the fractal dimension value, the more jagged the surface is.

It should be noted that for a 1-D surface (like considered in this paper), any fractal dimension value less than 1 and greater than 2 is not considered fractal. Since the standard fractal dimension range of 1 to 4, infers that values of $D = 1$ equate to a uniform line (surface x or y-cross section), $D = 2$ equate to a plane, and values of $D = 3$ equate to a volume (3-D surface like a cube) (Vanderbilt, n.d), the values in the that are less than $D = 1$ may indicate that the features at those spatial scales may not significantly contribute to the surface variability using this calculation method.

$$D = \frac{\left(6 - |\gamma_1|\right)}{2}$$

(13)

The box plots show that the 1st spatial frequency band (spatial range of 8.9 to.4 mm) has significantly higher fractal dimension values than the 2nd spatial frequency range (spatial range of .4 to .02 mm). For the 1st spatial frequency band (Figure 21, plots (a) and (c)), the fractal dimension values range from 0.93 to 2.9 with the median values ranging from 1.35 to 2.60 across both the x and y-cross sections. Likewise, for the 2nd spatial frequency band (Figure 21, plots (b) and (d)), the fractal dimension values ranged from 0.43 to 1.81 with the median values ranging from 0.98 to 1.45 for the x and y-cross sections. These ranges indicate that the primary surface height variations here are caused by surface features that fall into the spatial range of 8.9 to 0.4 mm with potentially less variation in surface height coming from the features in the smaller spatial frequencies less than 0.4 mm.
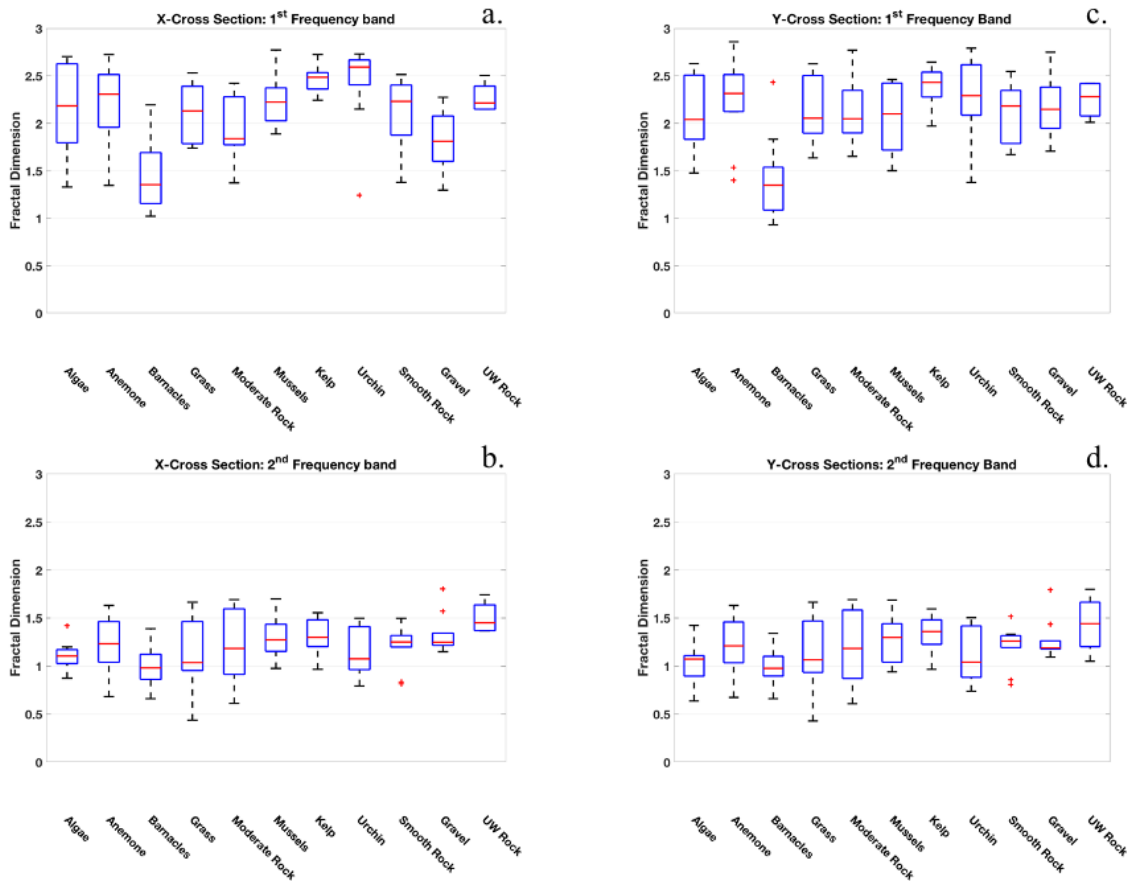
Multitaper spectrum fractal dimension (FD) calculations (based on 1-D parameters). The median FD value each surface is depicted by the red line in each box. The blue box represents 50% of the data, or the limits of the 25th percentile and the 75th percentile. The dashed black lines represent the upper and lower adjacent values and the red plus signs represent outliers within the data for each surface.

Figure 22.   Fractal Dimension Values Based on the Multitaper Spectrums

As noted in Chapter I, Leon et al. (2015) recently conducted an experiment that calculated fractal dimension values from estimated spectral parameters in order to describe the surface roughness of a coral reef environment. While that study was focused on a slightly different underwater environment, the coral reef environment has a lot of similarities to a rocky shoreline with regard to large- and small-scale surface features. The study was also conducted using a similar camera setup and data processing technique to this experiment, with roughness results resolved to the submillimeter scale. Therefore, the

The 2-D fractal dimension values obtained across the coral reef environment in (Leon et al. 2015) ranged from 2.2 to 2.59 with an average value of 2.45. While these values did not completely encompass the values found during this study, the range of values found within each should be noted. This type of comparison may indicate that the amount of variation of roughness spectral levels of the coral reef environment and the amount of variation roughness spectral levels of a few of the surfaces identified here may be comparable at the millimeter to submillimeter scale. The surfaces in this study that may be the most comparable to those found in the coral reef study also happen to be the surfaces that contain similar biological structures such as mussels, anemones, kelp, and urchins.

The potential similarities between the surface height variations at the mm and submillimeter scale on the rocky seafloor and the coral reef environments could benefit both fields of study in future work. Assuming the difficulties of underwater data collection, collection in air along the shore may provide insight to the roughness of the coral given specific composition is known. Additionally, since more studies have been conducted in the coral reef environment than in the rocky shoreline, it is possible that some of the coral reef roughness data could be used to estimate roughness along the rocky shore.

F.   SCATTERING STRENGTH

Scattering strength values were estimated using the small roughness perturbation method (SPM) (Jackson and Richardson, 2007) with input parameters encompassing the geoacoustic properties from Gruber (2019) which are outlined in Table 1, a 200 kHz center frequency, roughness parameters from each estimate spectra which are all found in Appendix B, and three grazing angles of 10°, 45°, and 60° as was discussed in Chapter II. Although the SPM is only valid for small RMS roughness compared to the acoustic wavelength, it can be used as an indicator of the possible range of values that could be encountered in scattering strength measurements.

For analysis of scattering strength at 200 kHz, only the first frequency band will be considered since the spatial scales of the second frequency band are likely not very important for scattering at 200 kHz based on the Bragg wave numbers. Scattering strength

values calculated for the spectral parameters from the 1st spatial frequency band are shown in Figure 22.

For the 1st spatial frequency band, the scattering strength across the three different grazing angles ranged from -54 dB to 27 dB with mean values for each surface across the three different angles ranging from -46 dB to 11.75 dB. While there is some variation in scattering strength between the three different grazing angles of 10°, 45°, and 60°, the main scattering strength variations seem to be primarily attributed to the surface type.

It should be noted that the high scattering strength values above -10 dB are most likely unrealistic, especially at low angles since scattering strength measurements conducted in comparable rocky environments have shown ranges between -33 and -26 dB for grazing angles of 20° and frequencies of 100 kHz in Olson et al., (2016) and ranges between -35 and -30 dB for grazing angles of 20° and frequencies of 201 kHz in Gruber, (2019). Additionally, a study conducted by McKinney and Anderson (1964) found that scattering strength actually decreases with frequencies over 100 kHz meaning that both the scattering strength data measured from Gruber (2019) and the scattering strength estimates from this study would be less than the scattering strength values found in Olson et al., (2016) given that the environments were similar enough over multiple spatial scales. Given the scattering strength values identified in this study, it is possible that the perturbation method used to calculate these scattering strength estimates overestimated the values significantly or is not a viable method given the spatial scales and spectral parameter values of the surfaces analyzed here. This method was shown to overestimate scattering strength by up to 8 dB in this type of environment by Olson et al. (2016) and it was theorized that the rms height values are significantly large as compared to the acoustic wavelengths (Olson et al., 2016). Given the scales and frequencies used in this study, it is possible that the same theory would apply to the surfaces identified here which could account for the very large scattering strength estimates attained in these calculations.

The recent study conducted by Gruber (2019) measured scattering strength (at 201 kHz) from the rocky outcroppings off Asilomar Beach, near to the locations in which data was collected for this study. In that experiment, scattering strength was estimated to be between -30 and -35 dB for a 10° grazing angle and between -25 dB and -30 dB for a 45°

grazing angle. While not all the data in the first frequency band collected in this experiment had scattering strength estimates that matched those measured values, a few of the surfaces identified within this study showed estimated scattering strength values that overlapped with the values identified in Gruber (2019). The surfaces identified with similar scattering strength values were the rock-specific surfaces (moderate and smooth), barnacles (which were rock surfaces covered in barnacles), and gravel. The overlap for these surfaces between the collected and modeled scattering strength values suggests that the perturbation model used in this study can potentially be used for surfaces along the rocky seafloor when the spectral parameter values are known, even at very small scales. However, this conclusion is probably limited to the exposed rock surfaces given the fact that surfaces with any biological presence, such as urchins or barnacles, can change much faster than the rocky structure on which they are located. Given the potential for this spatial and temporal variation, these scattering strength estimates may be inaccurate in other locations or times of year.

The other surfaces identified in this experiment such as grass, kelp, and algae may also be significant factors in the scattering but due to their interaction and movement within the water column, they most likely influence the volume scattering more than the seafloor scattering when underwater. Taking that into consideration, the scattering strength estimates show in the following figures for these surfaces are most likely highly inaccurate.
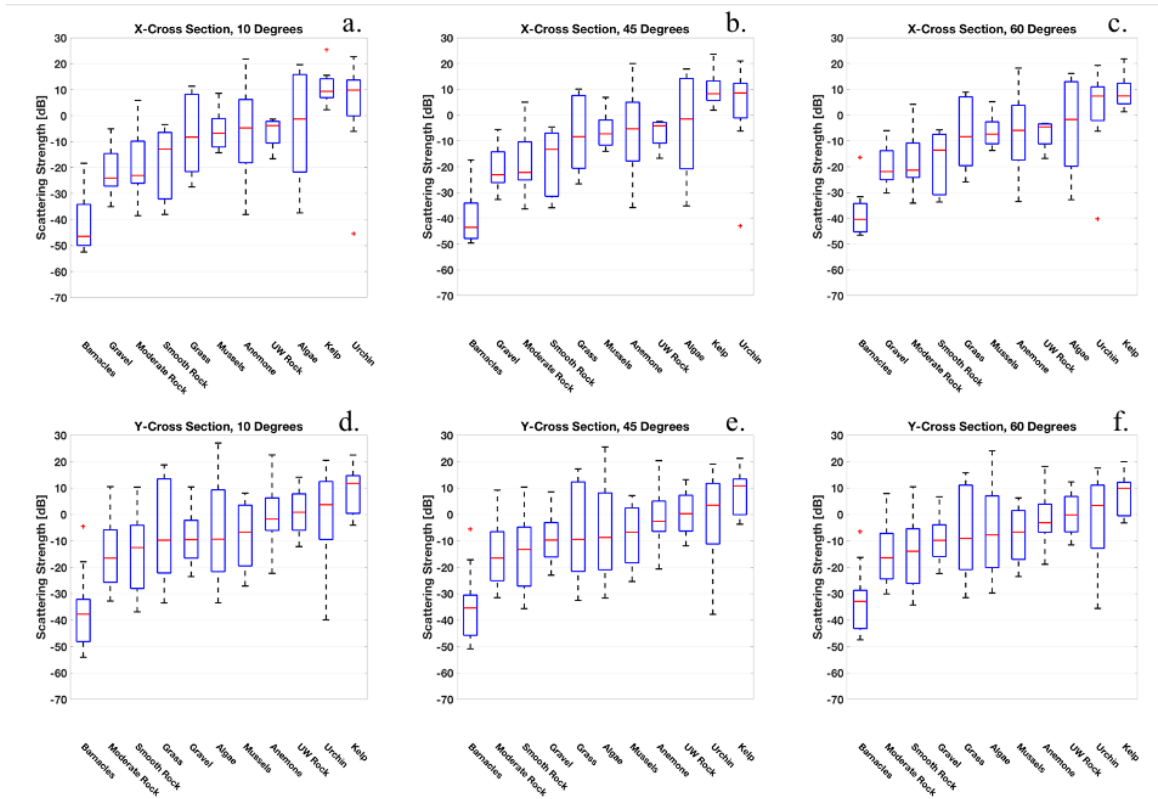
Scattering Strength box plots for the 1st spatial frequency band for them multitaper spectrum calculations at scattering and grazing angles of 10°, 45°, 60°. The median scattering strength value each surface is depicted by the red line in each box. The blue box represents 50% of the data, or the limits of the 25th percentile and the 75th percentile. The dashed black lines represent the upper and lower adjacent values and the red plus signs represent outliers within the data for each surface. Note that the x-axis for the plots vary slightly since the box plots are arranged lowest to highest (left to right) by median scattering strength value.

Figure 23.   Scattering Strength for the Multitaper Spectrums: 1st Spatial Frequency Band

G.   2-D RADIALLY AVERAGED SPECTRUM

The 2-D polar spectrum values were averaged along each radial and the mean spectrum for each surface was plotted in Figure 24. The figure shows that the surfaces fall into two groups between the spatial frequency range of 10^1 to 10^2 m^{-1}. The first group (algae, barnacle, moderate rock, smooth rock, and anemone) exhibits more energy within that spatial frequency range than the second group (kelp, grass, mussels, UW rock, and gravel). All the surfaces show the regression starting between $4*10^1$ and $6*10^1$ m-1 where

the slope is relatively consistent for most of the surfaces until approximately $3*10^2$m-1 where small fluctuations in the slope can be seen. Between $2*10^3$and $5*10^3$m-1 that largest fluctuations on the surfaces are visible before the slopes for all the surfaces steepen slightly. Between $6*10^1$m-1 and $4*10^3$m-1 the individual surface spectra overlap or cross one another significantly but once the slopes steepen between $4*10^3$m-1 and $5*10^4$m-1 the lines of each spectrum become more parallel to one another. These relationships match the spectral parameter values identified earlier in this chapter where there is a clear distinction between the spectral parameters and the two spatial frequency bands identified in these spectrum estimates.
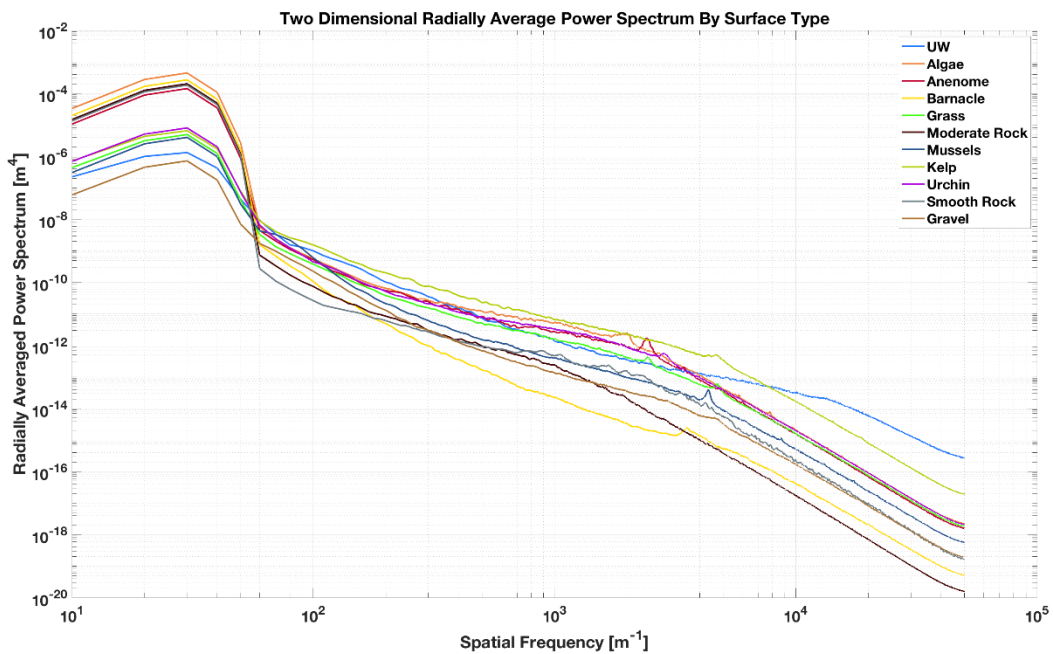
2-D radially average power spectrum by surface type. Each 2-D spectrum was average along each radial and then averaged across all radials to be plotted here by surface type.

Figure 24.   2-D Radially Averaged Power Spectrum

THIS PAGE INTENTIONALLY LEFT BLANK

IV.   CONCLUSIONS
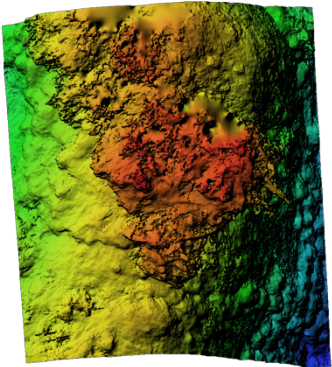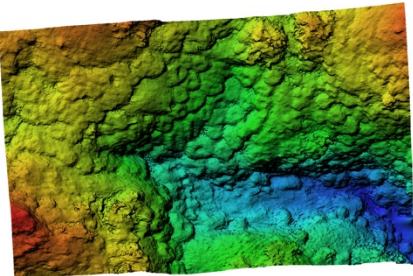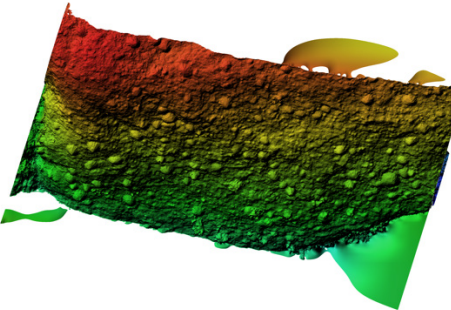
Roughness measurements between $O(10^{-3}$ m) and $O(10^{-5}$ m) were calculated for ten different surface morphologies along the rocky shoreline of the Monterey Peninsula. These roughness measurements were performed using photogrammetry techniques. Photographs were collected during extreme low tide events with both dual-camera, and single-camera setups with a reference object of known size placed within the field of view of the camera(s). The photographs were processed using commercial photogrammetry software (AgiSoft Metashape) to calculate 3-D representations of the different surfaces from which 1-D and 2-D roughness power spectral densities were estimated. Analysis of the roughness spectrum estimates showed power-law behavior across two distinct spatial frequency regions that correlated to spatial resolutions of 0.02 to 8.9 mm, with different slopes. The spectral parameters of ϕ_1 and γ_1 were derived from the roughness power spectrum estimates over both spatial frequency bands. The plotted spectral parameter values indicated that there was a clear distinction in the values for each parameter between the 1st and 2nd frequency bands across all the surfaces, potentially indicating a difference in variations in surface height between the mm and submillimeter scale surface features. Additionally, the wide range of values for each parameter for each surface within each frequency bands indicates additional potential for increased spatial variability of roughness characteristics present on each surface at these resolved scales along the rocky shoreline. This type of analysis also identified an overlap between the 2-D equivalent spectral parameters (when plotted in spectral pairs), of the mm scale features on the rocky seafloor surfaces and slightly larger scale roughness features of the sandy seafloors. Scattering estimates based on the estimated roughness parameters for the primarily rock dominant (not biological) surfaces of this study partially align with recently collected scattering measurements of the rocky outcroppings near the data collection sites, which was measured to be between -25 and -30 dB for grazing angles of 45° (Gruber, 2019), but the scattering strength calculations within this experiment tended to show more variation than the data collected by Gruber (2019).
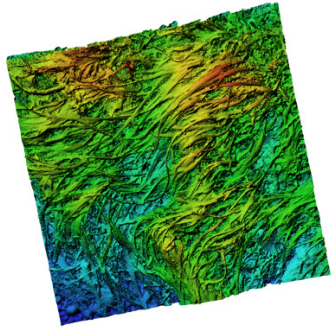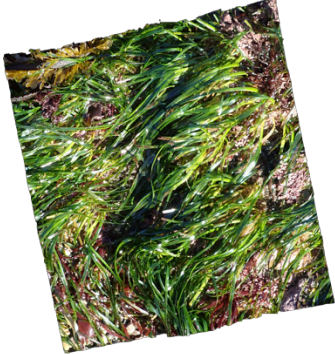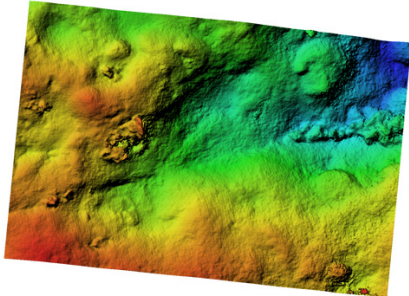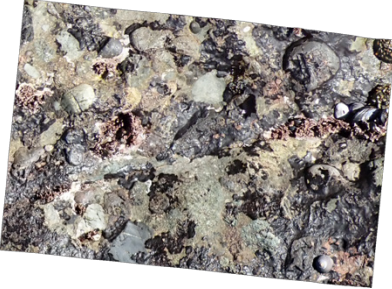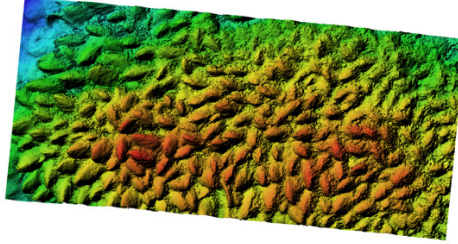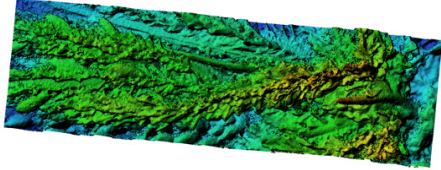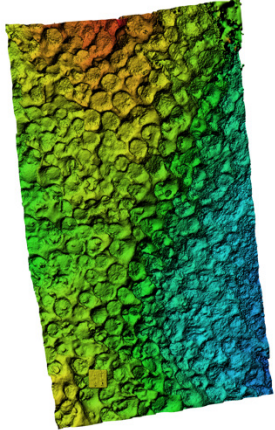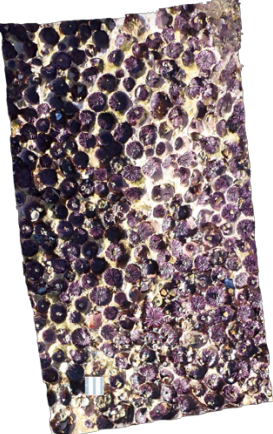
The portability and flexibility of these roughness measurement methods could easily be expanded to drone and satellite imagery collection. However, since a large number of high-resolution photographs are required to be processed using the highest thresholds in order to resolve features at smaller (mm to submillimeter) spatial scales, these methods would best be paired with the implementation of some automation into the data processing. Automation would potentially decrease processing time, allowing for larger areas or more distinct surfaces types found along the rocky coastline to be analyzed using these other means of imagery collection. If applied, these types of adaptations to the methods described in this paper would allow for an increase in data collection, roughness estimates, and ultimately the understanding of the acoustically relevant parameters that characterize the surfaces within the rocky seafloor environment.
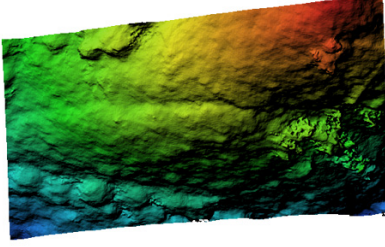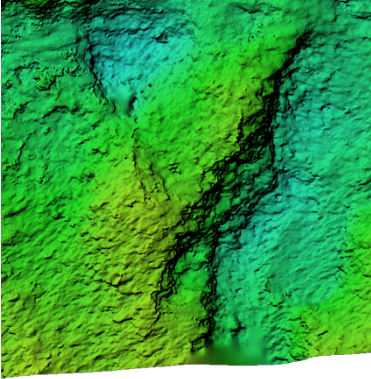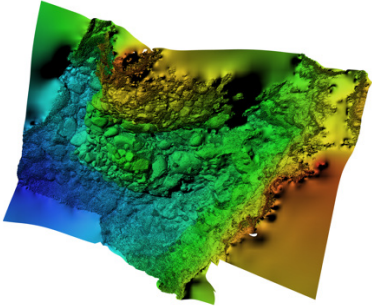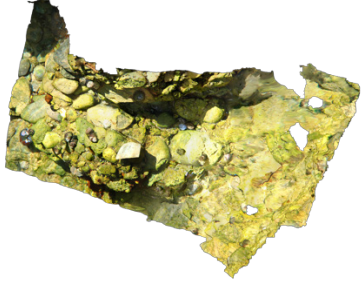
APPENDIX A: OUTPUT EXAMPLES FOR EACH SURFACE TYPE FROM METASHAPE PROFESSIONAL

The table within this Appendix provides an example of a Digital Elevation Map (DEM) and an Orthomosaic representation of the surface that were exported out of the AgiSoft Metashape Professional Software during image processing.

Table 1: Digital Elevation Map and Orthomosaic Representations of Each Surface

Surface Type	Digital Elevation Map (DEM)	Orthomosaic
Algae		
Anemone		
Barnacles		

73

Grass		
Moderate Rock		
Mussels		
Kelp		
Urchin		

Smooth Rock		
Gravel		
Underwater Rock		

THIS PAGE INTENTIONALLY LEFT BLANK

APPENDIX B: DATA TABLES

For all the tables below, phi refers to ϕ_1 and gamma refers to $-\gamma_1$. All values in these tables are based on meters. The values from the 2-dimensional spectrum in the third table are the parameters derived from the 1-D components of the 2-D spectrum output.

| | 1-Dimensional Multi-Taper Spectrum | | | | | | | | | | | | | |
| | X-Cross Section | | | | | | | Y-Cross Section | | | | | | |
Surface Type	Frequency 1	Frequency 2	Frequency 3	Section 1 - Phi	Section 1 - Gamma	Section 2 - Phi	Section 2- Gamma	Frequency 1	Frequency 2	Frequency 3	Section 1 - Phi	Section 1 - Gamma	Section 2 - Phi	Section 2- Gamma
Algae	110	990	49990	1.37774E-06	-0.74680419	914.9609288	-3.727467506	110	1490	49990	1.2637E-06	-0.98644988	1625.254414	-3.784117465
Algae	40	890	49990	0.000298836	-2.410015098	0.008657099	-3.16356195	110	1090	49990	4.98805E-05	-2.337815475	0.007992595	-3.155677135
Algae	70	890	49990	1.92856E-05	-1.887348447	14.7089261	-3.790841346	90	1190	49990	0.000101897	-2.289847401	22.28517159	-3.831857619
Algae	40	690	49990	3.06163E-06	-0.923675123	715.5543378	-3.793419465	90	1190	49990	5.70098E-07	-0.743249955	761.1846681	-3.799563701
Algae	70	890	49990	3.63832E-07	-0.656770131	413.3893394	-3.949105139	140	1490	49990	0.052213736	-2.766769219	626.9854632	-3.990185867
Algae	110	1990	49990	5.21642E-07	-0.5935874	6147937.184	-4.211730687	90	1990	49990	1.16937E-05	-0.766392489	6147937.184	-4.211730687
Algae	90	4990	49990	9.18897E-05	-2.105899289	135.1127773	-3.880846936	90	1490	49990	1.31276E-05	-1.834475518	133.9587487	-3.879658849
Algae	90	1990	49990	0.003081366	-2.764929835	90.63174497	-4.254644947	140	1990	49990	0.006282074	-3.047386794	90.63174497	-4.254644947
Algae	90	1490	49990	5.20096E-05	-1.377509291	13.1965432	-3.66025818	90	990	49990	0.000299033	-2.005420694	19.01886993	-3.696277716
Algae	140	9990	49990	0.037474411	-3.343617736	0.733553966	-3.603320666	90	1490	49990	2.69547E-06	-1.307634632	79342.28229	-4.729076099
Anemone	110	1290	49990	6.10351E-07	-0.549962842	42.69778103	-2.976954372	90	1390	49990	1.02786E-07	-0.281456049	41.27193876	-2.973607886
Anemone	140	1190	49990	1.49505E-07	-1.105583598	5.308540123	-3.559180295	90	5990	49990	0.029542384	-2.934024669	14.03225313	-3.654110292
Anemone	110	1290	49990	1.24469E-06	-0.857250533	1002.844579	-3.706416478	140	1190	49990	2.63593E-06	-1.091884337	992.32749	-3.705376633
Anemone	90	1190	49990	0.000254694	-2.552791515	40.86257292	-3.776238038	110	990	49990	4.58441E-08	-0.883304711	38.8458363	-3.77124154
Anemone	90	890	49990	1.73029E-06	-1.337850855	3905.617614	-4.068086157	110	1090	49990	2.54875E-07	-0.870170411	5063.469404	-4.093732405
Anemone	140	1290	49990	2.62931E-07	-1.088166116	16.83317532	-3.514280756	90	990	49990	1.16293E-06	-1.309213414	15.47229084	-3.505965985
Anemone	70	990	49990	1.15715E-06	-1.437589498	0.018325558	-2.738299027	90	990	49990	1.54119E-05	-1.751046949	0.018325558	-2.738299027
Anemone	90	1090	49990	1.79181E-06	-1.490141478	6903.325874	-4.149282568	110	1490	49990	4.18159E-06	-1.433845263	13397.02838	-4.214637039
Anemone	90	990	49990	0.000267993	-2.750809548	70.06709451	-3.47609002	90	990	49990	1.11256E-06	-1.065042087	70.06709451	-3.47609002
Anemone	140	890	49990	0.023695717	-3.308664327	91738.29984	-4.636999441	90	5990	49990	0.7536547	-3.198186126	109069.3876	-4.653843943
Anemone	90	1990	49990	1.1626E-05	-1.61593581	0.346341775	-2.954234558	90	1090	49990	1.17127E-05	-1.546824092	0.510639169	-2.992478215
Anemone	190	1490	49990	7.36894E-07	-0.800385951	9.432569841	-3.173491581	70	1490	49990	0.000127439	-1.756332094	9.432569841	-3.173491581
Barnacles	90	1990	49990	0.000914305	-2.447474121	4.29578107	-3.979773676	90	1490	49990	0.052320381	-3.573059565	2.96654578	-3.943382105
Barnacles	690	1490	49990	1.44591E-08	-1.611574636	158.3974756	-3.756745659	190	1990	49990	1.82724E-07	-1.133323971	242.8375669	-3.798756909
Barnacles	190	1190	49990	0.001217355	-3.284647256	0.99694596	-4.003365662	140	1490	49990	1.655298082	-4.140355378	1.215415663	-4.022887218
Barnacles	140	1190	49990	0.068907545	-3.791610612	0.096154781	-3.267645892	140	1990	49990	0.019807182	-3.156428814	0.182210895	-3.330514051
Barnacles	90	1190	49990	1.030279775	-3.958676617	0.443615642	-3.223471337	90	1490	49990	1.900457327	-3.830052368	1.186173407	-3.320365634
Barnacles	140	1190	49990	0.007372096	-3.49081767	0.925337262	-4.080324832	140	1990	49990	0.008642509	-3.454413339	0.893195334	-4.076898837
Barnacles	90	4990	49990	0.000112227	-2.619249935	914.815772	-4.277971824	140	1990	49990	0.000359264	-2.334755069	454.3586121	-4.209875798
Barnacles	90	39990	49990	0.01870029	-3.30051904	5.84289E-39	4.494873274	90	990	49990	0.002854516	-2.926503811	2534.379646	-4.425030618
Barnacles	140	4990	49990	0.135972447	-3.691282494	0.881611216	-4.074501268	110	1190	49990	0.394636182	-4.024288687	1.961105955	-4.152283582
Barnacles	90	1490	49990	0.001806902	-3.265809669	4488.715264	-4.680234573	110	1490	49990	0.002874362	-3.024207125	4488.715264	-4.680234573
Grass	140	1990	49990	0.000569549	-2.43117334	5.949044957	-3.974402525	140	1990	49990	3.29207E-05	-2.468231834	5.949044957	-3.974402525
Grass	140	19990	49990	0.000371272	-2.42964396	0.000124058	-2.671854563	140	19990	49990	0.001385763	-2.729473583	0.000124058	-2.671854563
Grass	140	2990	49990	7.30245E-06	-1.198699222	68865.95182	-3.905671328	110	1490	49990	1.47738E-06	-0.74702593	25934.60623	-3.809894477
Grass	90	1990	49990	1.34376E-06	-0.938309981	228737161.6	-5.128296871	110	1190	49990	8.30207E-07	-0.812198304	103113004.3	-5.04988489
Grass	140	5990	49990	0.000222182	-2.523657652	333.4223076	-4.094741135	110	2990	49990	6.69151E-06	-1.825171336	495.9010579	-4.133031395
Grass	140	2990	49990	0.000108779	-1.888734709	31983128.94	-5.053243149	140	3990	49990	0.000176594	-1.961551786	81890315.65	-5.144999908
Grass	110	990	49990	1.7045E-05	-2.234193579	0.123664457	-3.471638449	70	990	49990	4.39042E-05	-2.209422776	0.123664457	-3.471638449
Grass	110	4990	49990	2.80669E-06	-1.220018603	6.590369736	-3.073926867	110	1490	49990	1.08785E-05	-1.365024773	5.949789741	-3.063330944
Grass	140	1990	49990	3.16723E-05	-1.386182632	37.65570735	-3.001874654	140	1990	49990	3.49197E-06	-0.993481355	37.65570735	-3.001874654
Grass	90	1190	49990	2.48306E-06	-1.591940285	140.7190508	-3.953732245	90	990	49990	8.37436E-05	-2.046725906	114.7045514	-3.933560297
Moderate Rock	110	990	49990	3.22776E-06	-1.185567199	12238.84162	-4.183951982	90	690	49990	6.78797E-07	-0.880854735	7675.807974	-4.137824575
Moderate Rock	90	990	49990	5.0725E-07	-1.187836163	0.001250337	-2.802299594	90	1190	49990	1.30532E-05	-2.161462734	0.001239227	-2.801416211
Moderate Rock	70	1090	49990	0.00168908	-2.841973242	5.34719E-05	-2.61718287	90	1090	49990	0.000307315	-2.696689623	5.34719E-05	-2.61718287
Moderate Rock	110	990	49990	0.000525144	-2.43909093	0.002157697	-2.833315099	90	490	49990	5.2319E-07	-1.283136871	0.00368719	-2.886342691
Moderate Rock	90	1990	49990	0.00015828	-2.458361173	69.47886717	-3.964340556	90	790	49990	1.99777E-09	-0.458705274	26.96944207	-3.871164046
Moderate Rock	90	1090	49990	2.28829E-05	-2.207935503	4073.495912	-4.77885018	110	990	49990	4.89004E-06	-1.819560965	4371.417798	-4.785817793
Moderate Rock	110	990	49990	0.01326783	-3.256398036	4.41999934	-3.604116331	110	1490	49990	1.01859E-06	-1.375900685	3.511827356	-3.580970491
Moderate Rock	90	1990	49990	9.89543E-05	-2.32429336	0.000191082	-2.691214818	90	990	49990	6.08115E-05	-2.356862787	0.000687098	-2.817191171
Moderate Rock	110	1090	49990	1.13192E-07	-1.156524428	23.87429292	-3.634822203	110	1090	49990	3.00571E-05	-1.904405981	23.87429292	-3.634822203
Moderate Rock	190	2990	49990	0.000183092	-2.225453994	73.96029974	-4.320639374	90	790	49990	8.02312E-06	-1.935469706	75.61237878	-4.322678712
Moderate Rock	70	1090	49990	0.00011423	-2.336674567	162.4485392	-4.152295305	140	1990	49990	2.09907E-05	-2.21784501	733.6972939	-4.300699028
Mussels	110	1490	49990	1.26808E-06	-1.263442641	123.5776757	-3.517056917	90	1190	49990	7.21402E-07	-1.076944353	75.00810553	-3.467866996
Mussels	90	1990	49990	5.79525E-06	-1.637232329	3.979530057	-3.391432054	90	1090	49990	0.017679711	-3.000144008	1.909801656	-3.319044284
Mussels	140	5990	49990	5.10576E-07	-1.253332898	16.99540617	-3.131012821	140	1990	49990	1.27389E-05	-1.600950942	4.246465072	-2.995622005
Mussels	140	990	49990	4.41909E-08	-0.602041326	998.3298235	-3.6949369	90	1990	49990	3.67581E-05	-1.644494041	9991.175261	-3.921699948
Mussels	90	1090	49990	0.000861914	-2.224360407	38.06491331	-3.240674928	110	1990	49990	1.34562E-06	-1.084360486	110.0867512	-3.345149031
Mussels	90	1490	49990	7.60202E-09	-0.454458997	19.31463297	-3.118757358	90	1490	49990	3.963E-06	-1.152330135	19.31463297	-3.118757358
Mussels	110	1190	49990	4.16508E-06	-1.470759331	0.013398369	-2.60291503	110	1990	49990	8.83637E-05	-1.959851596	0.017203624	-2.62751782
Mussels	110	1090	49990	3.81172E-05	-1.936333701	13.65317989	-3.652751118	140	1990	49990	0.001329879	-2.564732597	36.03070479	-3.748241318
Mussels	90	1090	49990	2.63984E-05	-1.948075558	161.6638255	-3.943629854	90	1490	49990	0.002986718	-2.609384716	246.8241221	-3.98533983
Mussels	110	990	49990	0.000161172	-2.0939152	726.3628052	-4.050666617	90	1490	49990	0.000279796	-2.17303111	1520.988435	-4.123528066
Kelp	190	1090	49990	2.48266E-05	-1.51267155	12.46916393	-2.891112028	190	1990	49990	6.02103E-06	-1.098808914	42.0806896	-3.010776818
Kelp	140	4990	49990	1.47775E-05	-1.278441475	753452.4157	-4.070839604	110	4990	49990	3.2781E-06	-0.964697659	753452.4157	-4.070839604
Kelp	190	4490	49990	4.31938E-07	-1.016544483	205.8341987	-3.595486729	140	1990	49990	1.00968E-05	-1.461191556	129.0810867	-3.549589402
Kelp	190	1990	49990	2.14737E-06	-1.044359578	0.545591149	-2.892072047	140	5990	49990	0.000735717	-2.059222277	0.234543074	-2.810460631
Kelp	290	4990	49990	3.39518E-07	-0.894708712	52.7123989	-3.412379682	490	4990	49990	5.10411E-06	-1.447654516	52.7123989	-3.412379682
Kelp	290	1490	49990	1.3929E-06	-0.549215984	441.5819004	-3.038812953	140	1490	49990	1.51845E-05	-0.922455342	441.5819004	-3.038812953
Kelp	490	2990	49990	6.86363E-06	-1.016105278	70269.80146	-3.917469508	190	2990	49990	1.84323E-05	-1.266690072	70269.80146	-3.917469508
Kelp	90	3990	49990	1.66164E-05	-1.154286611	2024.926547	-3.420360906	190	3990	49990	2.24572E-06	-0.908862775	2024.926547	-3.420360906
Kelp	190	1990	49990	7.96397E-07	-0.930943845	69.29586023	-3.098063675	140	4990	49990	1.11717E-05	-1.176835672	120.7161553	-3.152615902
Kelp	140	4990	49990	3.77358E-05	-1.319655663	5351.841527	-3.395179173	90	1090	49990	2.14731E-06	-0.711102724	371.6529507	-3.133724873
Urchin	90	1290	49990	0.02837029	-3.514026261	21.36851243	-3.843481339	90	7990	49990	0.001423385	-2.693268401	32.53729383	-3.885385954
Urchin	490	2990	49990	1.9386E-05	-1.701728248	81961.39128	-4.066609016	140	1090	49990	8.72789E-08	-0.416497377	25704.76689	-3.952767041
Urchin	190	2490	49990	4.49609E-07	-0.746566538	13.55948843	-3.027662865	110	1490	49990	7.17589E-06	-1.193016856	9.613251362	-2.993865259
Urchin	240	1490	49990	1.12655E-06	-0.788238442	371036.0669	-4.416784045	110	1990	49990	0.000234543	-1.829570518	795600.8833	-4.491769049
Urchin	110	1190	49990	1.03334E-06	-0.842408048	1.660454737	-3.006809632	110	1490	49990	1.13247E-05	-1.579918617	2.440862433	-3.044759115
Urchin	140	1490	49990	7.39251E-08	-0.665575155	261.9062995	-3.744606142	490	4990	49990	8.88886E-10	-0.635466832	761699.2938	-4.524693711
Urchin	90	990	49990	3.2245E-07	-1.078213416	340763.8	-4.075717322	110	1490	49990	4.07323E-05	-1.3040354	1730190.717	-4.235910283
Urchin	110	1190	49990	9.9778E-07	-0.584520873	30684.70391	-4.075862576	190	1490	49990	9.51886E-05	-1.530174983	42671.6141	-4.108351754
Urchin	90	1590	49990	1.11434E-05	-1.191189948	107.307548	-3.180832782	110	1190	49990	2.61076E-06	-0.766857075	92.8245612	-3.16654744
Urchin	140	990	49990	8.06245E-09	-0.539157077	2.025714004	-3.859550838	70	990	49990	0.008671413	-3.246079976	2.025714004	-3.859550838
Smooth Rock	140	1190	49990	1.60309E-07	-1.194922745	5.039115616	-3.572927901	90	1490	49990	1.5836E-07	-1.446016502	7.717191906	-3.61491798
Smooth Rock	90	1490	49990	7.12477E-07	-1.602716104	783037.0049	-4.327124305	90	3990	49990	0.002489835	-1.82478106	526941.5889	-4.288104096
Smooth Rock	90	1990	49990	1.2542E-06	-1.475191722	2.180319802	-3.345228525	110	1190	49990	6.05266E-07	-1.307339991	2.089774513	-3.341048295
Smooth Rock	140	2990	49990	1.73396E-06	-1.439892286	22.64784424	-3.519572573	110	990	49990	1.08489E-07	-0.907620747	8.959357718	-3.428424086
Smooth Rock	140	1490	49990	6.07712E-08	-0.97315918	4.10350778	-3.421272232	140	1990	49990	8.69881E-08	-1.138820149	5.722276208	-3.453971589
Smooth Rock	140	1190	49990	2.23516E-07	-1.173688772	19.23092408	-3.481545018	140	1490	49990	9.97405E-07	-1.315763129	26.11328612	-3.51168595
Smooth Rock	140	1190	49990	2.83138E-06	-2.156006352	0.036256121	-3.365235425	110	990	49990	4.50722E-05	-2.468702091	0.037078488	-3.367452219
Smooth Rock	110	1090	49990	2.15361E-05	-2.449100651	146.3658988	-4.371563172	90	1190	49990	4.5869E-06	-1.995764785	165.2925654	-4.383560423
Smooth Rock	110	890	49990	2.3938E-05	-2.249622429	0.001837171	-3.008052604	70	1490	49990	7.92385E-05	-2.425282913	0.001177479	-2.964237167
Smooth Rock	40	890	49990	0.013303814	-3.244637881	0.211281837	-3.605377848	90	990	49990	8.66276E-05	-2.660971799	0.238075948	-3.61717408
Gravel	140	4990	49990	2.26666E-06	-1.695202098	162.0183887	-3.510963423	140	4990	49990	5.55363E-07	-1.199314569	162.0183887	-3.510963423
Gravel	90	2490	49990	0.000152689	-2.474034319	0.76186354	-3.337881788	90	9990	49990	0.000997246	-2.587646442	13.1848617	-3.614547207
Gravel	90	1090	49990	4.90541E-05	-2.025746426	306.8208267	-3.703174949	90	2990	49990	1.51504E-06	-1.238169883	961.3748812	-3.815577775
Gravel	240	3990	49990	2.65849E-06	-1.451987624	52.2695589	-3.501110319	140	1990	49990	1.03434E-05	-1.637756601	40.12977012	-3.475153137
Gravel	90	4990	49990	5.4853E-05	-2.28240479	7.057274848	-3.315601454	90	1990	49990	6.33078E-05	-2.106205685	1.010409476	-3.125501846
Gravel	140	1190	49990	0.000551195	-2.535137714	0.043572308	-2.854761619	140	8990	49990	3.72749E-06	-1.773933773	139.2302036	-3.640760198
Gravel	140	4990	49990	1.32287E-05	-1.846622596	1.662651137	-3.570742757	140	3990	49990	2.40358E-05	-2.177566575	3.180498605	-3.633831436
Gravel	90	690	49990	0.116733374	-3.408256779	0.001921813	-2.389051824	90	990	49990	2.11988E-05	-1.849185081	0.002462984	-2.413589025
Gravel	90	9990	49990	0.004730162	-2.802626218	6.441929515	-3.555023519	90	1490	49990	2.66132E-06	-1.523369261	16.56696535	-3.64534528
Gravel	90	1240	49990	0.002350994	-2.829784241	1385.391204	-3.592866998	190	1990	49990	3.01189E-08	-0.501431256	5174.322322	-3.722506504
UW Rock	90	3990	49990	1.71344E-06	-1.70182169	69.18962558	-3.25921682	90	4990	49990	0.000119727	-1.712865357	100.6683977	-3.295674256
UW Rock	90	3990	49990	2.74625E-06	-1.441378247	18.33159985	-3.269042097	90	6990	49990	5.53872E-05	-1.978001971	12220.44415	-3.899896935
UW Rock	110	9990	49990	3.95244E-05	-1.704980582	8.690155641	-2.515365688	110	6990	49990	1.76971E-05	-1.1650132	2.706234323	-2.402760721
UW Rock	190	4990	49990	1.15245E-07	-0.992702637	6.663869822	-2.94065375	190	4990	49990	6.71442E-07	-1.157180306	6.663869822	-2.94065375

78

	1-Dimensional P-Welch Spectrum													
	X-Cross Section							Y-Cross Section						
Surface Type	Frequency 1	Frequency 2	Frequency 3		Section 1 - Phi	Section 2 - Phi	Section 2- Gamma	Frequency 1	Frequency 2	Frequency 3		Section 1 - Gamma	Section 2 - Phi	Section 2- Gamma
Algae	70	1190	49990	1.25727E-06	-0.795007127	609.279016	-3.534616058	90	990	49990	6.55155E-08	-0.420670638	2129.477475	-3.798184525
Algae	90	1090	49990	2.7249E-05	-2.183493746	0.010033918	-2.882969053	90	990	49990	4.07253E-05	-2.254619604	0.027758296	-3.275508873
Algae	40	890	49990	3.76167E-05	-2.125126317	1.270287838	-3.435377819	70	990	49990	2.92497E-05	-2.172493966	71.02683931	-3.959478426
Algae	70	790	49990	2.08523E-07	-0.882521224	0.824534119	-3.093702552	70	990	49990	5.003E-07	-0.646719057	3796.290263	-3.952499493
Algae	70	890	49990	1.30419E-06	-1.145849078	11.4364417	-3.432516392	90	890	49990	5.85317E-07	-1.233275253	21.37069731	-3.668107537
Algae	90	1490	49990	5.1365E-07	-0.807304727	34.97427907	-3.121065144	90	1490	49990	8.93354E-05	-1.373404363	7080.311889	-3.649665389
Algae	90	1090	49990	2.47996E-06	-1.69638435	0.928722899	-3.403365764	40	790	49990	4.43328E-08	-0.933149287	15.3268588	-3.711164084
Algae	70	1090	49990	2.38088E-05	-2.367207221	0.003486331	-3.01494779	90	1990	49990	0.000198556	-2.820291133	0.001161183	-3.066245222
Algae	90	890	49990	7.7046E-05	-1.605070242	152.5554335	-3.723621161	70	890	49990	0.000129186	-1.821131273	59.13430226	-3.822179466
Algae	110	1190	49990	3.91718E-05	-2.57049436	0.009854122	-3.209268225	90	1190	49990	5.32776E-08	-1.335829332	0.65621184	-3.580745719
Anemone	110	1390	49990	7.57611E-08	-0.18174348	3023.461061	-3.415307412	60	1290	49990	6.80924E-08	-0.184768143	170.7980055	-3.098298481
Anemone	70	1190	49990	4.12466E-07	-1.175945247	81.36729136	-3.721371021	110	1190	49990	0.000211163	-2.144319307	7.942803931	-3.623119301
Anemone	90	1490	49990	1.6538E-07	-0.62558292	46.50673277	-3.254574942	110	1490	49990	1.98713E-07	-0.65636436	2228.242088	-3.762916595
Anemone	90	890	49990	0.000917541	-3.079897848	0.001621487	-3.04767413	90	990	49990	4.10891E-09	-0.544236198	24.54696099	-3.756690165
Anemone	70	890	49990	7.21322E-08	-0.783393391	21.12980426	-3.649893099	90	1090	49990	2.29042E-07	-1.149193516	0.278137378	-3.2073681
Anemone	90	1490	49990	3.27489E-07	-1.109554535	13.57983069	-3.548013536	110	1290	49990	1.09762E-08	-0.478515881	115.2947787	-3.670734124
Anemone	90	1090	49990	1.3782E-07	-1.032829615	8.486370175	-3.64931598	70	1090	49990	2.68993E-06	-1.487208016	0.008004753	-2.624247364
Anemone	70	1090	49990	5.09376E-07	-1.583985355	3.611801288	-3.872383448	110	1290	49990	1.42879E-06	-1.381595963	57.67396838	-3.693062423
Anemone	90	990	49990	4.47848E-05	-2.652712049	0.326739281	-3.720319624	70	990	49990	2.47002E-06	-1.27379183	15.04340004	-3.384510836
Anemone	90	990	49990	2.23332E-05	-2.652175209	0.020108294	-3.530748424	70	790	49990	0.000838299	-2.681952377	0.142439235	-3.34653677
Anemone	90	1990	49990	1.8357E-06	-1.310416356	0.839554201	-3.029466668	90	1090	49990	9.27636E-07	-1.153762865	1.430856618	-3.098715106
Anemone	40	1190	49990	1.17534E-07	-0.727037631	135.5983739	-3.544315469	40	1090	49990	5.67443E-06	-1.597017778	6.355829058	-3.13161316
Barnacles	140	1490	49990	0.004235787	-2.779783724	1.3647E-05	-2.158947067	110	990	49990	0.067772355	-3.693110971	0.137458264	-3.663232965
Barnacles	90	1190	49990	0.112202278	-4.029109803	0.168789017	-3.883522921	190	1490	49990	1.7453E-07	-1.110771546	623.9537247	-3.90746813
Barnacles	90	1190	49990	0.0014918	-3.425530783	0.189452042	-3.952997127	110	1490	49990	0.025366544	-3.713153667	0.068085942	-3.727306695
Barnacles	110	1190	49990	0.190181494	-4.039321364	0.132979792	-3.801093945	140	1490	49990	0.003465539	-2.918609141	0.065962439	-3.256689438
Barnacles	90	1490	49990	0.044836271	-3.578426405	0.007498385	-2.827351127	90	1490	49990	0.322196431	-3.643776176	0.045649258	-3.038701815
Barnacles	140	1090	49990	0.000339132	-3.16991533	0.061669746	-3.818520232	140	1190	49990	0.005195784	-3.580009777	0.102290019	-3.866818078
Barnacles	90	1490	49990	0.000836792	-2.991935503	0.037181508	-3.460771977	90	4990	49990	7.78882E-06	-2.160849169	250.4156473	-4.148021296
Barnacles	90	9990	49990	0.000292372	-2.856225568	255.2522153	-4.220766991	110	4990	49990	5.75545E-05	-2.538542712	31.29237723	-4.007171816
Barnacles	110	4990	49990	6.65381E-05	-2.802123257	0.005313913	-3.436785969	110	1090	49990	0.003039003	-3.43340331	0.137672793	-3.885356534
Barnacles	90	990	49990	0.015127886	-3.781787674	0.122138917	-3.901813691	110	1490	49990	0.000451596	-2.969803935	0.052163487	-3.460964546
Grass	90	990	49990	0.000723017	-2.949457338	0.001827469	-3.172466199	110	1090	49990	0.000314129	-2.932616508	1.338499117	-3.846780606
Grass	70	790	49990	0.005722327	-2.916916981	0.350787077	-3.285613087	90	1190	49990	0.000109469	-2.432509406	0.606367442	-3.485055566
Grass	110	1490	49990	3.47054E-06	-1.101934791	0.00699684	-2.229058092	110	1090	49990	1.43987E-07	-0.527101975	775.9019233	-3.548131627
Grass	90	1690	49990	3.09462E-07	-0.860875407	2014.363888	-3.716394342	90	1090	49990	4.20201E-08	-0.723308474	48.48578363	-3.633084008
Grass	110	990	49990	0.000718412	-2.92369916	0.000169546	-2.65969428	110	2990	49990	1.32726E-06	-1.670950417	39.12520301	-3.913032176
Grass	110	1090	49990	2.71764E-05	-1.614080821	0.020808298	-2.644386067	90	1090	49990	8.08133E-05	-2.186618746	46.9756089	-3.756281875
Grass	90	990	49990	7.12113E-06	-2.135756332	0.262163804	-3.410782712	110	990	49990	0.000200689	-2.811122981	0.008074848	-3.214322976
Grass	110	1190	49990	5.16855E-07	-0.956567314	137.9951997	-3.394210954	110	1990	49990	0.000194352	-1.979568724	1.014516529	-2.949249084
Grass	110	1990	49990	5.50291E-07	-0.930476396	628.9271575	-3.511897351	110	1490	49990	2.83817E-06	-1.056332741	28.11885966	-3.0489229
Grass	110	1190	49990	6.77239E-06	-2.073086707	0.001033208	-2.778662818	90	1090	49990	0.003899403	-2.965818662	0.829456675	-3.479061842
Moderate Rock	90	990	49990	1.63915E-06	-1.256605949	57.46144988	-3.863029934	90	490	49990	1.67583E-05	-1.545505414	15.29934768	-3.573159572
Moderate Rock	70	1090	49990	6.3913E-08	-0.837920085	61.29410953	-3.610091463	90	1090	49990	6.95569E-07	-1.748964226	0.000703839	-2.771758288
Moderate Rock	90	990	49990	0.001659637	-2.983762084	2.401111426	-3.682430366	70	790	49990	3.21857E-05	-2.454262577	3.66888E-06	-2.389527073
Moderate Rock	70	890	49990	0.000327906	-2.33777614	12.0779433	-3.90933032	70	490	49990	5.16451E-07	-1.286359936	0.000871213	-2.745429239
Moderate Rock	70	990	49990	2.93954E-05	-2.552784972	0.204212748	-3.714741709	90	990	49990	3.23498E-09	-0.646130398	6.673373037	-3.779526299
Moderate Rock	90	1090	49990	7.66772E-07	-1.761104433	365.9738795	-4.302396919	110	890	49990	0.000261401	-2.945283366	0.215093967	-3.811589836
Moderate Rock	90	890	49990	0.012791078	-3.254903091	1.289481368	-3.99272494	90	990	49990	7.62214E-07	-1.51725736	1.217701018	-3.496972209
Moderate Rock	70	1090	49990	7.02256E-06	-1.893699026	6.908986723	-3.827512266	90	890	49990	0.001155709	-2.937520453	0.000205863	-2.692620657
Moderate Rock	90	1090	49990	5.9487E-07	-1.474022596	14.8296424	-3.860710857	70	990	49990	9.93924E-06	-1.772247979	16.29805363	-3.648785474
Moderate Rock	110	890	49990	5.23784E-06	-1.854796656	22.43501243	-3.942597313	90	990	49990	9.06999E-06	-2.208808052	0.758816525	-3.879002542
Moderate Rock	70	990	49990	5.16638E-06	-1.886619925	0.012427671	-3.025063166	90	1490	49990	3.73469E-06	-2.086931696	3.066255186	-3.781430772
Mussels	90	1090	49990	1.3833E-05	-1.739203576	4.424065623	-3.284375237	90	1990	49990	6.92622E-07	-1.3778519	10.30964718	-3.387348488
Mussels	90	1490	49990	3.39875E-06	-1.816836726	0.110131313	-3.091962676	110	1090	49990	0.056619051	-3.336318716	0.052685298	-3.032104099
Mussels	110	4990	49990	3.2915E-07	-1.199084114	20411.98054	-4.055393675	90	2990	49990	3.10543E-06	-1.459309043	1.558476894	-3.000678142
Mussels	90	1090	49990	3.35718E-08	-0.509398414	0.141688129	-2.799574242	90	1090	49990	4.95721E-06	-1.50009012	32.77989257	-3.363918416
Mussels	70	990	49990	8.63504E-05	-1.75663176	0.927454197	-2.869896776	70	1090	49990	9.06436E-05	-1.819952074	83.34601872	-3.28277137
Mussels	90	1090	49990	7.52094E-08	-1.178884434	76.2322072	-3.787703931	90	1190	49990	3.67873E-06	-1.077075293	99.76043299	-3.249705377
Mussels	90	890	49990	4.48001E-07	-1.113443079	5.539689275	-3.29059732	110	1490	49990	2.48417E-05	-1.758289751	0.021228154	-2.605418775
Mussels	90	990	49990	0.000440336	-2.477801712	0.114149512	-3.034929223	110	990	49990	0.042016595	-3.288379146	0.602126127	-3.372137892
Mussels	90	1090	49990	6.25014E-06	-1.834952641	0.790883373	-3.335968413	90	990	49990	0.006640533	-2.891774748	17.51913875	-3.761875086
Mussels	90	890	49990	4.45256E-06	-1.672270676	1.684370175	-3.262837617	90	1490	49990	0.001845898	-2.629004873	70.13838164	-3.854342866
Kelp	190	1490	49990	1.49048E-06	-1.301644266	1.2887946	-2.950054214	190	1990	49990	1.63057E-05	-1.315992869	58.10235711	-3.09727932
Kelp	90	1490	49990	3.7141E-06	-1.077989201	1534.316697	-3.576506959	140	2990	49990	9.77406E-06	-1.391385032	307.4798756	-3.419520436
Kelp	110	4990	49990	1.12032E-06	-1.498451246	463.2211361	-3.825636202	190	1490	49990	8.11831E-06	-1.515916087	2.609485433	-3.228433984
Kelp	110	1090	49990	2.24617E-06	-1.145853924	1.092153802	-2.754819715	90	1090	49990	8.33554E-06	-1.414668988	0.450701665	-2.885884588
Kelp	190	1190	49990	1.9643E-09	-0.353112015	12.22331385	-3.339004586	110	1990	49990	5.03025E-06	-1.483718202	55.95550853	-3.457303798
Kelp	90	1190	49990	1.775E-06	-0.608850189	2218.065336	-3.280061829	140	1990	49990	3.45587E-06	-0.662874889	2522.041125	-3.214978911
Kelp	140	1490	49990	2.6289E-06	-0.994765501	108.1165921	-3.13541827	110	1990	49990	3.53495E-05	-1.57324305	3673.552282	-3.664314332
Kelp	110	1990	49990	4.02235E-06	-1.03695913	811.5525735	-3.382660997	490	2490	49990	6.41668E-06	-1.197194038	225.8119654	-3.29661008
Kelp	190	1990	49990	5.86123E-08	-0.574948396	3.664585426	-2.878704586	140	4990	49990	5.7721E-06	-1.19440099	113.4059603	-3.183153045
Kelp	190	1990	49990	2.33066E-05	-1.190798887	1042.235264	-3.38978905	140	1490	49990	3.82099E-07	-0.471535776	680.6756101	-3.219341701
Urchin	90	1190	49990	0.024221071	-3.568019708	0.531421754	-3.79114029	110	1490	49990	0.000197024	-2.582510857	4.009632149	-3.711994298
Urchin	190	1140	49990	1.40507E-06	-1.485907353	0.019270124	-2.790957214	70	1090	49990	1.66157E-07	-0.675239366	653.8610518	-3.673594225
Urchin	90	2490	49990	3.13043E-07	-0.853525829	1.16603207	-2.910011934	90	2990	49990	4.56962E-06	-1.137471426	40.31950605	-3.177288752
Urchin	140	1990	49990	1.301E-07	-0.685015029	603.4779585	-3.553091262	110	1990	49990	2.26825E-07	-1.089107874	1143.392532	-3.903145981
Urchin	90	1190	49990	1.6426E-06	-0.965989417	0.398883299	-2.666135734	140	1990	49990	1.01732E-06	-1.175514092	10.05670422	-3.151564575
Urchin	110	1190	49990	1.37396E-07	-0.883275943	256.0596122	-3.597917948	490	4990	49990	5.25043E-11	-0.306717195	2950542.006	-4.670925806
Urchin	90	990	49990	2.51382E-08	-0.614442224	0.011877565	-2.572479602	110	1490	49990	2.54903E-05	-1.634912981	150.0812915	-3.466987209
Urchin	90	1990	49990	1.87375E-06	-0.929124858	2790.803118	-3.762987638	190	2990	49990	4.60155E-05	-1.651049546	3917.770046	-3.948645327
Urchin	90	1990	49990	2.43338E-05	-1.275382804	7.259018623	-2.866845271	90	990	49990	7.57469E-08	-0.381092842	4.445280919	-2.925287996
Urchin	90	990	49990	1.36161E-08	-0.67772691	31.30086694	-3.638207811	70	990	49990	0.002442316	-3.223895355	0.105282037	-3.579078777
Smooth Rock	110	1190	49990	1.01254E-08	-0.915884183	1.912385076	-3.490477916	90	1490	49990	8.32483E-08	-1.401091871	10.34990191	-3.671608134
Smooth Rock	90	1090	49990	1.33756E-06	-1.875329978	1.932337041	-3.72641583	90	3990	49990	0.000811021	-1.828106338	5194.974538	-3.925308439
Smooth Rock	110	1490	49990	5.6187E-07	-1.418464414	1.772282237	-3.367636422	110	1190	49990	3.70277E-08	-0.970238277	1.130839068	-3.320767953
Smooth Rock	110	1990	49990	2.02202E-06	-1.523753438	7.314393558	-3.458218129	110	1090	49990	4.70207E-06	-1.632153123	2.052256911	-3.337788057
Smooth Rock	90	1490	49990	4.34459E-08	-0.931499082	12.12666467	-3.516634345	110	1990	49990	7.71539E-08	-1.112907458	9.734635341	-3.500281988
Smooth Rock	140	1190	49990	6.97261E-08	-1.029903382	6.345231013	-3.527712585	90	1190	49990	1.42011E-06	-1.391223968	22.43320901	-3.518257202
Smooth Rock	70	790	49990	1.97346E-05	-2.565290788	8.24262E-06	-2.55122119	90	990	49990	1.31315E-06	-2.001401885	0.059695918	-3.444414198
Smooth Rock	70	1090	49990	0.000162371	-2.841479673	0.53650098	-3.888510222	90	990	49990	9.23891E-06	-2.294643659	0.446305707	-3.807739357
Smooth Rock	90	890	49990	1.06663E-05	-2.11097288	0.216644857	-3.465271016	90	990	49990	0.000230332	-2.697392669	0.000107336	-2.76246334
Smooth Rock	70	890	49990	9.77739E-05	-2.909372532	0.163078587	-3.823519951	70	790	49990	4.23694E-06	-2.237057184	0.143184267	-3.592844805
Gravel	90	1990	49990	0.000801965	-3.036570582	0.004325	-3.157295391	140	2990	49990	1.21219E-06	-1.5819793	1.137701541	-3.139771654
Gravel	110	1990	49990	0.000260586	-2.784912988	0.004882078	-3.059739075	90	9990	49990	0.001032032	-2.587424355	92.07477422	-3.794245811
Gravel	90	1190	49990	5.6251E-05	-2.090649327	17.29561544	-3.561656911	90	3990	49990		-1.468877745	11.40689278	-3.432836211
Gravel	140	1990	49990	1.04507E-06	-1.35691789	37.69586267	-3.567285644	90	2990	49990	2.45838E-06	-1.448433337	36.38342234	-3.495559084
Gravel	40	490	49990	0.000179829	-2.548379957	1.93859E-06	-2.167190188	90	1190	49990	4.79981E-07	-1.30995842	5.611060662	-3.289518426
Gravel	110	1490	49990	1.5227E-05	-1.993468292	0.94626472	-3.298574516	110	9990	49990	5.25326E-06	-1.799615822	5127.265467	-3.970731723
Gravel	140	1490	49990	1.52694E-06	-1.667432483	0.135899749	-3.102867446	140	1190	49990	2.25526E-06	-1.894157726	0.073685843	-3.30584756
Gravel	140	1190	49990	0.002143986	-2.845008852	5.38787E-06	-1.917872671	90	1090	49990	8.84972E-07	-1.249513322	0.007899895	-2.483093679
Gravel	90	2990	49990	0.000373689	-2.475405198	5.864733498	-3.631920704	90	1990	49990	2.7953E-05	-2.182277584	0.180374071	-3.250032005
Gravel	90	1490	49990	0.005321171	-3.06535474	2.021730096	-3.626412444	90	1490	49990	4.42177E-07	-1.110201189	26.87692801	-3.345519106
UW Rock	90	1990	49990	3.19032E-06	-1.82119402	0.000314676	-2.281772355	90	2990	49990	3.24637E-05	-1.60966606	15.60659223	-3.17682373
UW Rock	90	5990	49990	2.38914E-07	-1.105568007	2.199506076	-2.844182062	90	6990	49990	8.11765E-05	-2.009643155	83612.02514	-4.087866548
UW Rock	110	4990	49990	6.3928E-07	-1.520106254	0.157110212	-2.880767449	90	5990	49990	3.13099E-05	-1.252834054	0.960371182	-2.31657896
UW Rock	140	3990	49990	8.27751E-07	-1.303171743	0.724323707	-2.710432865	140	2990	49990	4.27445E-06	-1.761051549	0.002171533	-2.306518695

| | 2-Dimensional Spectrum | | | | | | | | | | | | | |
| | X-Cross Section | | | | | | | Y-Cross Section | | | | | | |
Surface Type	Frequency 1	Frequency 2	Frequency 3	Section 1 - Phi	Section 1 - Gamma	Section 2 - Phi	Section 2- Gamma	Frequency 1	Frequency 2	Frequency 3	Section 1 - Phi	Section 1 - Gamma	Section 2 - Phi	Section 2- Gamma
Algae	90	990	49990	2.75065E-09	-1.173771507	27.88610627	-4.333163226	90	1190	49990	8.0832E-07	-1.986159284	51.12050718	-4.396815149
Algae	70	1090	49990	2.61369E-05	-3.384010518	0.176820198	-4.466309918	90	1090	49990	0.00022086	-3.722973068	0.060621809	-4.352862557
Algae	90	1090	49990	1.04709E-06	-2.637864307	3.076198478	-4.633819502	70	1190	49990	5.76231E-06	-2.888307351	0.608742177	-4.433828629
Algae	90	1090	49990	3.01121E-06	-2.273945533	39.43356599	-4.439558692	90	1190	49990	1.86255E-08	-1.565679621	0.149558827	-3.792726138
Algae	90	1990	49990	4.89121E-05	-2.82744805	51.88199919	-4.555870718	110	1890	49990	6.6576E-08	-1.906401213	6.376858272	-4.34027256
Algae	90	1490	49990	2.18456E-08	-1.317521395	263.1568462	-4.35433513	110	1490	49990	1.0858E-07	-1.550619953	202.0920005	-4.319429503
Algae	70	1190	49990	5.98765E-05	-3.248304719	2.207461834	-4.461025258	110	1490	49990	5.45578E-06	-2.919758968	0.252976943	-4.2224339
Algae	70	1990	49990	8.99218E-06	-3.286788071	0.522428983	-4.637820726	140	1490	49990	2.673E-08	-2.447809881	0.001613689	-3.983104547
Algae	110	1090	49990	0.000133681	-2.964915181	6.898099161	-4.365416825	90	990	49990	1.52603E-05	-2.599486469	17.75803722	-4.512713617
Algae	140	1990	49990	9.34099E-09	-2.158432157	0.159652564	-4.302583122	110	2990	49990	1.25488E-07	-2.532264427	5.74610446	-4.702101274
Anemone	140	1990	49990	3.1198E-07	-1.750275251	747.6392027	-4.469727116	140	1990	49990	2.59257E-07	-1.707246488	375.848322	-4.408021379
Anemone	140	2490	49990	3.49909E-07	-2.382869355	0.377495666	-4.185585207	140	2490	49990	7.55441E-05	-3.124193623	4.968660262	-4.496082435
Anemone	110	1090	49990	2.8105E-07	-2.113128459	16.49466236	-4.420859116	140	1990	49990	2.19027E-07	-2.034262262	8.21894943	-4.351161732
Anemone	40	1090	49990	2.43295E-06	-2.891699531	0.061105028	-4.181692885	70	1090	49990	0.000500387	-3.71311238	0.247138313	-4.332403777
Anemone	70	1090	49990	1.71465E-06	-2.32755	22.83713311	-4.410735892	70	1190	49990	1.92178E-07	-2.101246253	1.830182522	-4.139335108
Anemone	110	1490	49990	4.50574E-10	-1.453586316	1.932334565	-4.453866782	110	1990	49990	8.6849E-07	-2.493647484	0.071563745	-4.076791241
Anemone	90	1990	49990	2.50169E-07	-2.625728845	5.838476772	-4.718448303	90	1990	49990	9.09261E-09	-2.203023153	0.422735994	-4.415550812
Anemone	110	1090	49990	4.24091E-10	-1.292598328	16.64160305	-4.52866396	70	4990	49990	1.89962E-05	-2.833168761	313.4701355	-4.819687675
Anemone	70	1090	49990	5.52621E-08	-2.025631061	7.393806662	-4.422433057	110	1090	49990	9.45847E-06	-2.691438962	11.44795177	-4.463802876
Anemone	110	1490	49990	1.70743E-08	-2.341342468	1.340581359	-4.605910965	90	1090	49990	0.001481621	-3.938337392	0.083881078	-4.328073396
Anemone	90	1190	49990	4.90796E-08	-2.025791327	5.868380874	-4.362742416	90	1490	49990	6.624E-06	-2.6067938	2.437554198	-4.281280805
Anemone	90	1190	49990	5.79958E-08	-1.843288751	6.15675268	-4.268358647	110	1490	49990	7.88661E-07	-2.209575023	45.10244288	-4.491715257
Barnacles	90	1990	49990	5.65559E-06	-3.421030393	0.007584584	-3.877818587	90	1990	49990	4.96038E-06	-2.985892321	0.006674326	-3.829166988
Barnacles	90	6990	49990	6.54197E-10	-1.994217874	0.510188013	-4.329850014	90	6990	49990	6.66016E-06	-3.06991219	0.332260767	-4.298917694
Barnacles	140	1990	49990	0.00269638	-4.546826438	0.010303953	-4.667999323	110	1990	49990	0.000400505	-4.260945526	0.179074084	-4.961543922
Barnacles	110	5990	49990	4.40373E-09	-2.317331633	0.215379713	-4.233880603	140	5990	49990	2.3004E-07	-2.666651987	0.746993769	-4.356041817
Barnacles	90	1090	49990	0.000436012	-4.152068293	0.001111066	-3.649356864	110	4990	49990	1.76288E-05	-3.163161136	0.15606631	-4.126162635
Barnacles	140	1490	49990	0.03840492	-5.05493809	0.000537433	-4.275123475	110	1490	49990	0.015003454	-4.79413388	0.000606097	-4.234434011
Barnacles	90	2990	49990	2.60759E-09	-1.925035688	0.431846081	-4.133896819	110	4990	49990	3.47218E-06	-2.72948691	0.391222244	-4.119250582
Barnacles	110	1190	49990	0.051431776	-4.889949935	0.004007485	-3.950382428	110	4990	49990	3.16986E-07	-2.819017271	8.87962989	-4.702076282
Barnacles	110	1990	49990	0.001121115	-4.404936673	0.000240409	-4.013699961	110	1190	49990	0.018582298	-4.796642624	0.000484722	-4.11971994
Barnacles	140	1090	49990	0.085958493	-5.122686477	0.000167	-3.782858077	90	1490	49990	0.000274764	-3.928587562	0.000127049	-3.752362797
Grass	110	1090	49990	0.000209228	-3.963947504	0.019917839	-4.365135289	110	1490	49990	5.29739E-06	-3.424015608	0.006676967	-4.263561295
Grass	90	1990	49990	7.33275E-07	-2.498071217	9.17320845	-4.632480454	90	1490	49990	1.23432E-08	-1.916704367	0.162958991	-4.187321381
Grass	110	1490	49990	1.12645E-06	-2.118504152	54.93677217	-4.364119518	110	1490	49990	3.34478E-08	-1.54202843	169.6955821	-4.48507956
Grass	110	1190	49990	1.32287E-06	-2.310817481	21.62047073	-4.393096423	110	1490	49990	2.15389E-07	-2.079530609	16.39021579	-4.355684772
Grass	90	990	49990	6.8992E-05	-3.710471587	0.0389315	-4.389655378	110	1090	49990	2.7038E-07	-2.81261077	0.301815826	-4.580385953
Grass	110	1190	49990	1.44568E-06	-2.501810342	0.338342355	-4.116674372	90	1190	49990	1.32332E-07	-2.22799953	13.00769479	-4.509653624
Grass	110	1090	49990	1.63855E-05	-3.383735858	0.038864494	-4.337551599	110	1090	49990	2.43012E-07	-2.816759808	0.26258616	-4.556736251
Grass	90	1990	49990	3.84242E-07	-2.134452689	4.417873484	-4.064655358	110	2990	49990	8.45664E-07	-2.223581657	33.5934599	-4.281352624
Grass	110	4990	49990	8.30388E-08	-1.793653105	48.63290962	-4.184198644	140	3990	49990	2.03386E-07	-1.857386034	73.79834711	-4.243754193
Grass	110	1990	49990	1.3151E-06	-2.844527464	0.13067039	-4.173804031	110	1990	49990	1.58929E-05	-3.167978989	0.175328737	-4.208634695
Moderate Rock	90	890	49990	2.21219E-08	-1.615893198	42.88053518	-4.649155761	90	990	49990	3.77582E-06	-2.530033234	8.690611924	-4.475990501
Moderate Rock	70	890	49990	5.03264E-07	-2.510120872	1.019082351	-4.529183568	90	1090	49990	3.57983E-09	-1.839738062	1.027581861	-4.531165697
Moderate Rock	70	890	49990	0.000254553	-3.659883709	0.257020905	-4.476202123	90	990	49990	9.58559E-07	-2.936960777	0.364182065	-4.555890978
Moderate Rock	70	790	49990	1.95399E-07	-2.357151484	1.298541183	-4.535357303	70	890	49990	1.99596E-05	-3.067205643	0.388323832	-4.425964691
Moderate Rock	90	890	49990	7.47393E-07	-2.860715781	0.005407046	-4.18407014	110	890	49990	1.70693E-07	-2.764208473	0.074752192	-4.453029987
Moderate Rock	90	990	49990	0.001695626	-4.189903314	0.016758269	-4.358746379	90	1090	49990	0.000134031	-3.874529036	0.140277779	-4.648568513
Moderate Rock	90	990	49990	1.80845E-06	-2.87793886	0.02543343	-4.225768294	90	1090	49990	1.17525E-05	-3.301295245	0.293752236	-4.502632193
Moderate Rock	90	1090	49990	3.66172E-08	-2.326084942	0.286852586	-4.554492284	90	1090	49990	1.64728E-05	-3.299149393	0.01588305	-4.217334925
Moderate Rock	90	1190	49990	4.19818E-09	-1.886656632	7.082605192	-4.786980954	90	1190	49990	1.04061E-06	-2.802814928	6.223257734	-4.764629785
Moderate Rock	90	890	49990	1.47812E-05	-3.288972545	0.23557667	-4.552484644	140	990	49990	8.67007E-07	-2.920588672	0.593622463	-4.663387999
Moderate Rock	90	990	49990	3.69329E-05	-3.368912887	1.353728892	-4.651874227	90	1090	49990	4.6166E-06	-3.082715538	1.537865251	-4.668195176
Mussels	140	4990	49990	1.08378E-08	-1.906150329	1.836298726	-4.177563834	140	4990	49990	1.05262E-08	-1.921890857	3.902974526	-4.265351858
Mussels	110	1990	49990	1.99621E-05	-3.110561504	0.176825141	-4.023729448	110	2990	49990	8.32876E-07	-2.590303567	1.470823868	-4.245474439
Mussels	110	4990	49990	3.60093E-07	-2.212449916	9.162176289	-4.222774902	110	3990	49990	6.59876E-07	-2.313121296	14.43745726	-4.278081009
Mussels	110	4990	49990	1.70857E-08	-1.89018933	8.096920574	-4.263669063	110	4990	49990	3.28568E-07	-2.292437722	3.284634711	-4.190239387
Mussels	90	1090	49990	3.55034E-05	-2.941571047	0.151028578	-3.873820218	110	1990	49990	5.15611E-08	-2.070195015	1.274894122	-4.091123061
Mussels	90	1190	49990	1.23959E-06	-2.301968789	2.284037431	-4.02591418	90	990	49990	4.74604E-05	-2.817675494	2.322193872	-4.02371961
Mussels	90	1990	49990	5.47011E-08	-2.091640019	2.165706085	-4.250230982	140	3990	49990	5.11133E-07	-2.39823181	28.05958043	-4.502813622
Mussels	110	990	49990	6.06259E-05	-3.401826198	0.006184096	-3.772414284	90	890	49990	0.004044362	-4.005092253	0.019523926	-3.89613427
Mussels	90	1090	49990	5.28189E-06	-2.943183425	0.070927499	-4.134136966	110	1490	49990	1.46331E-05	-3.119575937	0.253953089	-4.257711976
Mussels	90	1090	49990	0.000422906	-3.575277384	0.079154434	-4.106087457	90	1090	49990	3.21152E-07	-3.211520849	0.045044017	-4.042593689
Kelp	190	4990	49990	1.22556E-08	-1.570400147	23.19672224	-4.132452691	140	3990	49990	6.94102E-07	-2.099761419	46.89269137	-4.217682498
Kelp	140	2990	49990	1.34455E-07	-2.058665574	5.426541591	-4.145527321	140	3990	49990	5.79693E-06	-2.525272908	15.36526967	-4.270176451
Kelp	140	4990	49990	7.60569E-09	-1.77984081	7.721956618	-4.244450548	140	4990	49990	1.50561E-07	-2.153118923	1.750912153	-4.114492762
Kelp	110	1990	49990	2.19061E-06	-2.42911422	2.112608582	-3.986358937	110	1990	49990	5.85329E-06	-2.538997589	4.348870016	-4.091237935
Kelp	290	2990	49990	6.94416E-09	-1.723137895	1.603516826	-4.08021208	290	2490	49990	5.59706E-09	-1.687353828	3.015543062	-4.155270285
Kelp	190	4990	49990	8.81654E-07	-1.803162071	1194.740178	-4.276404997	110	3990	49990	1.41786E-06	-1.847592823	1350.813523	-4.296825759
Kelp	110	4990	49990	4.81716E-07	-1.988503702	11.52935768	-4.015514764	110	3990	49990	9.06446E-07	-2.064136673	175.2291011	-4.301851065
Kelp	110	3990	49990	1.68898E-06	-2.150716683	17.05087262	-4.062109383	110	3990	49990	1.66612E-07	-1.845564926	186.1769596	-4.32159504
Kelp	190	1990	49990	1.01601E-06	-2.10149832	20.12533056	-4.094058745	290	4990	49990	8.3668E-08	-1.767338361	117.2506034	-4.274567219
Kelp	110	3990	49990	2.73616E-07	-1.815719984	414.4348083	-4.283191502	140	4990	49990	5.97634E-07	-1.925072601	563.3166912	-4.333498101
Urchin	90	1990	49990	6.61943E-07	-2.705658568	0.620243247	-4.386461995	110	1990	49990	1.40461E-06	-2.833906256	0.623053734	-4.378431129
Urchin	140	1990	49990	4.37607E-08	-1.855263811	25.45875941	-4.452716207	140	1990	49990	5.1682E-09	-1.560279936	15.71057838	-4.396822104
Urchin	110	1190	49990	9.69128E-08	-1.893328885	4.479214812	-4.17068213	90	1490	49990	3.9226E-07	-2.082677789	9.459691977	-4.252171428
Urchin	110	1190	49990	9.27044E-06	-2.411843179	33.82834809	-4.216265757	110	1490	49990	1.76889E-07	-1.847428316	23.65626948	-4.186716025
Urchin	110	1490	49990	1.24355E-07	-1.828437395	15.17430101	-4.240641152	90	1490	49990	3.52671E-09	-1.322799835	26.28961418	-4.304912483
Urchin	140	1990	49990	5.12873E-08	-1.815531477	16.32658847	-4.334231611	140	2990	49990	3.67639E-08	-1.855782368	48.47912773	-4.477548133
Urchin	140	4990	49990	1.12998E-07	-1.992116421	12.28266264	-4.269629699	110	4990	49990	7.684E-07	-2.253497977	12.25238624	-4.285473239
Urchin	90	1990	49990	2.21019E-06	-2.276268754	10.42350415	-4.22890357	90	2990	49990	2.64657E-07	-1.984529102	41.14351596	-4.386516146
Urchin	110	1990	49990	1.6853E-06	-2.060047281	71.06170161	-4.282096909	110	1990	49990	2.04477E-08	-1.426284603	109.6647648	-4.329510025
Urchin	140	1990	49990	4.39776E-07	-2.469667809	1.151941751	-4.262294131	90	1990	49990	6.28274E-07	-2.491294322	0.03033079	-3.856186234
Smooth Rock	110	1990	49990	3.8202E-07	-2.766076774	0.705626972	-4.509238717	110	2990	49990	1.45686E-08	-2.296845992	0.337991734	-4.429887767
Smooth Rock	110	1490	49990	5.97777E-08	-1.915078358	74.78768384	-4.501216211	90	2990	49990	9.1146E-11	-0.932751817	1612.3787	-4.786463957
Smooth Rock	110	1490	49990	5.24223E-08	-2.258983442	0.752206935	-4.354612184	110	1990	49990	9.89365E-09	-2.002711789	0.548860372	-4.323437393
Smooth Rock	90	2990	49990	2.21547E-07	-2.406789388	1.802520833	-4.408022576	90	1990	49990	1.51209E-08	-2.004280343	0.85894339	-4.330217371
Smooth Rock	140	2990	49990	2.54156E-07	-2.483214295	3.112666634	-4.504946366	140	3990	49990	1.58475E-08	-2.134542436	1.094162728	-4.371026166
Smooth Rock	110	1190	49990	4.08269E-07	-2.557756314	0.649468495	-4.352057187	90	1190	49990	8.67068E-08	-2.339316976	0.393104089	-4.295730416
Smooth Rock	70	1990	49990	1.38621E-05	-3.576368358	0.102335645	-4.732796066	90	1490	49990	0.000259137	-4.020950648	0.000682341	-4.090127701
Smooth Rock	90	990	49990	1.82387E-05	-3.615728065	0.015262774	-4.499937388	90	990	49990	0.000108899	-3.886948236	0.001217498	-4.152292581
Smooth Rock	90	1190	49990	6.81062E-06	-3.362103188	0.010812718	-4.311920217	90	1490	49990	6.40472E-06	-3.306673752	0.057009974	-4.505342367
Smooth Rock	90	890	49990	0.001054396	-4.399288677	0.009648499	-4.606881905	90	890	49990	2.96784E-05	-3.972298314	0.000859097	-4.341280253
Gravel	90	3990	49990	1.40098E-06	-2.814332135	0.07414541	-4.043471489	90	3990	49990	2.50082E-06	-2.881324252	0.551893475	-4.266615615
Gravel	90	4990	49990	1.1615E-07	-2.309698097	0.548982364	-4.146851546	90	4990	49990	6.5067E-07	-2.514017136	1.1575825	-4.230021344
Gravel	90	2990	49990	1.33362E-07	-2.219296495	0.789516075	-4.080813798	90	2990	49990	1.8484E-07	-2.247298867	2.230621707	-4.196221144
Gravel	110	4990	49990	7.89636E-07	-2.509162612	1.458611604	-4.233794304	110	3990	49990	7.0100E-08	-2.109500439	5.345019345	-4.357614533
Gravel	110	3990	49990	8.4676E-07	-2.603475264	1.612301976	-4.291478041	110	3990	49990	1.78238E-08	-2.015672842	6.015696242	-4.412645291
Gravel	110	1190	49990	9.96427E-08	-2.493391673	0.013160133	-3.912831443	140	4990	49990	2.29575E-07	-2.60044756	0.528735983	-4.291362609
Gravel	140	3990	49990	6.86325E-09	-1.966132758	1.081580751	-4.251662254	140	3990	49990	1.04869E-08	-2.05715193	2.303534965	-4.346993282
Gravel	90	1990	49990	1.67769E-05	-3.16970116	0.10036179	-3.963495259	90	3990	49990	4.01304E-08	-2.267031278	0.55638159	-4.132806304
Gravel	110	4990	49990	1.77254E-08	-2.094335247	2.314135986	-4.285649029	110	2990	49990	5.1935E-08	-2.208559843	0.397250589	-4.089169148
Gravel	90	2990	49990	8.52056E-07	-2.459583601	0.89703426	-4.161752628	90	3490	49990	7.19169E-08	-2.046976401	23.01575915	-4.487759971
UW Rock	110	6990	49990	3.02882E-09	-1.719486383	0.239043754	-3.735332125	110	9990	49990	3.03087E-09	-2.390770308	1.02810862	-3.880034956
UW Rock	90	6990	49990	1.32619E-08	-1.970581327	0.399649385	-3.821594854	110	6990	49990	6.43842E-07	-2.477285934	0.068390132	-3.653730057
UW Rock	110	9990	49990	5.32203E-09	-1.436993461	3.111243929	-3.526626504	90	14990	49990	8.47721E-06	-2.232665378	4.073773735	-3.557479647
UW Rock	110	9990	49990	5.00641E-08	-1.988628991	0.541864604	-3.625894007	110	14990	49990	3.32554E-08	-1.931942488	0.355561445	-3.592155734

Surface Type	P-Welch Fractal Dimensions				2-D Fractal Dimensions				Multi-Taper Fractal Dimensions			
	X-Direction: Section 1	X-Direction: Section 2	Y-Direction: Section 1	Y-Direction: Section 2	X-Direction: Section 1	X-Direction: Section 2	Y-Direction: Section 1	Y-Direction: Section 2	X-Direction: Section 1	X-Direction: Section 2	Y-Direction: Section 1	Y-Direction: Section 2
Algae	2.602496437	1.232691971	2.789664681	1.100907738	2.413114247	0.833418387	2.006920358	2.006920358	2.626597905	1.136266247	2.50677506	1.107941268
Algae	1.908253127	1.558515473	1.872690198	1.362245564	1.307994741	0.766845041	1.138513466	1.138513466	1.794992451	1.418219025	1.831092262	1.422161432
Algae	1.937436842	1.28231109	1.913753017	1.020260787	1.681067847	0.683090249	1.555846325	1.555846325	2.056325777	1.104579327	1.855076299	1.084071191
Algae	2.558739388	1.453148724	2.676640472	1.023750253	1.863027234	0.780220654	2.21716019	2.21716019	2.538162439	1.103290268	2.628375022	1.10021815
Algae	2.427075461	1.283741804	2.383362374	1.165946231	1.586275975	0.722064641	2.046799393	2.046799393	2.671614934	1.02544743	1.616615391	1.004907066
Algae	2.596347637	1.439467428	2.313297818	1.175167305	2.341239303	0.822832435	2.224690024	2.224690024	2.7032063	0.894134656	2.616803756	0.894134656
Algae	2.151807825	1.298317118	2.533425356	1.144417958	1.37584764	0.769487371	1.540120516	1.540120516	1.947050355	1.059576532	2.082762241	1.060170576
Algae	1.816396389	1.492526105	1.589854434	1.466877389	1.356605965	0.681089637	1.77609506	1.77609506	1.617535083	0.872677526	1.476306603	0.872677526
Algae	2.197464879	1.138189419	2.089434363	1.088910267	1.51754241	0.817291587	1.700256765	1.700256765	2.311245354	1.16987091	1.997289653	1.151861142
Algae	1.71475282	1.395365888	2.332085334	1.209627141	1.920783921	0.848708439	1.733867786	1.733867786	1.328191132	1.198339667	2.346182684	0.63546195
Anemone	2.90912826	1.292346294	2.907615929	1.45085076	2.124862374	0.765136442	2.146376756	2.146376756	2.725018579	1.511522814	2.859271976	1.513196057
Anemone	2.412027376	1.13931449	1.927840346	1.188440349	1.808565322	0.907207397	1.437903188	1.437903188	2.447208201	1.220409852	1.532987665	1.172944854
Anemone	2.68720854	1.372712529	2.67181782	1.118541702	1.94343577	0.789570442	1.982868869	1.982868869	2.571374734	1.146791761	2.454057831	1.147311684
Anemone	1.460051076	1.476162935	2.727881901	1.121654917	1.554150234	0.909153557	1.14344381	1.14344381	1.723604242	1.111880981	2.558347644	1.11437923
Anemone	2.608303305	1.17505345	2.425403242	1.39631595	1.836225	0.794632054	1.949376873	1.949376873	2.331074573	0.965956921	2.564914794	0.953133797
Anemone	2.445122733	1.225993232	2.760742059	1.164632938	2.273206842	0.773066609	1.753176258	1.753176258	2.455916942	1.242859622	2.345393293	1.247017007
Anemone	2.483585192	1.17534201	2.256395992	1.687876318	1.687135577	0.640775849	1.898488424	1.898488424	2.281205251	1.630850487	2.124476525	1.630850487
Anemone	2.208007323	1.063808276	2.309202019	1.153468789	2.353700836	0.73566802	1.58341562	1.58341562	2.254929261	0.925358716	2.283077368	0.89268148
Anemone	1.673643976	1.139840188	2.363104085	1.307744582	1.987184469	0.788783471	1.654280519	1.654280519	1.624595226	1.26195499	2.467478957	1.26195499
Anemone	1.673912396	1.234625788	1.659023811	1.326731615	1.829328766	0.697044518	1.030831304	1.030831304	1.345667836	0.681500279	1.400906937	0.673078029
Anemone	2.344791822	1.485266666	2.423118567	1.450642447	1.987104336	0.818628792	1.6966031	1.6966031	2.192032095	1.522882721	2.226587954	1.503760892
Anemone	2.636481184	1.227842266	2.201491111	1.434193342	2.078355625	0.865820676	1.895212489	1.895212489	2.599807024	1.41325421	2.121833953	1.41325421
Barnacles	1.610108138	1.920526467	1.153444515	1.168383517	1.289484804	1.061090706	1.50705384	1.50705384	1.77626294	1.010113162	1.213470218	1.028308948
Barnacles	0.985445098	1.058238539	2.444614227	1.046265935	2.002891063	0.835074993	1.465043905	1.465043905	2.194212682	1.121627171	2.433338015	1.100621545
Barnacles	1.287234609	1.023501437	1.143423167	1.136346653	0.726586781	0.666000339	0.869527237	0.869527237	1.357676372	0.998317169	0.929822311	0.988556391
Barnacles	0.980339318	1.099453028	1.540695429	1.371655281	1.841334183	0.883059699	1.666674006	1.666674006	1.104194694	1.366177054	1.421785593	1.334742975
Barnacles	1.210786798	1.58632436	1.178111912	1.480649092	0.923965854	1.175321568	1.418419432	1.418419432	1.020661692	1.388264332	1.084973816	1.339817183
Barnacles	1.415042335	1.090739884	1.209995111	1.066590961	0.472530955	0.862438262	0.60293306	0.60293306	1.254591165	0.959837584	1.272793331	0.961550582
Barnacles	1.504032248	1.269614012	1.919575416	0.925989352	2.037482156	0.933051591	1.635256545	1.635256545	1.690375032	0.861014088	1.832622466	0.895062101
Barnacles	1.571887216	0.889616504	1.730728644	0.996414092	0.555025032	1.024808786	1.590491364	1.590491364	1.34974048	0.752563363	1.536748094	0.787484691
Barnacles	1.598938371	1.281607015	1.283298345	1.057321733	0.797531663	0.993150019	0.601678688	0.601678688	1.154358753	0.962749366	0.987855657	0.923858209
Barnacles	1.109106163	1.049093154	1.515098033	1.269517727	0.438656761	1.108570962	1.035706219	1.035706219	1.367095165	0.659882713	1.487896438	0.659882713
Grass	1.525271331	1.4137669	1.533691746	0.076609697	1.018026248	0.817432355	1.287992196	1.287992196	1.78441333	1.012798738	1.765884083	1.012798738
Grass	1.54154151	1.357193456	1.783745297	1.257472217	1.750964392	0.683759773	2.041647817	2.041647817	1.78517802	1.664072718	1.635263208	1.664072718
Grass	2.449032605	1.885470954	2.736449013	1.225934187	1.940747924	0.817940241	2.228985785	2.228985785	2.400650389	1.047164336	2.626487035	1.095052761
Grass	2.569562296	1.141802829	2.638345763	1.183457996	1.844591259	0.803451788	1.960234696	1.960234696	2.53084501	0.435851564	2.593900848	0.475057555
Grass	1.53815042	1.67015286	2.164524792	1.043483912	1.144764207	0.805172311	1.593694615	1.593694615	1.738171174	0.952629433	2.087414332	0.933484302
Grass	2.192959589	1.677806966	1.906690627	1.121859062	1.749094829	0.941662814	1.886000235	1.886000235	2.055632645	0.473378426	2.019224107	0.427500046
Grass	1.932121834	1.294608644	1.59443851	1.392838512	1.308132071	0.831224201	1.591620096	1.591620096	1.882903211	1.264180776	1.895288612	1.264180776
Grass	2.521716343	1.302894523	2.010215638	1.525375458	1.932773655	0.967672321	1.888209171	1.888209171	2.389990698	1.463036567	2.31748761	1.468334528
Grass	2.534761802	1.244051324	2.47183363	1.47553855	2.103173447	0.907900678	2.071306983	2.071306983	2.306908684	1.499062673	2.503259322	1.499062673
Grass	1.963456646	1.610668591	1.517090669	1.260469079	1.577736268	0.913097984	1.416010505	1.416010505	2.204029857	1.023133877	1.976637047	1.033219852
Moderate Rock	2.371697025	1.068485033	2.227247293	1.213420214	2.192053401	0.675422119	1.734983383	1.734983383	2.4072164	0.908024009	2.559572633	0.931087712
Moderate Rock	2.581039957	1.194954268	2.125517887	1.614120856	1.744939564	0.735408216	2.080130969	2.080130969	2.406081918	1.598850203	1.919268633	1.599291894
Moderate Rock	1.508118958	1.158784817	1.772868711	1.805236463	1.170058146	0.761898939	1.531519612	1.531519612	1.579013379	1.691408565	1.651655189	1.691408565
Moderate Rock	1.83111193	1.04533484	2.356820032	1.627285381	1.821424258	0.732321348	1.466397179	1.466397179	1.780454535	1.583342451	2.358431564	1.556828654
Moderate Rock	1.723607514	1.142629146	2.676934801	1.110236851	1.56964211	0.90796493	1.617895764	1.617895764	1.770819413	1.017829722	2.770647363	1.064417977
Moderate Rock	2.119447783	0.84880154	1.527358317	1.094205082	0.905048343	0.82062681	1.062735482	1.062735482	1.896032249	0.61057491	2.090219517	0.607091134
Moderate Rock	1.372548455	1.00363753	2.24137132	1.251513896	1.56103057	0.887115853	1.349352377	1.349352377	1.371800982	1.197941835	2.312049658	1.209514755
Moderate Rock	2.053150487	1.086243867	1.531914628	1.653689671	1.836957529	0.722753858	1.350425304	1.350425304	1.83785332	1.654392591	1.821568607	1.591404414
Moderate Rock	2.262988702	1.069644572	2.11387601	1.175607263	2.056671684	0.606509523	1.598592536	1.598592536	2.421737786	1.182588899	2.04779701	1.182588899
Moderate Rock	2.072601572	1.028701344	1.895595974	1.060498729	1.355513728	0.723757678	1.539705664	1.539705664	1.887273003	0.839680313	2.032265147	0.838660644
Moderate Rock	2.056690037	1.487468417	1.956534152	1.109284614	1.315543556	0.674062887	1.458642231	1.458642231	1.831662716	0.923852347	1.891077495	0.849650486
Mussels	2.130398212	1.357812381	2.31107405	1.306325756	2.046924836	0.911218083	2.039054572	2.039054572	2.36827868	1.241471542	2.461527824	1.266066502
Mussels	2.091581637	1.454018662	1.331840642	1.48394795	1.444719248	0.988135276	1.704848217	1.704848217	2.181383835	1.304283973	1.499927996	1.340477858
Mussels	2.400457943	0.972303163	2.270345478	1.499660929	1.893775042	0.888612549	1.843439352	1.843439352	2.373333551	1.434493589	2.199524529	1.502188998
Mussels	2.745300793	1.600212879	2.24995494	1.318040792	2.054905335	0.868165469	1.853781139	1.853781139	2.698799337	1.15253155	2.17775298	1.039150026
Mussels	2.12168412	1.565051612	2.090023963	1.358614315	1.529214476	1.063089891	1.964902492	1.964902492	1.887819796	1.379662536	2.457819757	1.327425484
Mussels	2.410557783	1.106148035	2.461462353	1.375147312	1.849015606	0.98704291	1.591162253	1.591162253	2.772770502	1.440621321	2.423834933	1.440621321
Mussels	1.761099144	1.482535389	1.355810427	1.313931054	1.299086901	1.113792858	0.997453874	0.997453874	2.03183315	1.173624441	1.717633702	1.125879341
Mussels	1.08252368	1.332015793	1.554112626	1.119062457	1.528408288	0.933931517	1.440212032	1.440212032	2.025962221	1.028185073	1.695307642	1.007330085
Mussels	1.163864662	1.368581191	1.685497563	1.072828567	1.212361308	0.946956272	1.394239575	1.394239575	1.95304924	0.970466691	1.913484445	0.938235967
Kelp	2.349177867	1.524972893	2.342003566	1.45136034	2.214799926	0.933773654	1.950119291	1.950119291	2.243664225	1.554443986	2.450595543	1.494611591
Kelp	2.461005399	1.211746521	2.304307484	1.290239782	1.970667213	0.927236339	1.737363546	1.737363546	2.360779262	0.964580198	2.517651171	0.964580198
Kelp	2.250774377	1.087181899	2.242041956	1.385783008	2.110079995	0.877774726	1.923440538	1.923440538	2.491727759	1.202256635	2.269404222	1.225205299
Kelp	2.427073038	1.622590143	2.292665506	1.57705770	1.78544289	1.006820531	1.730501206	1.730501206	2.477820211	1.553963977	1.970388861	1.594769684
Kelp	2.823443993	1.330497707	2.258140899	1.271348101	2.138431052	0.95989396	2.156323086	2.156323086	2.552645644	1.293810159	2.276172742	1.293810159
Kelp	2.695574905	1.359969086	2.668562555	1.392510545	2.098418965	0.861797501	2.076203589	2.076203589	2.725392041	1.480593523	2.538772329	1.480593523
Kelp	2.50261725	1.432290865	2.213378475	1.167842834	2.005748149	0.992242618	1.967931664	1.967931664	2.491947361	1.041265246	2.366654964	1.041265246
Kelp	2.481520435	1.308669501	2.401402981	1.35169496	1.924641659	0.968945309	2.077217537	2.077217537	2.422856694	1.289819547	2.545568613	1.289819547
Kelp	2.712525802	1.560647707	2.44027999	1.408423477	1.94925084	0.952970627	2.116330819	2.116330819	2.534528077	1.450968162	2.411582164	1.423692049
Kelp	2.404600556	1.305105475	2.764232112	1.39032915	2.092140008	0.858404249	2.037463699	2.037463699	2.340172169	1.302410414	2.644448638	1.433137563
Urchin	1.215990146	1.044298555	1.708744572	1.144002851	1.647170716	0.806769002	1.583046872	1.583046872	2.242986869	1.07825933	1.653365799	1.057307023
Urchin	2.357046323	1.604521393	2.662380317	1.163202887	2.072368095	0.773641896	2.219860032	2.219860032	2.149135876	0.966695492	2.791751311	1.023616479
Urchin	2.573237086	1.544994033	2.431264287	1.411355624	2.053335558	0.914658935	1.958661105	1.958661105	2.626716731	1.486168568	2.403491572	1.503067371
Urchin	2.657492485	1.223454369	2.455446063	1.048427009	1.794078411	0.891867121	2.076285842	2.076285842	2.605880779	0.791607977	2.085214741	0.754115475
Urchin	2.517005292	1.666932133	2.412242954	1.424217663	2.085781303	0.879679424	2.338600083	2.338600083	2.578795976	1.496595184	2.210040692	1.477620443
Urchin	2.558362028	1.201041026	2.846641402	0.664537097	2.092234261	0.832884194	2.072108816	2.072108816	2.667212423	1.127696929	2.682266583	0.737653144
Urchin	2.692778888	1.713760199	2.182543509	1.266506396	2.003941789	0.865185151	1.873251011	1.873251011	2.460893292	0.962141339	2.3479823	0.882044858
Urchin	2.535437571	1.118506181	2.174475227	1.025677336	1.861865623	0.885548215	2.007735449	2.007735449	2.707739564	0.962068712	2.234912508	0.945824123
Urchin	2.362308598	1.566577365	2.809453579	1.537356002	1.969976359	0.858951546	2.286857698	2.286857698	2.404405026	1.409583609	2.616571462	1.41672628
Urchin	2.661136545	1.180896094	1.388052323	1.210460611	1.765166096	0.868852934	1.754352839	1.754352839	2.730421461	1.070224581	1.376960012	1.070224581
Smooth Rock	2.542057909	1.254761042	2.299454065	1.164195933	1.616961613	0.745380642	1.851577004	1.851577004	2.402538627	1.213536049	2.276991749	1.19254101
Smooth Rock	2.062335011	1.136792085	2.085918831	1.03734578	2.042460821	0.749391895	2.533624091	2.533624091	2.198641948	0.836437847	2.08760947	0.855947952
Smooth Rock	2.290767793	1.316181789	2.514880861	1.339616024	1.870508279	0.822693908	1.998644105	1.998644105	2.262404139	1.327385738	2.346330004	1.329475852
Smooth Rock	2.238123281	1.270890935	1.839923439	1.331105971	1.796605306	0.795988712	1.997859828	1.997859828	2.280053857	1.240213713	2.546189626	1.285787957
Smooth Rock	2.534250459	1.241682827	2.443546271	1.249859006	1.758392852	0.747526817	1.932728782	1.932728782	2.51342041	1.289363884	2.430589925	1.273014206
Smooth Rock	2.485048309	1.236143708	2.304388016	1.240871399	1.721121843	0.823971406	1.830341512	1.830341512	2.413155614	1.259227491	2.342118436	1.244157025
Smooth Rock	1.717354606	1.724389405	1.999299057	1.277792901	1.211815821	0.633601967	0.989524676	0.989524676	1.921996824	1.317382288	1.765648955	1.31627389
Smooth Rock	1.579260164	1.055744889	1.852678171	1.096130321	1.192135968	0.750031308	1.056525882	1.056525882	1.775449675	0.814218414	2.002117607	0.808219788
Smooth Rock	1.94451356	1.267364492	1.651303665	1.61876833	1.318948406	0.844039892	1.346663124	1.346663124	1.875188786	1.495973698	1.787358543	1.517881417
Smooth Rock	1.545313734	1.088240024	1.881471408	1.203577598	0.800355661	0.696559047	1.013850843	1.013850843	1.377681059	1.197311076	1.669514101	1.19141296
Gravel	1.481714709	1.421352304	2.20901035	1.430114173	1.592833933	0.978264256	1.559313774	1.559313774	2.152398951	1.244518288	2.400342715	1.244518288
Gravel	1.607543506	1.470130463	1.706287822	1.102877094	1.845150951	0.926574227	1.742991432	1.742991432	1.76298284	1.331059106	1.706176779	1.192726366
Gravel	1.954675337	1.219171544	2.265561127	1.283581895	1.890351753	0.959593101	1.876350567	1.876350567	1.987126787	1.148412525	2.380915058	1.092211112
Gravel	1.321541055	1.216357178	2.275783315	1.252220458	1.745418694	0.883102848	1.945249781	1.945249781	2.274006188	1.249444841	2.181121699	1.262423431
Gravel	1.725810021	1.916404906	2.34502079	1.355240787	1.698262368	0.85426098	1.992163579	1.992163579	1.858797605	1.342199273	1.946897158	1.437249077
Gravel	2.003265854	1.350712742	2.100192089	1.014634138	1.753304163	1.043584278	1.69977622	1.69977622	1.732431143	1.572619191	2.113033114	1.179619901
Gravel	2.166283759	1.448566277	2.052921137	1.34707622	2.016933621	0.874168873	1.971424035	1.971424035	2.076688702	1.214628621	1.911216713	1.183084282
Gravel	1.577495574	2.041063664	2.375243339	1.758453161	1.41514942	1.018252371	1.866484361	1.866484361	1.29587161	1.805474088	2.075407459	1.793205488
Gravel	1.762297401	1.184039648	1.908861208	1.374983997	1.952832376	0.857175486	1.895720079	1.895720079	1.598686891	1.222488241	2.238315369	1.17732736
Gravel	1.46732263	1.186793778	2.444899405	1.327240427	1.7702082	0.919123686	1.976511799	1.976511799	1.58510788	1.203566501	2.749284372	1.138746748
UW Rock	2.08940299	1.859113823	2.19516697	1.411588135	2.140256808	1.132333937	1.804614846	1.804614846	2.149089155	1.37039159	2.143567321	1.352162872
UW Rock	2.447215997	1.577908969	1.995178423	0.956066726	2.014709337	1.089202573	1.761357033	1.761357033	2.279310876	1.365478952	2.010999014	1.050051532
UW Rock	2.239946873	1.559616276	2.373582973	1.84171052	2.28150327	1.236686748	1.883667311	1.883667311	2.147509709	1.742317156	2.4174934	1.798619639
UW Rock	2.348414128	1.644783567	2.119474226	1.846740653	2.005685505	1.187052997	2.034028756	2.034028756	2.503648682	1.529673125	2.421409847	1.529673125

* FD Values above are all based on the 1-D cross sections of the data, specifically γ_1 as discussed in Chapter II.
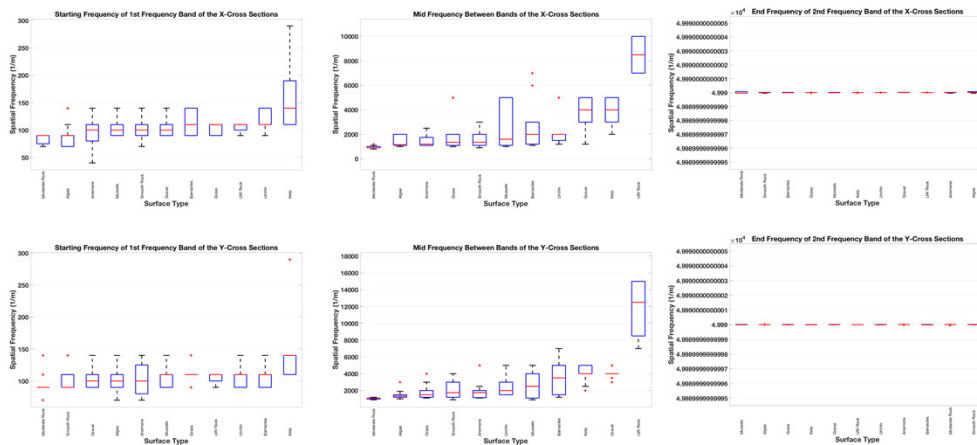
THIS PAGE INTENTIONALLY LEFT BLANK

APPENDIX C: WELCH AND 2-D SPECTRUM DATA PLOTS

All the plots in this appendix are the same format as the plots presented in Chapter III—Results and Discussion but for the spectrums derived from the Welch method and the 2-D Fourier Transform method.
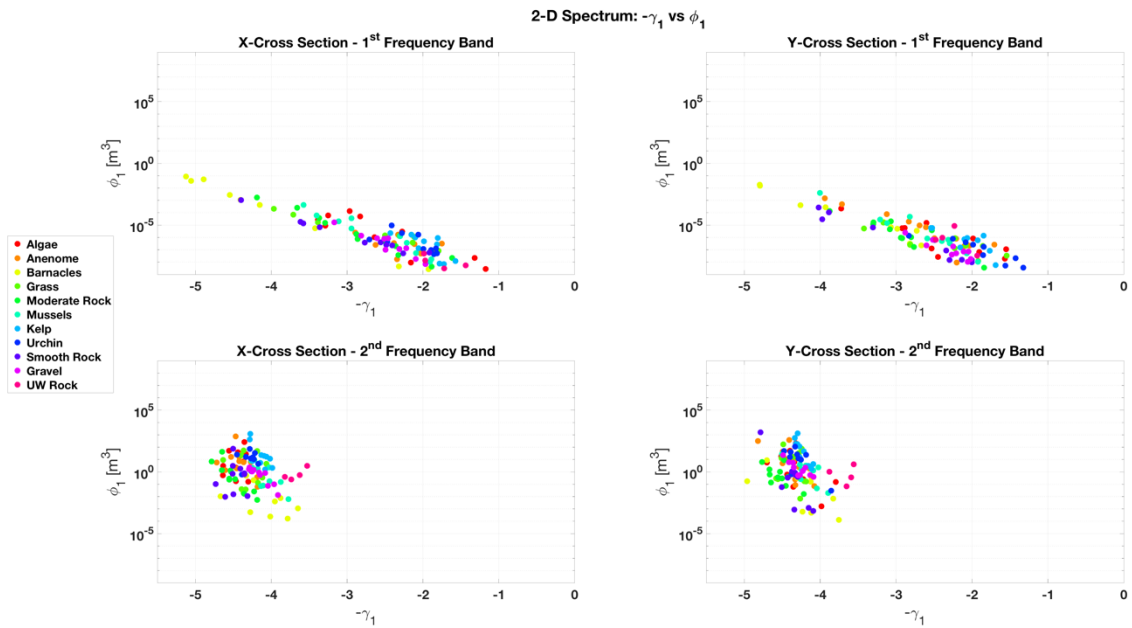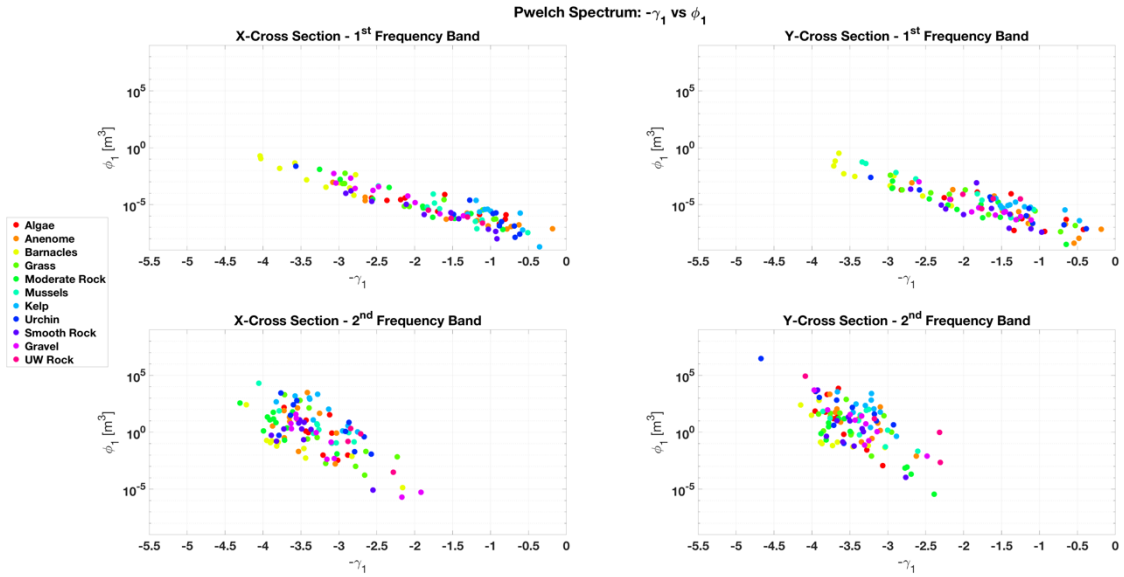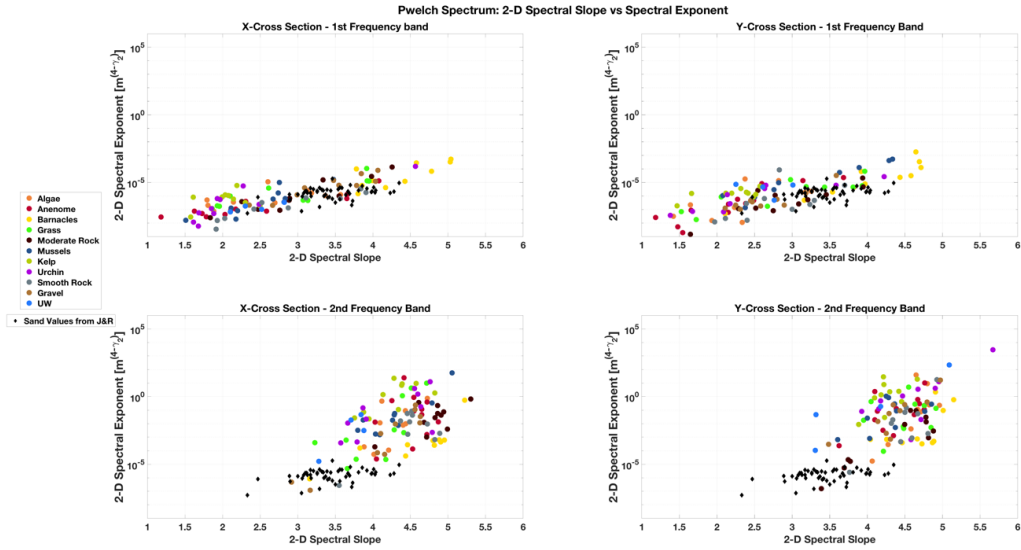
**Frequency Bands**
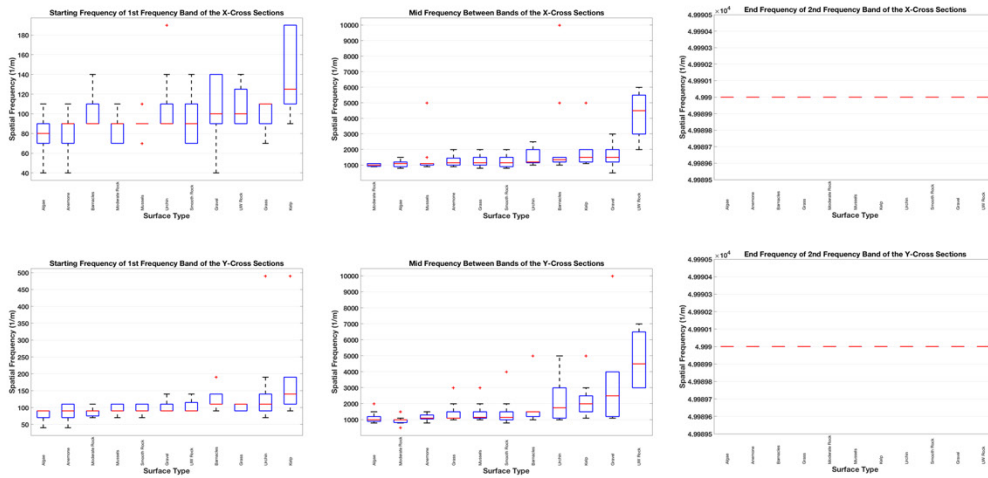
Pwelch Spectrum Frequency Bands

2-D Spectrum Frequency Bands

1-D Spectral Parameters

φ_1 Parameters for 1st Frequency Band: All Spectrums

φ_1 Parameters for 2nd Frequency Band: All Spectrums

-γ₁ Parameters for 1st Frequency Band: All Spectrums

-γ₁ Parameters for 2nd Frequency Band: All Spectrums

-γ₁ vs. φ₁ Scatter Plots by Surface for Welch Method Spectrum.

-γ₁ vs. φ₁ Scatter Plots by Surface of 1-D Components for 2-D Spectrum.

2-D Equivalent Spectral Parameters w_2 and γ_2

2-D Equivalent Spectral Parameters γ_2 vs w_2 Scatter Plots with 'Sand' Data: Welch Method Spectrum
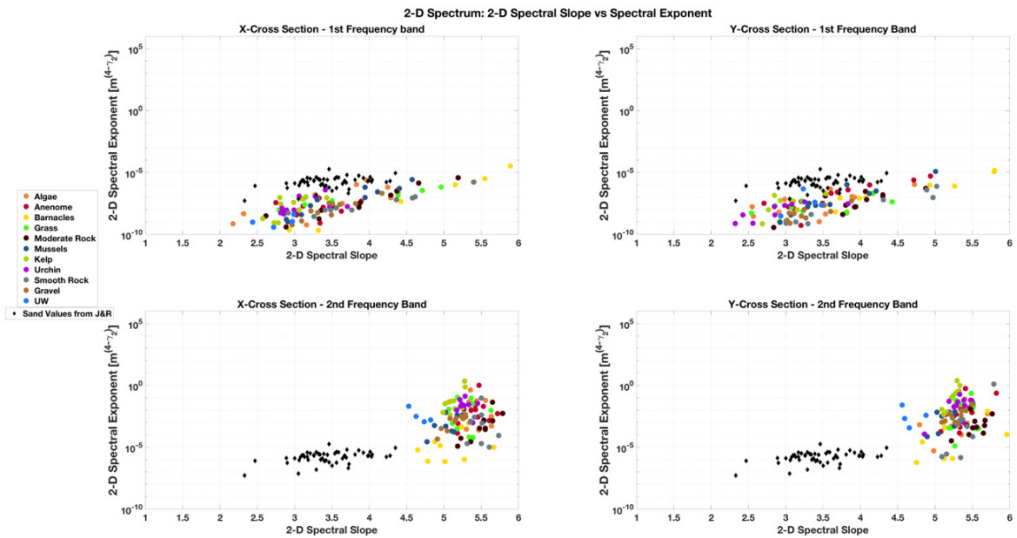
2-D Equivalent Spectral Parameters γ_2 vs w_2 Scatter Plots with 'Sand' Data: 2-D Spectrum

87

Fractal Dimension Parameter
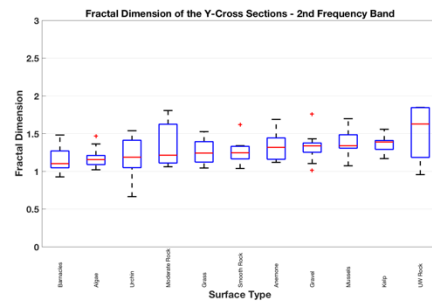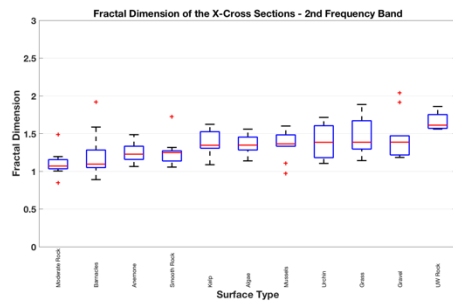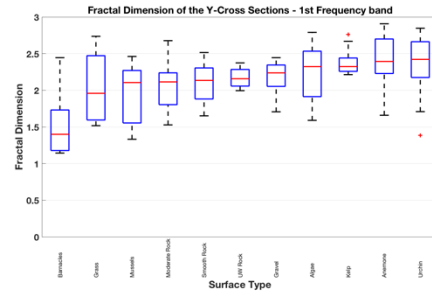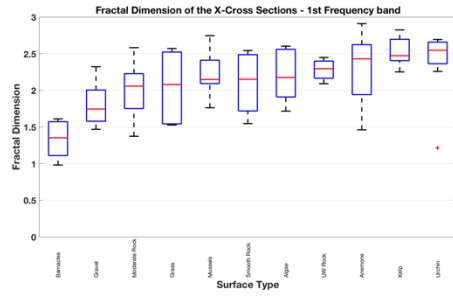
Fractal Dimension Values for Welch Method Spectrum.

Scattering Strength Estimates – Perturbation Method

Scattering Strength for 1st Frequency Band of Welch Method Spectrum:
Grazing and Scattering Angles of 10°, 45°, and 60°

Scattering Strength for 2nd Frequency Band of Welch Method Spectrum:
Grazing and Scattering Angles of 10°, 45°, and 60°

2D Spectrum Scattering Strength: 1st Frequency Band, 10, 45, 60 Degree Grazing and Scattering Angle
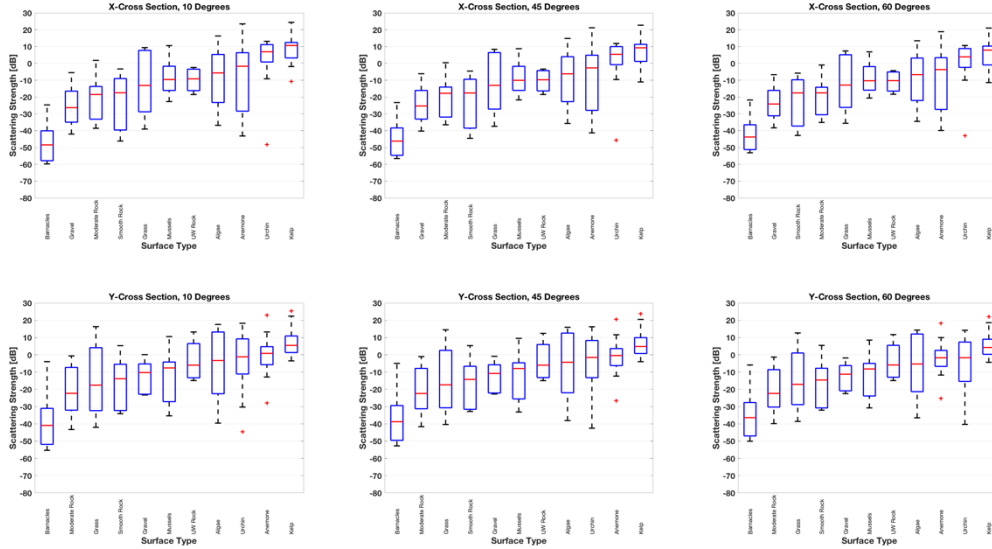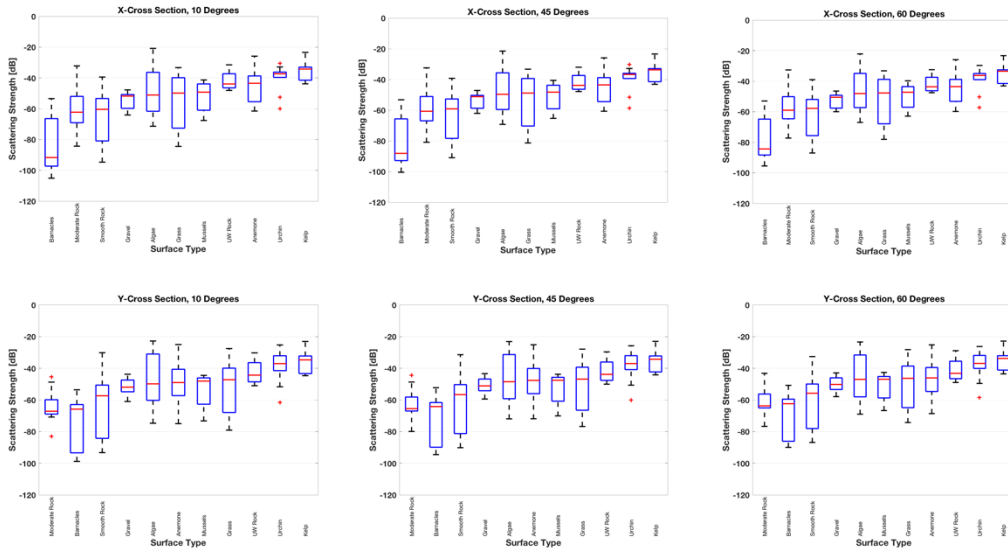
Scattering Strength for 1st Frequency Band of 2-D Spectrum:
Grazing and Scattering Angles of 10°, 45°, and 60°

2D Spectrum Scattering Strength: 2nd Frequency Band, 10, 45, 60 Degree Grazing and Scattering Angle
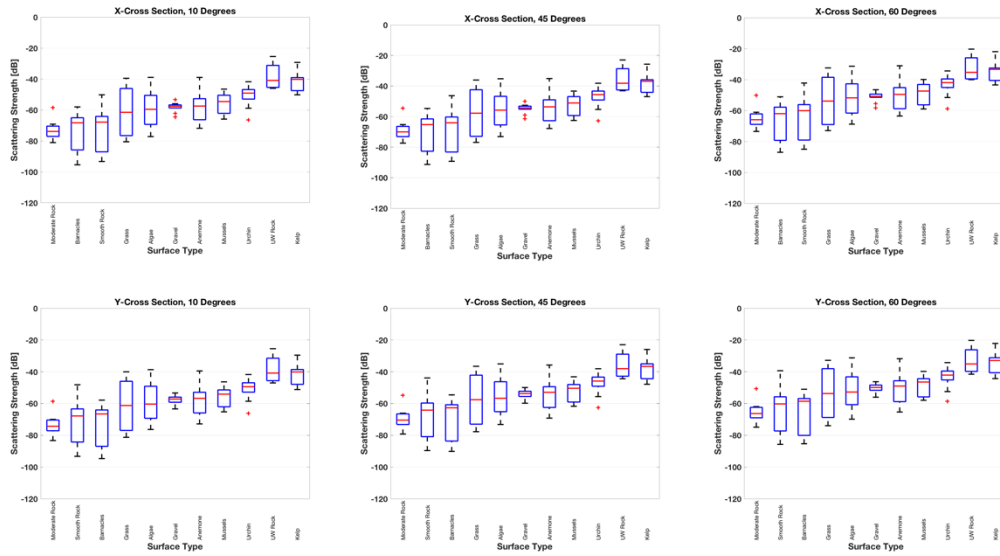
Scattering Strength for 2nd Frequency Band of 2-D Spectrum:
Grazing and Scattering Angles of 10°, 45°, and 60°

LIST OF REFERENCES

Agisoft LLC, 2020: Agisoft Metashape User Manual: Professional Edition, Version 1.6, 154, https://www.agisoft.com/downloads/user-manuals/.

AOI dual fiber optic cable with sea & sea ends, n.d.: Backskatter. Accessed May 5, 2020, https://www.backscatter.com/AOI-Dual-Fiber-Optic-Cable.

Ballard et al., 2020: Application of acoustical remote sensing techniques for ecosystem monitoring of a seagrass meadow, *Acoustical Society of America*, **147**, https://doi.org/10.1121/10.0000954.

Briggs, K. B., 1989: Microtopographical roughness of shallow-water continental shelves, *IEEE J. Oceanic Eng.,* **14**, 360–367, https://doi.org/10.1109/48.35986.

Briggs, K.B, Tang, D., and Williams K.L., 2002: Characterization of interface roughness of rippled sand off Fort Walton Beach, Florida, *IEEE J. Oceanic Eng.,* **27**, 505–514.

Gaines, S., Airame, S., NOAA: Upwelling, accessed 3 May 2020, https://oceanexplorer.noaa.gov/explorations/02quest/background/upwelling/upwelling.html.

Google, Google Earth Pro, accessed 15 April 2020, https://www.google.com/earth/versions/#earth-pro.

Gragg, R. F., D. Wurmser, and R. C. Gauss, 2001: Small-slope scattering from rough elastic ocean floors: General theory and computational algorithm, *The Journal of the Acoustical Society of America*, **110**, 2878–2901, https://doi.org/10.1121/1.1412444.

Greene, H.G., 1977: Geology of the Monterey Bay Region. Open-file Report 77–718, 363 pages, https://pubs.er.usgs.gov/publication/ofr77718.

Gruber, J. A., 2019: Measurements of acoustic scattering from rocky outcrops in Monterey Bay, Oceanography Department, Naval Postgraduate School, 72, https://calhoun.nps.edu/handle/10945/64176.

Eittreim, S.L., Anima, R.J., and A.J. Stevenson, 2002: Seafloor Geology of the Monterey Bay area continental shelf. *Marine Geology*, **(3-4)**, 3–34, https://doi.org/10.1016/0025- 3227(02)00382-1.

Jackson D.R. et al., 2009: Acoustic observation of the time dependence of the roughness of sandy seafloors, *IEEE Journal of Oceanic Engineering*, **34 no. 4**, pp. 407–422.

Jackson, D. R., Richardson M.D., 2007: *High-Frequency Seafloor Acoustics*. Springer, 616.

Jones, C. D. and Jackson D.R., 2001: Analysis of the small perturbation method for high-frequency scattering from marine sediments, *Proceedings of the Fifth European Conference on Underwater Acoustics*, pp. 1259–1264. https://ieeexplore.ieee.org/stamp/stamp.jsp?tp=&arnumber=917934.

Karmacharya, Sanat & Bishwakarma, Meg & Shrestha, Ujjwal & Rüther, Nils., 2019: Application of 'Structure from Motion' (SfM) technique in physical hydraulic modelling, *Journal of Physics: Conference Series*, **1266**, https://www.researchgate.net/publication/334907890_Application_of_'Structure_from_Motion'_SfM_technique_in_physical_hydraulic_modelling.

Leon, J. X., C. M. Roelfsema, M. I. Saunders, and S. R. Phinn, 2015: Measuring coral reef terrain roughness using 'Structure-from-Motion' close-range photogrammetry, *Geomorphology*, **242**, 21–28, https://doi.org/10.1016/j.geomorph.2015.01.030.

Lyons, A.P, Brown, D.C, 2013: The Impact of the Temporal Variability of Seafloor Roughness on Synthetic Aperture Sonar Repeat–Pass Interferometry, *IEEE Journal of Oceanic Engineering*, **38 no. 1**, pp. 91–97.

Lyons, A. P., W. L. J. Fox, T. Hasiotis, and E. Pouliquen, 2002: Characterization of the two-dimensional roughness of wave-rippled sea floors using digital photogrammetry, *IEEE J. Oceanic Eng.*, **27**, 515–524, https://doi.org/10.1109/JOE.2002.1040935.

Mathworks Inc., 1994–2020: Accessed 20 April 2020, https://www.mathworks.com.

McKinney, C. M., and C. D. Anderson, 1964: Measurements of Backscattering of Sound from the Ocean Bottom, *The Journal of the Acoustical Society of America*, **36**, 158–163, https://doi.org/10.1121/1.1918927.

Merriam-Webster (n.d.): Roughness. Retrieved 25 April 2020. https://www.merriam-webster.com/dictionary/roughness.

National Research Council (U.S.), 2007: *Distributed Remote Sensing for Naval Undersea Warfare*, Washington, D.C.: The National Academies Press, **41**, https://ebookcentral.proquest.com/lib/ebook-nps/reader.action?docID=3378256&query=.

NOAA, 2019: Monterey Bay National Marine Sanctuary. Accessed 18 May 2020. https://montereybay.noaa.gov.

NOAA Tides and Currents, 2019: Station 9413745, accessed 3 April 2020, https://tidesandcurrents.noaa.gov/noaatidepredictions.html?id=9413745&units=st andard&bdate=20200205&edate=20200206&timezone=LST/LDT&clock=12hou r&datum=MLLW&interval=hilo&action=dailychart.

Oelze, M.L., Raspet, R., Sabatier, J., 2002: Application of an Acoustic backscatter technique for characterizing the roughness of porous soil, *The Journal of the Acoustical Society of America*, **14**, https://www.researchgate.net/publication/11367857.

Olson, D.R., 2014: High-frequency acoustic scattering from rough elastic surfaces. The Pennsylvania State University, The Graduate School, 319, https://etda.libraries.psu.edu/files/final_submissions/10212.

Olson, D. R., A. P. Lyons, and T. O. Sæbø, 2016: Measurements of high-frequency acoustic scattering from glacially eroded rock outcrops. *The Journal of the Acoustical Society of America*, **139**, 1833–1847, https://doi.org/10.1121/1.4945589.

Olympus, Digital Camera TG-6 Instruction Manual, Model No: IM015, https://learnandsupport.getolympus.com/support/tough-tg-6.

Olympus, PT-059 Manual, https://www.backscatter.com/images/article/content/olympus-tg-6/Olympus_PT-059_Manual.pdf.

Richardson, M. D., K. B. Briggs, K. L. Williams, A. P. Lyons, and D. R. Jackson, N.D., n.d.: Effects of changing roughness on acoustic scattering: (2) anthropogenic changes. Technical report, Naval Research Laboratory, Stennis Space Center, MS.

Russ, J. C., 2007: *The Image Processing Handbook*. Taylor and Francis Group, 834.

Sea Grant California, King Tides: A cosmic phenomenon, accessed 1 May 2020, https://caseagrant.ucsd.edu/extension-outreach/facts-and-resources/king-tides-a-cosmic-phenomenon.

Sea & Sea, Y-S-D2 Underwater Strobe, https://www.backscatter.com/Sea-and-Sea-YS-D2-Underwater-Strobe.

Soukup, R. J., and R. F. Gragg, 2003: Backscatter from a limestone seafloor at 2–3.5 kHz: Measurements and modeling, *The Journal of the Acoustical Society of America*, **113**, 2501–2514, https://doi.org/10.1121/1.1558039.

Stack, J., 2011: Automation for underwater mine recognition: current trends and future strategy, Proceedings of SPIE, SPIE Defense, Security and Sensing, Orlando, Florida, United States, 80170K, https://www.spiedigitallibrary.org/conference-proceedings-of-spie.

Tang, D., 2004: Fine-scale measurements of sediment roughness and subbottom variability, *IEEE J. Oceanic Eng.*, **29**, 929–939, https://doi.org/10.1109/JOE.2004.834176.

Thomson, D.J., 1982: Spectrum estimation and harmonic analysis, *Proceedings of the IEEE 70*, **9**, 1055–96. https://doi.org/10.1109/PROC.1982.12433.

Urick, R. J., 1954: The backscattering of sound from a harbor bottom. *The Journal of the Acoustical Society of America*, **6**, https://doi.org/10.1121/1.1907314.

Vanderbilt, Fractals and Fractal Dimensions, accessed 16 May 2020, https://www.vanderbilt.edu/AnS/psychology/cogsci/chaos/workshop/Fractals.html

Welch, P., 1967: The use of fast fourier transform for the estimation of power spectra: A method based on time averaging over short, modified periodograms, *IEEE Transactions on Audio and Electroacoustics*, **15 no. 2**, 70–73, https://doi.org/10.1109/TAU.1967.1161901.

INITIAL DISTRIBUTION LIST

1.   Defense Technical Information Center
        Ft. Belvoir, Virginia

2.   Dudley Knox Library
        Naval Postgraduate School
        Monterey, California